12-9-2022

Molecular dynamics of high temperature hydrogen attack

Mike Travis Bodden Connor
mkbodden@yahoo.com

Follow this and additional works at: https://scholarsjunction.msstate.edu/td

Part of the Computer-Aided Engineering and Design Commons, and the Other Mechanical Engineering Commons

Molecular dynamics of high temperature hydrogen attack

By

Mike Travis Bodden Connor

Approved by:

Christopher D. Barrett (Major Professor)
Doyl E. Dickel
Matthew W. Priddy
Tonya W. Stone (Committee Member/Graduate Coordinator)
Jason M. Keith (Dean, Bagley College of Engineering)

A Dissertation
Submitted to the Faculty of
Mississippi State University
in Partial Fulfillment of the Requirements
for the Degree of Doctor of Philosophy
in Engineering, Mechanical Engineering
in the Department of Mechanical Engineering

Mississippi State, Mississippi

December 2022

Name: Mike Travis Bodden Connor

Date of Degree: December 9, 2022

Institution: Mississippi State University

Major Field: Engineering, Mechanical Engineering

Major Professor: Christopher D. Barrett

Title of Study: Molecular dynamics of high temperature hydrogen attack

Pages in Study: 104

Candidate for Degree of Doctor of Philosophy

High temperature hydrogen attack (HTHA) is a damage mechanism that only affects carbon steel and low alloy material. Most of the data regarding HTHA are experimental-driven. Even though this approach has been successful, there are still much more things that the oil and gas industry does not understand about HTHA. The regions that were considered safe (below the Nelson curves) have experienced catastrophic failure. Our research consists of performing Molecular Dynamics (MD) and the Nudge Elastic Band (NEB) calculation of HTHA to better understand the atomistic behavior of this damage mechanism.

Key words: Interatomic potential, HTHA, NEB, Cementite

DEDICATION

To my parents (Lorna Bodden Connor, and Clifford Feurtado Mann) who are no longer with us, my wife Karen Wilson, and three daughters Lorna, Nia, and Janae. Also, to my brothers Alson, Alvin (no longer with us), and Livingston Brooks who have been a big support throughout my life.

ACKNOWLEDGEMENTS

This dissertation would not have been possible without the numerous instructors, mentors, professors, friends, church members (Alvarez Johnson), and loved ones who have helped me get to this place in my life, for which I am grateful. Starting from my high school math teacher (Clark Johnson), undergraduate professors from the Universidad National Autonoma de Honduras to my graduate professors at Mississippi State University. A special thanks to my Ph.D. adviser Dr. Christopher Barrett who had graciously agreed to serve as my advisor. He knew that this was a distance program, and the topic was unique and unknown to him but decided to take this journey with me.

TABLE OF CONTENTS

LIST OF TABLES

LIST OF FIGURES

CHAPTER I

INTRODUCTION

1.1   General objective

Hydrogen embrittlement (HE) and high-temperature hydrogen attack (HTHA) are both damage mechanism that involves hydrogen diffusion into the steel. The main differences include the temperature range in which the mechanism is dominant (HE from ambient to ~149°C, HTHA from 204°C to ~700°C) and material susceptibility [1–6]. HTHA is a degradation mechanism that occurs when carbon steel and low alloy steel are exposed to prolonged high temperatures and a hydrogen-rich environment [3,7]. At temperatures of 204°C and above with hydrogen partial pressures starting around 50 psia, molecular hydrogen separates into individual atoms which readily diffuse into steel [8–14]. Hydrogen atoms react with carbon in locations such as grain boundaries and precipitate boundaries, reducing iron carbides (Fe_3C) and forming cavities that are filled with CH_4 gas. CH_4 molecule is too large to diffuse out of the steel which eventually causes high internal stresses that allows the cavities to grow and coalesce due to the internal stresses, microcracks are formed, which eventually leads to intergranular failures of components [3,15–20]. High-temperature hydrogen attack (HTHA) has been an issue for many years. Most of the data regarding HTHA are experimental-driven. Even though this approach has been successful, there are still much more things that the oil and gas industry does not understand about HTHA. The regions that were considered safe (below the Nelson curves) have experienced a catastrophic failure. The greatest incident to date due to HTHA occurred on April 2, 2010, in the Tesoro

Anacortes Refinery in Washington where a carbon steel heat exchanger (E-6600E) experienced a catastrophic rupture after 40 years of service[21–24]. This exchanger was in the Catalytic Reformer / Naphtha Hydrotreater unit (NHT). Hydrogen and Naphtha at 262.2°C (504°F) and 291 psia were released from the exchanger and ignited, causing an explosion that burned for more than 3 hours. This incident fatally injured 7 Tesoro employees [22,24,25]. During the investigation of the incident, it was determined that the heat exchanger operated in the safe zone region of the Nelson Curves for HTHA [22]. After this event, a Joint industry project (JIP) was developed that was supported by 9 refineries and petrochemical companies to better understand the behavior of HTHA and develop a more robust inspection process regarding this damage mechanism.

1.2   Introduction of MD for HTHA and a review article on HTHA

Chapter 2 consists of the introduction of molecular dynamics (MD) for HTHA and a review article on HTHA. The introduction of the MD portion is some of our preliminary findings in our research using a small atomistic structure and run time. It shows the behavior of CH_4 as it approaches other CH_4 molecules and Fe. We noticed that at a certain distance CH_4 repels each other and at closer distances, they separated into H and C atoms. The repulsion is due to the CH_4 being a stable composition and the attraction occurs because the C-C bond is stronger at very close distances compare to the C-H bond. It also shows that CH_4 is stable in a void size as small as 7.8 Å in diameter. The attraction force between H and the Fe_3C structure increased significantly as the H is at ~ 5Å above the surface. The review article portion covers the hydrogen-assisted damage mechanism, the three stages of HTHA, primarily factors that affect HTHA, incubation time-period, oil and gas industry code that governs HTHA, inspection methods that are mostly used to detect HTHA, etc.

1.3 Failure analysis of an M7X1 high-speed steel tap

Chapter 3 does not cover the HTHA damage mechanism, but it explores a case study that describes the failure of an M7x1 high-speed steel tap that experienced a torsional brittle fracture while a crescent wrench was applied by hand to create threads in a steel brake caliber of a motorcycle. The tap is fractured into two pieces forming a 45° angle concerning the long axis of the tap. The crack origin was in one of the flutes of the tap. An FEA was performed and the failure location in the model was consistent with the location in which the tap failed. The hardness of the tap was well below the recommended per ASTM A600 and large cementite particles were on the microstructure. These large particles lead to a reduction in hardness, hence reducing the strength of the material. Also, per [26], stress tends to be lower in smaller cementite particles and higher in larger cementite particles. The original tap was compared to a new tap that had properties in accordance with ASTM A600. The original tap failed at approximately 27.3% lower torque than it should have been. The hardness testing between the original and new taps was~18% in HRC values which led to a converted tensile strength difference of ~27%. Both taps were identified to be M2 high-speed Molybdenum based.

1.4 Molecular dynamics of HTHA

Chapter 4 is the bulk of our research. In this chapter, we show the importance of an atomistic approach to understanding HTHA. Performing Molecular Dynamics (MD) of HTHA allowed us to see the different behavior of CH_4 in Fe_3C structure in MD timescale, determine a depth/time ratio of H on a Fe_3C structure, determine the effect of temperate on the structure, etc. We also performed the Nudge Elastic Band (NEB) calculation method to determine the minimum energy path of the CH_4. This approach allowed us to determine the required energy to extract C from Fe_3C and form CH_4. We were also able to determine why HTHA occurs quicker in some case

scenarios compared to others even though they operate at the same parameter conditions. Our research was separated into 4 objectives: 1) Explore how can hydrogen get into the void of a cementite structure from a surface, 2) Explain how Hydrogen can take Carbon out of a cementite structure, 3) Determine the effect of the density level of Hydrogen on CH_4 formation, 4) Evaluate the rate of formation of CH_4 at different temperature and void size. A first-of-its-kind Fe-C-H MEAM interatomic potential was used to perform the calculation. Our data showed that CH_4 forming on a surface was much more difficult (requires twice as much energy) than for the CH_4 to form inside a void. It also showed that in the presence of H atoms, CH_2 more and likely would form first, then CH_3 after that CH_4 or CH_2 then CH_4 or CH_3 then CH_4. An introduction of the Eyring equation on how to determine the rate constant using the free energy activation was presented with general guidelines on how our data can be used in conjunction with the empirical data from the Nelson curve.

CHAPTER II

INTRODUCTION OF MOLECULAR DYNAMICS FOR HIGH TEMPERATURE

HYDROGEN ATTACK

This chapter is adapted from our previously published article: Mike T. Bodden Connor, Christopher D. Barrett; Introduction of Molecular Dynamics for HTHA and a Review Article of HTHA. Journal of Failure Analysis and Prevention

2.1   Introduction Molecular Dynamics for high temperature hydrogen attack (HTHA)

In [27] (see figure related to historical overview of approaches to HE studies), we show the historical overview of the various approaches over the years for hydrogen embrittlement (HE) in which the change in the scale of study is from a macro approach, through a micro-meso approach, up to the nano and atomistic approach. The most contemporary research (nano and atomistic approach) discusses the hydrogen-materials interaction, effects of hydrogen on the mechanical properties, and the multiple HE mechanisms in metallic materials [28]. This approach is based on using advanced methods of microscopy, computational modeling/simulation, hydrogen mapping, and other experiments such as scanning electron microscopy (SEM), transmission electron microscopy (TEM), environmental transmission electron microscopy (ETEM), atomic force microscopy (AFM), focused-ion beam (FIB) microscope and machining, thermal desorption spectroscopy (TDS) analysis, atomistic/quantum/meso/macro mechanical models (density functional theory (DFT) modeling and first-principles modeling, cohesive zone modeling (CZM), molecular dynamics (MD) simulation and Monte Carlo (MC) simulation, finite element (FE)

simulation of polycrystalline materials), advanced macro- micro- and nano-mechanical testing (like slow strain rate testing (SSRT), nano indentation testing, including micro-fracture mechanics models) [28].

In non-hydride-forming metals, the two mechanisms responsible for HE are the hydrogen-enhanced localized plasticity (HELP) and the hydrogen-enhanced de-cohesion (HEDE) [29][30][31]. HELP depends on the enhancement in the mobility of dislocations while the HEDE results in a very sudden and sharp ductile-brittle transition [29]. The coexistence and synergistic activity HELP (Hydrogen-enhanced localized plasticity) and HEDE (hydrogen-enhanced de-cohesion) mechanism that causes the HE in metals were recently detected and confirmed experimentally and through computations-simulations [28]. The localized plasticity effects were noticed at the micro-and nano-level, even in the case of a macroscopically brittle fracture [28]. While recent developments have shown some promise in enhancing empirical modeling efforts for avoiding HTHA [32], physics-based predictive modeling, similar to HE, should be viewed as the ideal goal. A predictive physics-based model would be superior because it requires fitting to fewer HTHA-damaged components under various boundary conditions, as well as providing a greater understanding of the scientific driving mechanisms for HTHA.

A modified embedded-atom method (MEAM) interatomic potential has been developed for Fe-C-H at Mississippi State University based on the density functional theory to enable large-scale molecular dynamics simulations of carbon steel and hydrogen. This MEAM potential was developed by Dr. Sungkwang Mun, Dr. Nayeon Lee, Dr. Doyl Dickel, Dr. Sara Adibi, Dr. Bradly Huddleston, Dr. Raj Prabhu, and Dr. Krista Limmerd by utilizing the work done by [33,34] concerning the Fe-C and Fe-H MEAM potential. This potential is the first of its kind and it consists of having the three alloying elements in one (Fe-C-H). It was developed primarily to evaluate the

effects of hydrogen embrittlement. In the developmental process of the potential, H interactions with C inside a Fe matrix were simulated with the first-principles density functional theory. This information was then bridged to the molecular dynamics (MD) scale.

The Fe-C-H potential is also being utilized by Mike T. Bodden Connor and Christopher D. Barrett to evaluate HTHA from an atomistic point of view at Mississippi State University. They are utilizing the Large-scale Atomic/Molecular Massively Parallel Simulator (LAMMPS) software developed by Sandia National Laboratory to simulate the H interaction with C and Fe to form CH_4. Below are the preliminary findings obtained on the small size simulation and the larger simulation data will be published at a later date.

2.1.1   Preliminary findings of atomistic simulation

In a Fe unit cell, Hydrogen (H) will reside in the tetrahedral interstitial site and Carbon (C) in the octahedral interstitial site[33,34]. The formation of CH_4 produced a tetrahedral structure with 4 equal bond angles and 4 equal bond lengths. During the simulations, it was noticed the importance of a minimum distance between the elements (Fe-C-H) to form met. When the Fe, C, and H atoms are too close to each other, the Fe and C attraction force and the Fe and H attraction forces are stronger than the H and C attraction force. Therefore, C and H will always want to bond with Fe before they bond with each other. Per the preliminary data, CH_4 will form if there is a saturation of C and H in the Fe matrix around an empty void that is large enough to accommodate the reaction.

2.1.2   The minimum distance between two CH_4

In [27] (see figure related to two CH_4 at 2 Å, two C bond together, two CH_4 at 3 Å, two CH_4 at 8.15 Å) two CH4(C is the gray sphere and H is the white) were placed in a large box

(17.0887 x 17.0887x 17.0887 Å) and it was noticed that they repel each other if the distance was lesser than 3 Å. This is true because CH4 is a stable composition and doesn't want to react with any other elements. CH_4 separated at 2 Å, two C bond together, two CH_4 at 3 Å, two CH_4 at 8.15 Å showed that the attractive force between the two C is greater than the C and H which causes the separation of the H from the C, the two CH4 repel each other but H does not separate from C.

2.1.3   The minimum distance between CH4 and Fe

In [27] (see figures related to CH4 and Fe at 3 Å, C bonds to Fe, CH4 and Fe at 3.5 Å, CH_4 and Fe at 11.14 Å) one CH_4 (C is the grey sphere and H is the white) and one Fe (brown sphere) was placed in a large box (17.0887 x 17.0887x 17.0887 Å) and it was noticed that at a distance lower than 3.5 Å, the bond strength between the Fe and C is greater than the H and C. This causes the H to separate from C. At 3.5 Å and greater, the CH4 repels from Fe but does not separate.

2.1.4   CH4 in a Cementite (Fe3C) structure

In [27] (see figures related to Fe3C structure, CH4 inside 7.8 Å diameter void), due to the low weight percentage of carbon in most carbon steel materials, it tends to lead to the formation of a cementite (Fe3C) structure. For this simulation model, a Fe3C structure was obtained from materials API and input into the Burai software (GUI of quantum espresso) to obtain the coordinates then visualized in the Ovito software (open visualization tool) (Fe is the brown sphere, C is the gray, H is the white). A structure was generated with 0.0 17.9634 xlo xhi, 0.0 16.12072 ylo yhi, 0.0 26.95724 zlo zhi coordinates.

Multiple analysis was performed by creating a void in the center and placing one CH4 in the middle of the void to determine at what size the CH4 will not separate and bond to Fe or C. It was noticed that a void size of 7.8 Å in diameter was the minimum size to achieve CH4 stability.

2.1.5   CH$_4$ formation inside a Cementite structure and H diffusion in the steel

In [27] (see figures related to void size of 11.1 Å in diameter, CH$_4$ formation inside the Fe$_3$C structure, H atoms 15 Å above Fe$_3$C structure, H diffused into Fe$_3$C structure, Energy vs length of H diffusion into Fe$_3$C structure), to get CH$_4$ to form, a large void size of 11.1 Å in diameter was created inside the cementite structure (0.0 17.9634 xlo xhi, 0.0 16.12072 ylo yhi, 0.0 26.95724 zlo zhi coordinates) and saturated with 71 H and two C inside the void.

160 atoms of H were placed at 15 Å above the cementite structure. During the simulation, it was noticed that when H was at approximately 5 Å above the surface, the attraction force increased significantly, and H diffused into the steel. This is shown in the energy vs length graph figure. Below 5 Å, the attraction force increased, and above it decreases.

2.2   Hydrogen-assisted damage mechanisms

The hydrogen-assisted mechanical degradation of steel is a very complex phenomenon. This is due to the number of unknowns in the degradation process kinetics which can produce various effects [29]. As atomic hydrogen penetrates the steel, it reduces the ductility of the material and produces intergranular cracks which can lead to brittle cracking. The term hydrogen damage is commonly used to represent many hydrogens-assisted types of damage which can range from environmental damages, material microstructural changes, and hydrogen-material interactions caused by the presence of hydrogen in metals [29,35]. The mechanisms normally take place from ambient temperature to high temperature (above 700°C). The types of hydrogen damage can be classified into blisters, hydrogen-induced cracking (HIC), hydrogen stress cracking (HSC), hydrogen embrittlement (HE), and high-temperature hydrogen attack (HTHA) [35]. Of these, HE and HTHA are the most common. In this work, we focus primarily on HTHA and point out similarities and contrast between it and HE.

2.2.1 Hydrogen blisters

Hydrogen blisters can form in multiple areas in the metal such as on the internal diameter, external diameter, or mid-wall of a metal plate of pressure vessels or pipe [2] (figure 1). Blisters are bulges on a metal surface that are filled with hydrogen gas [2]. This hydrogen is a result of the corrosion process between the process stream and the metal surface in which the hydrogen atoms enter the steel and form hydrogen molecules that are too large to diffuse out of the metal [2].

2.2.2 Hydrogen-induced cracking (HIC)

As neighboring hydrogen blisters at different depths (surface, middle of the plate, near a weld) produce cracks they tend to interconnect producing a stepwise cracking appearance [2]. The linking process in part is due to the trans-granular plastic shear mechanism that occurs from the accumulation of hydrogen internal pressure [2]. HIC is also known as cold cracking or delayed cracking which is due to the combination process of tensile residual stress and absorbed hydrogen during welding [36]. Throughout the welding process, the sources of hydrogen can be obtained from moisture, organic materials in the electrode coating, flux, flux-cored wires, water vapor in air and shielding gas, hydrogen in the filler, and corrosion products [36]. A high-strength weld will have a lower resistance to HIC and the tougher a microstructure, the greater its resistance to HIC [36].

2.2.3 Hydrogen stress cracking (HSC)

Two common hydrogen stress cracking are stress-oriented hydrogen-induced cracking (SOHIC) and sulfide stress corrosion cracking (SCC) [2]. SOHIC is similar to HIC, but its appearance is a series of stacked cracks on top of each other, which can potentially result in a through-thickness crack that is perpendicular to the surface [2]. SOHIC is normally found adjacent

to the weld heat-affected zones [2]. In the oil and gas industry, SCC is produced under the combination of tensile stress and H_2S in the presence of water [2]. The reaction of sulfur (S) with iron (F) produces iron sulfide which allows hydrogen atoms to enter the steel which can eventually result in the cracking of the metal. SCC is most commonly found in areas of high hardness in the weld metal and heat-affected zone [2].

2.2.4   Hydrogen embrittlement (HE)

Hydrogen embrittlement (HE), is a mechanism of hydrogen damage in which the mechanical properties of the material are degraded, reducing the ductility and tensile strength, and decreasing the fracture resistance of steel [29,35]. This occurs as hydrogen atom enters the metal and gets trapped in diverse sites which impede it from exiting the steel. HE can occur during various processes, such as manufacturing, welding, cleaning, pickling in acid solutions, cathodic protection, and from the operating process in an aqueous or gaseous environment [2]. The prediction of HE in iron depends on numerous parameters, such as the loading rate, hydrogen chemical potential, temperature, initial crack size, effective hydrogen diffusion activation enthalpy, and cleavage stress intensity [29]. Depending on where the metal obtains its hydrogen, HE can be classified as Internal Hydrogen Embrittlement (preexisting hydrogen in the steel) and Hydrogen Environmental Embrittlement [35]. The HE effect is most pronounced from ambient temperature to 149°C and in locations of high residual or tri-axial stresses, and weld heat-affected zone [2]. It affects various carbon steel, low alloy steels, 400 series stainless steel, precipitation hardenable (PH) stainless steel, and some high strength nickel-based alloys [2].

2.2.5 High-temperature hydrogen attack (HTHA)

In contrast, high-temperature hydrogen attack (HTHA) is a degradation mechanism that occurs when carbon steel and low alloy steel are exposed to prolonged high temperatures and a hydrogen-rich environment [3,7]. HTHA is normally found in petroleum refineries and petrochemical plants and is a continuing concern in the oil and gas industry [37]. The industry currently utilizes the American Petroleum Institute (API) Recommended Practice (RP) 941 to establish safe operating limits for steels under HTHA conditions [37,38]. The API RP 941 consists of the Nelson Curves which is a temperature/hydrogen gas partial pressure graph showing certain materials' susceptibility to high-temperature hydrogen attack [38]. These curves were created mainly from empirical data on plant failures and do not account for the underlying failure mechanisms and the material microstructure [37]. HTHA induces a transition in failure from ductile micro-void coalescence to intergranular fracture [39–41]. At temperatures of 204°C and above with hydrogen partial pressures starting around 50 psia, molecular hydrogen separates into individual atoms which readily diffuse into steel [8–14]. In [27] (see figure related to CH_4 fissures. When CH_4 molecules cannot diffuse out of the steel, they accumulate inside of the steel, creating high pressure that forms fissures in steel), hydrogen atoms react with carbon in locations such as grain boundaries and precipitate boundaries, reducing iron carbides (Fe_3C) and forming cavities that are filled with CH_4 gas. The formation of CH_4 gas causes high internal stresses [3,42]. As cavities grow and coalesce due to the internal stresses, microcracks are formed, which eventually leads to intergranular failures of components [3,15–20]. These cavities grow along the grain or precipitate boundaries, leading to premature metal failure [43–50]. Cavity growth and CH_4 generation are strongly coupled [32,51,52]. The CH_4, which is a large molecule, does not diffuse out of the metal [53–57]. During the growth of pressurized methane-filled cavities, either surface

or internal decarburization occurs, leading eventually to sudden brittle failure [3,58–62]. Rates of

HTHA are difficult to predict and material failure can occur quickly or after many years of service

depending on several parameters [63]. Steel is said to have undergone a high-temperature

hydrogen attack after its mechanical properties suffer a detectable deterioration from CH_4 bubbles

formations [64], although it is generally thought that this occurs after a long nucleation phase

which is harder to detect. The chemical reaction of HTHA is given by[65,66]:

$$4H + C \rightarrow CH_4 \text{ or } 4H + MC \rightarrow CH_4 + 3M \text{ (M: metals)} \tag{2.1}$$
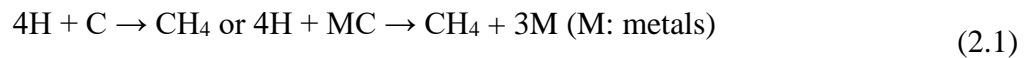
The deformation mechanism by which HTHA occurs is dependent on many material

properties such as the diffusion rate of carbon and of the metal atoms, the formation strength of

carbides, the reaction between C and H forming CH4, grain boundary strength, and diffusion, and

dislocation creep [3,32,67,68].

There are many similarities between HE and HTHA, including the penetration of hydrogen

atoms through steel, susceptible material (carbon steel and low alloy), the reduction of ductility of

the material by hydrogen, intergranular cracking, and premature failure of the metals. The main

differences include the temperature range in which the mechanism is dominant (HE from ambient

to ~149°C, HTHA from 204°C to ~700°C) and material susceptibility (HE can affect carbon steels,

certain stainless steel, and high strength nickel base alloys, HTHA can affect carbon steels and low

alloy steels) [1–6].

2.3   Factors affecting HTHA

2.3.1   Temperature and pressure

The severity of the hydrogen attack intensifies with increasing temperature and hydrogen

partial pressure. This leads to more pronounced fissuring, permanently reducing the ductility of

the metal [60,69,70]. HTHA activates either by surface decarburization and/or internal decarburization [58]. Surface decarburization is less problematic than internal decarburization [58]. It normally occurs at high temperatures and low hydrogen partial pressures. In the surface decarburization mechanism, diffusion of carbon to the surface transpires where gaseous compounds of carbon are formed, primarily CH_4 [71]. This generates a depletion of carbon in the steel which tends to produce a slight localized reduction in strength and hardness and an increase in ductility in the carbon steel material. Internal decarburization, however, occurs only at higher hydrogen partial pressures and elevated temperatures. In [27] (see figure related to internal decarburization and fissuring in HTHA), after an incubation period in which hydrogen penetrates through the steel, CH_4 formation begins in voids, taking carbon from the surrounding material. Damages during this period are very difficult to detect [72]. The total CH_4 pressure ($P_m = P_{CH4}$ $+P_{H2}$) is a combination of the partial equilibrium CH_4 pressure (P_{CH4}) and the partial hydrogen pressure (P_{H2}) [73]. High pressures caused by the CH_4 gas formation induce void growth and coalescence, permanently damaging the steel and sometimes leading to catastrophic brittle failure [58].

Grain boundaries are the ideal location for void growth, not only because the greatest amount of unstable carbides is located there, but also because cavities located there can grow rapidly by grain boundary diffusion [73]. Void growth related to HTHA has led to many researchers trying to develop a model that can accurately predict its behavior. In [37], some of those models are reviewed:

- Shewmon (1976): a model based on grain boundary diffusion of iron [4].
- Sagues et al. (1978): analytical model considering both grain boundary diffusion and power-law creep [74].

14

- Needleman and Rice (1980): a model of interaction of bulk creep deformation with grain boundaries diffusion for creep cavitation applications [75].

- Sundararajan and Shewmon (1981): a model based on a fraction of the grain boundaries being cavitated and the un-cavitated grains were assumed to enact a constraint on the void growth of the cavitated grain boundaries. The void growth is assumed to be accommodated by the surrounding matrix [62].

- Shih and Johnson (1982): a more detailed study on Sagues et al. (1978) [76].

- Shewmon (1987): a model to account for the interaction between internal CH_4 pressure and external stress [77].

- Van der Giessen et al. (1995): a model with multiaxial stress to study void growth under higher triaxialities stresses [20].

Overall, the models managed to capture some of the qualitative aspects of HTHA. However, the models are not predictive, which is in part due to the complexity of the interaction between the various processes or the use of simple estimated methods [37]. One of the more recent studies was done in 2019 in [37] by combining the model of Stone (1984) and Van der Giessen et al. (1995) to analyze HTHA kinetic by the constrained cavity growth model on 2-1/4Cr-1Mo steel. Voids' growth in the cavitated boundary will generate an increase in stress σ_A in the un-cavitated grain region while decreasing the stress in the cavitated region σ_B. The constraint comes from some grain boundaries that are cavitated while others are not, and this exerts opposing stresses to void growth on cavitated grains. The model simulated void growth agreed with the experimentally measured void growth.

2.3.2 Hydrogen sources and solubility

Since hydrogen is ubiquitous and diminutive, the permeation process into steel is inexorable. Hydrogen (H) can penetrate the steel throughout the steel lifecycle, including during the fabrication, heat treatment, corrosion, welding, galvanizing, cathodic charging, and pickling processes, and throughout the operation period [78–87]. Hydrogen can also get trapped in the electrodeposition layers of zinc, cadmium, and nickel coatings and eventually make its way into the base material [88]. Some processes in the industry (welding rods, heat treatment, etc.) require low hydrogen or free hydrogen environment to minimize the impact of the material properties. Hydrocarbons have many chemical elements with hydrogen, carbon, and sulfur being some of the most common. Water is found in hydrocarbon streams as it is extracted from the ground. Also, to assist in the desalting process of hydrocarbon, water is added to reduce salt formation. When Hydrogen Sulfide (H_2S) is in the presence of free water (H_2O) at a certain temperature, the sulfur (electronegative) reacts with the iron (electropositive) in the steel which forms iron sulfide (FeS). This chemical reaction process frees hydrogen atoms that permeate the steel. The more H is dissolved, the more it tends to reduce the mechanical properties of metal and make it more susceptible to cracking [5,89–94]. Hydrogen solubility in steel depends primarily on the amount of tensile stress, percentage of hydrogen, and heating temperature the metal is exposed to. Hydrogen gas concentration in metals can be expressed by Sievert's law [95]:

$$C_H = k(pH_2)^{1/2} \tag{2.2}$$

C_H = concentration of hydrogen
k = constant dependent upon temperature and crystal structure
pH_2 = partial pressure of molecular hydrogen

An example of the effect of temperature and pressure on hydrogen solubility is shown in an investigation from A.A. Astaf [78] (see table related to the content of hydrogen H is given after holding for 1 h at different temperatures (t_{test}) and stresses (σ)). The investigation consisted of saturating a specimen of steel in hydrogen at 1150°C, then reducing and holding the temperature at 100°C, 300°C, 400°C, and 600°C for 1 hour without stress and under various tensile stresses. The residual stress was determined in vacuum heating. Astaf showed that a certain combination of temperature and tensile stress tends to generate an increase of hydrogen diffusion into the steel, while other combinations facilitated the removal of hydrogen from the steel.

2.3.3   Incubation Time

Understanding the incubation stage of HTHA is critical for understanding and controlling the ensuing stages of HTHA. The incubation stage is defined as the period when the metal has been exposed to a temperature and hydrogen partial pressure but no damage to mechanical properties is noticeable [96]. It is well known that the incubation stage is characterized by the growth of isolated CH_4 bubbles driven by the pressure of CH_4 within the bubbles (figure 6). Many fine CH_4 bubbles tend to nucleate and grow on the grain boundaries. Controlling the pressure of CH_4 has been suggested as a direct means of controlling hydrogen attacks [72]. The number of CH_4 bubbles and their nucleation rate is highly dependent on the CH_4 pressure [63]. The end of the incubation stage occurs when the bubbles begin to coalesce and form cracks. How long the steel remains in the incubation stage is very difficult to predict. Since HTHA is time-dependent, the longer the exposure time the greater the damage. The damages eventually produce fissures and a significant amount of decarburization in the material microstructure [27] (see the figure related to Micro-fissures forming continuous cracks).

17

Howard G. Nelson and R. Dale Moorhead [97] showed that an SAE 1025 carbon steel material (0.25% C) subjected to 3.5MPa and 575°C had some decreased mechanical properties after 136 h of exposure time, and after 408 h, the strength of the material was reduced by 40 percent. Comparing this example with the accepted Nelson Curve practice in API RP 941, as can be seen in the window section in [27] (see the figure related to window section of Nelson Curves) at point A, the experiment conditions are above the desired curve in the unsafe zone. The material will be subject to premature failure due to HTHA. To operate a piece of equipment under these conditions one should utilize a higher nickel alloy type material.

2.3.4   Alloy composition

Due to the extreme weakening which can be produced by HTHA, ideal materials must be selected for industrial applications requiring significant exposure to high partial pressures of hydrogen under elevated temperatures [98–101]. In the petrochemical industry, HTHA is commonly found in carbon and low alloy steel piping and pressure vessels [53]. However, some steel alloys have shown substantially high resistance to HTHA effects. Some alloys in order of increasing HTHA resistance are [2]: Carbon steel, C-0.5Mo, Mn-0.5Mo, 1Cr-0.5Mo, 1.25Cr-0.5Mo, 2.25Cr-1Mo, 2.25Cr-1Mo-V, 3Cr-1Mo, 5Cr-0.5Mo.

Two strategies have been used with success for material selection with higher HTHA resistance. First, the use of stainless steel materials in which hydrogen solubility and diffusivity are much lower compared to carbon steel effectively suppresses HTHA [102]. This is due to stainless steel having a face-centered cubic crystal structure unlike the body-centered cubic structure of low-carbon steel. Additionally, several alloying elements have a role in stabilizing carbides, thus reducing CH_4 formation. These strategies are sufficiently effective that the 300 series stainless steel materials and other higher nickel alloy materials are considered non-

susceptible to HTHA [2]. This is mostly due to the addition of chromium and molybdenum which increase the stability of carbides in the grain boundaries [2,103,104]. It is common practice to utilize 300 series stainless steel as weld overlay or claddings with carbon steel as the base metal to reduce HTHA susceptibility. This is due to the higher cost of stainless-steel material compared to the carbon steel material.

There have been several failures of C-0.5Mo steels in the industry under conditions that were previously considered safe operation zones. As a result, the C-0.5 Mo-alloy steels are not recommended for new construction in hot hydrogen services [2,105].

Other alloying elements such as tungsten, vanadium, titanium, and niobium, can also form more stable alloy carbides that resist breakdown by hydrogen and thereby decrease the formation of CH_4 bubbles [58]. Replacing carbon steel material with a higher alloy material is, therefore, the best solution to prevent HTHA[106], yet many carbon steel components remain in service because of the expense of replacing them all at once.

2.3.5   Post weld heat treatment

Residual stress in the weldment location occurs when two materials are welded together. The residual stress can be reduced by performing heat treatment by reheating the weld location to a temperature below its lower critical transformation temperature and held for some time. This process is known as post-weld heat treatment (PWHT). The weld locations are ideal for hydrogen trapping to generate CH_4 gas as it reacts with carbon [69]. Reducing high stresses in the material reduces its susceptibility to HTHA [58]. PWHT tends to stabilize carbides in the material. The four major microstructural regions in a weldment are the weld metal (WM); the coarse-grained heat-affected zone (CGHAZ); the fine-grained heat-affected zone (FGHAZ); and the base metal [3](BM) [27] (see the figure related to the four microstructural regions (WM, CGHAZ, FGHAZ

and BM) of the weldment). These differ in grain size and carbide type, and composition, and possess different creep properties [3]. The generation of CH_4 gas is proportional to the stability of the carbide (M_7C_3) in the weldment location. FGHAZ has the lowest carbide stability, therefore, making it the most susceptible to HTHA [58] while the WM has the highest carbide stability making it the least susceptible to HTHA [3]. It should be noted that the PWHT microstructure depends on the temperature and the duration of heat treatment. Metals that are subjected to a higher temperature during PWHT have proven to reduce susceptibility to HTHA compared to those exposed to heat treatment for a longer duration [58]. This occurs because at a higher temperature the ductility of the material increases, and the strength decreases which can facilitates dislocation movements that can lead to a reduction of any residual stresses.

2.3.6   Cold Working

Since one of the driving forces of hydrogen attack is the applied stress, cold working steel enhances the rate of fissure formation on the grain boundaries and accelerates the rate of decarburization in the steel [107][42]. It can also enhance the precipitation of carbide which can lead to a reduction of the material strength[108]. Several experiments were performed with materials, such as 1020 carbon steel (0.2 % C) utilizing a three-point bending method apparatus to compare the similitudes in microscopic damages [61]. In one of the experiments, the material was placed inside a vessel where hydrogen was introduced for durations of 44, 88, 132, 176, or 220 h. At 132 h of exposure time, mechanical properties such as the ultimate tensile strength and density of the metal changed considerably. It was noted that in the material, fissures formed primarily on the inclusions of Manganese Sulfide (MnS). With increasing amounts of cold work, the fissures began to form more along grain boundaries and were generally aligned parallel to the rolling

20

direction. The type of fissures appeared to be more of a blocky type with sharp rectangular edges [61].

2.3.7 Example of equipment failures due to HTHA

The greatest incident to date due to HTHA occurred on April 2, 2010, in the Tesoro Anacortes Refinery in Washington where a carbon steel heat exchanger (E-6600E) experienced a catastrophic rupture after 40 years of service[21–24]. In [27], see figures related to process flow of the NHT unit and post-incident view of D/E/F Heat Exchanger Bank. This exchanger was in the Catalytic Reformer / Naphtha Hydrotreater unit (NHT). Hydrogen and Naphtha at 262.2°C (504°F) and 291 psia were released from the exchanger and ignited, causing an explosion that burned for more than 3 hours. This incident fatally injured 7 Tesoro employees [22,24,25]. During the investigation of the incident, it was determined that the heat exchanger operated in the safe zone region of the Nelson Curves for HTHA [22]. See point B on the window section in [27] (see figure related to window section of Nelson Curves). This event marked a significant change in the oil and gas industry perspective of the HTHA problem which led to many companies re-evaluating their equipment to determine HTHA susceptibilities and prompted much research by diverse engineering firms to identify better tools to detect HTHA at earlier stages and provide an accurate and safer operating zone [105,109].

In [110], the heat exchanger 103-C in an ammonia plant experienced HTHA damage on several tubes [27] (see figure related to tube samples selected from the heat exchanger (left to right: Tube Nos. 1, 2, 3, 4, 5, 6, and 7). The vessel had been in service for close to 30 years. The processed gas inside the straight tube of the heat exchanger had a 42% mole fraction of hydrogen gas equating to 1.28 Mpa (185 psig) of hydrogen partial pressure. The tube side process conditions were at 3.07 MPa (445 psia) and 442°C (827°F). The tubes are 1 inch in diameter and 0.25-inch-thick

constructed of 0.5Mo carbon steel. Several HTHA cases have been noted around this temperature-pressure point for 0.5 Mo carbon steel (this material is no longer recommended for new construction in hot hydrogen services) even though it was operating in the safe zone of the Nelson curves.

2.4   Strategies used to mitigate catastrophic failure due to HTHA

2.4.1   The Nelson Curves

The most widespread technique used to assess the susceptibility of a material to HTHA is the Nelson Curves [10,22,58,111,112]. In [27], see figure related to Nelson Curves. The API RP 941 8TH Edition can be obtained from API. These curves have been progressively developed based on past equipment failures. This data was first gathered from 1940 until his death by George Nelson to establish a safe operational limit for equipment [113]. The first publication of these curves occurred in 1949 [58]. These curves consist of three fundamental variables: temperature (204°C -800°C), hydrogen partial pressure (0-13000 psia), and material of construction [58]. When a material is operating below the limiting curves, it is considered to be within the safe region. If operating above the curve, the region is considered not safe and susceptible to HTHA failure. Industry code API RP 941 recommends the end-user determine a safety factor below the curves since operating close to the curves may still enable susceptibility to HTHA [58]. Many important variables are not considered by the curves such as working stress, carbide stability, grain size, type of weld, time in operation, and operating conditions such as low cycle fatigue [22].

2.4.2 Recommended Industry Code for HTHA

In the oil and gas industry, multiple codes and standards can be used to help determine if a material is fit for continuous service after it has been exposed to HTHA. Examples and figures can be found in each respectable code. The most common codes are:

2.4.2.1 API RP 941 Steels for Hydrogen Service at Elevated Temperatures and Pressures in Petroleum Refineries and Petrochemical Plants

API RP 941 is the American Petroleum Institute (API) Recommended Practice guideline to assess HTHA [58,114]. It gives guidance on setting integrity operating windows, selecting material, the effects of stresses, effects of heat treatment, and incubation time guidance for HTHA [58]. The code uses the Nelson Curves (figure 15) as its fundamental guidance for HTHA. Over the years, API has made multiple changes to the Nelson curves by adding more points and lowering the curves to address newly found HTHA in metals. In the API RP 941 8TH Edition of the code, significant changes were made to the Nelson Curves by the addition of 12 data points and the introduction of a new curve that addresses post-weld heat-treated carbon steel material [58,115].

2.4.2.2 ASTM G142-98 - Standard Test Method for Determination of Susceptibility of Metals to Embrittlement in Hydrogen Containing Environments at High Pressure, High Temperature, or Both

This code provides a test method to determine the tensile property of a material when subject to a hydrogen environment under certain pressure, temperature, or both. The test consists of putting a specimen of material inside an autoclave, introducing hydrogen gas, and applying temperature while pulling the specimen to failure in uniaxial tension [116].

2.4.2.3 API 571 - Damage Mechanisms Affecting Fixed Equipment in the Refining Industry

API 571 offers guidance on materials that are affected by HTHA, critical factors to consider when evaluating HTHA, potential units that are susceptible to HTHA, crystallographic pictures of HTHA damages (figure 8), and prevention/inspection guidance [2].

2.4.2.4 API 579 – Fitness for Service (FFS)

API 579 provides an in-depth calculation on how to evaluate certain types of damages. The 2016 version is divided into 14 parts. These parts have several steps such as data requirements, techniques, and acceptance criteria (Level 1 assessment, Level 2 assessment, and Level 3 assessment), remaining life assessments, remediation, in-service monitoring guidance, and documentation to perform a complete FFS [117]. The code recommends starting with a Level 1 assessment (most conservative and easiest) and so forth until the calculations are within the acceptable range [117]. Level 3 is based on numerical techniques such as Finite Element Analysis or experimental techniques [117].

2.4.2.5 API 580 (Risk-Based Inspection) &API 581 (Risk Based Inspection Technology)

The risk-based inspection (RBI) codes offer guidance for an inspection program using risk-based methods [118,119]. API 580 and API 581 are to be used in conjunction with each other. API 580 provides minimum general guidelines for RBI and API 581 provides the calculation methods. The RBI method consists of focusing on process equipment with the highest risk and providing data information for inspection frequency, level of inspection, and the recommended NDE method. API 581 divides itself into two parts. Part 1 consists of the inspection planning to evaluate the probability of failure, the consequence of failure, risk analysis, and inspection planning based on risk analysis for a different type of equipment. Part 2 consists of the

determination of the probability of failure in which it evaluates the damage factor of the equipment. The damage factor tries to quantify the amount of damage equipment has accumulated over time, this provides screening criteria and determines inspection priorities.

2.5   Inspection Methods

The three stages of HTHA consist of 1) Decarburization of the metal due to the CH4 bubble formation on the grain boundaries, 2) Development of micro-cracks that affect the mechanical properties of the metal, 3) Material failure [120]. Inspection methods have been developed to detect HTHA before stage 3, and preferably before stage 2 progresses dangerously[120]. However, inspection methods capable of detecting HTHA in stage 1 are still lacking. HTHA can be detected either by non-destructive testing (NDT) utilizing an ultrasonic wave testing method by a qualified inspector in the field or by inspection of metal samples in a laboratory setting. Even with all the advancements in NDT tools, early-stage detection of HTHA is still considered challenging. This is due to the very small initial metal defects, localized affected areas, subjectivity of the analysis, etc. Usually, two or more combinations of inspection methods are used to detect HTHA [121] to eliminate the limitations of an individual method [58]. API RP 941 Appendix E provides a list of several NDT methods that can be implemented to inspect for HTHA with their respective advantages and limitations. The variability of manual ultrasonic inspection is highly susceptible to the reliable interpretation of the raw data by skilled inspectors [122]. There have been many inaccurate inspections resulting from faulty instrument calibrations, inaccurate probe selection, or inaccurate interpretation of inspection results. HTHA detection accuracy is highly dependent on human factors. Thus, it can be argued that NDT inspections tools currently rely too much on subjective human interpretation. Ahmen Yamani [122], presented a process that yielded promising results to resolve this issue. The project consisted of creating a database of ultrasonic A-scan

signals from various known HTHA defect areas utilizing a SONATEST Mastercan 340 flaw detector, compression wave probes, and calibration blocks [27] (see figure related to a block diagram representing the data acquisition system used). The data was obtained from an out-of-service pressure vessel known to have HTHA by utilizing several different technicians to acquire the data [27] (see figure related to out-of-service pressure vessel used to collect the data). Then the A-scan signals were uploaded to a single computer. Each defect had its own database with an assigned classification. The extraction process to verify the presence of HTHA and assign a classification is based on the principal component analysis. This method separates the relevant information from all the data noise, then allowing a computer trained classifier to accurately distinguish between different flaws in the material.

2.6   Ongoing efforts and challenges to prevent HTHA failure

2.6.1   The complexity of H interactions with steel alloys

One of the things that makes H unique is that it can have both positive and negative effects on the properties of metals [123]. Twenty-seven forms of negative effects are produced on the material structure and properties of the alloy due to hydrogen interactions with HE being the most prominent [124]. The maximum permissible concentration of hydrogen (C_p) has been used in many studies to help determine the effect of hydrogen brittleness on metallic materials [123]. C_p = C_{cr}/n where C_{cr} is the critical concentration of hydrogen where hydrogen brittleness starts to develop, and n is a factor that's related to the degree of importance of the structure, manufacturing process, and service conditions [123]. In the opinion of the author of [125], a hydrogen concentration of less than 2 cm^3/100 g will eliminate the negative effect of hydrogens on the properties of the steel.

26

The embrittlement effects of hydrogen can be reduced by the following methods [123]: 1) reduction of the absorption of hydrogen to a minimum, beginning with melting the ingot, 2) introduction of inhibitors into the hydrogen-bearing working media, 3) depositing a protective coat onto the metal, 4) annealing, especially a vacuum one, aimed at diminishing the concentration of hydrogen in the metal to a safe value; 5) alloying and reduction of the content of harmful impurities to diminish the susceptibility of the metal to hydrogen brittleness; 6) using thermomechanical and heat treatment to create a structure that diminishes the sensitivity of the metal to hydrogen.

Producing a model that captures all of the hydrogen's effects on steel alloys is extremely complex [67],yet a simplified model may leave out key mechanisms and fail to properly access H's effects. Due to its size, there are multiple H trapping sites and locations in which H can reside and eventually affect the steel in multiple ways [28]. As can be seen in [27] (see figure related to different hydrogen trapping sites in steels), H can be in vacancies, dislocations, grain boundaries, voids, precipitates, and their interfaces, etc. [126]. Small quantities of hydrogen concentration are sufficient to cause failures in metals because they can amplify its effect by migrating to regions of high triaxial stress [36]. Hence, simplified models need to be based on micro-mechanisms exhibiting the most pronounced effects under the considered conditions [67].

2.6.2   Nucleation stage detection of HTHA

NDT methods capable of detecting HTHA during stage 1 would greatly enhance failure prevention. This is particularly significant because the nucleation stage can often have a much longer duration than stage 2 in which cracks begin to form. Thus stage 1 detection increases the chances that the component is tested between the time at which HTHA is first detectable and the time at which failure occurs. Direct detection of the CH_4 bubbles present in stage 1 without destroying the component is a challenge because of their extreme localization and small volume.

27

2.6.3   Dataset limitations in empirical modeling

Another difficulty in assessing danger due to HTHA is the relatively small dataset of components that have failed while in service under the same operating case scenario. Empirical models such as the Nelson curves (figure 15) require large amounts of data indicating reliably what temperatures and partial pressures various alloys can withstand without HTHA failure. Since many of these components fail suddenly after many years of service, it is difficult to assemble sufficient reliable data. Additionally, there is insufficient data to accurately access the dependence of HTHA on other factors such as loading conditions, fatigue, cold working, time of service, PWHT, laminations, impurities, and H concentrations. Also, the HTHA mechanism occurs at high temperatures and affects many materials in diverse ways [77] [51]. These kinds of experiments can become very costly and time-consuming.

Ideally, new Nelson curves should be developed including all of these effects. Over time, the end-user would either establish new operating boundary conditions or upgrade to a more HTHA-resistant material. A combination of experimental data and computer model simulations can be used to establish more well-defined boundary parameters for the new curves. Curves that can predict HTHA susceptibility more accurately will minimize equipment damage and loss of production.

Many organizations such as Materials Testing Institute (MTI), API, Equity Engineering (E2G), Stress Engineering Services, Becht Engineering, etc. have been working on new development that can help better detect and predict HTHA [24]. These new developments have shown positive results. In 2012, a Joint Industry Project (JIP) was initiated with backing from more than nine refineries and petrochemical companies and managed by Equity Engineering to evaluate the repeatability of the existing HTHA inspection method found in API RP 941 [115,127].

Many specimens from components with known HTHA damage were gathered and evaluated by five international nondestructive testing companies [115]. The results from the data led to the development of new remaining life assessment guidelines (Buckeye Model) like the API 579 fitness for service methodology [24,114,115]. The Buckeye Model is time-dependent [114]. Stress Engineering has developed a predictive guideline that takes the existing temperature-hydrogen space from API RP 941 Nelson Curves and transforms them to a new time/temperature parameter-methane pressure parameter curve [24]. Becht Engineering has its HTHA Action Prioritization Method that considers many factors such as time, PWHT, applied stress, etc. [24].

2.7 Conclusions

The preliminary findings of the molecular dynamics are slightly different from the experimental approach. For CH_4 to form, a saturation of H and C has to be present with a minimum void size of 11.1 Å. CH_4 will repel each other if their distance is less than 3 Å. Due to the bonding strength, C and H will bond to Fe if the distance between them is less than 3.5 Å. The molecular dynamic approach to HTHA provides greater insight into the movability and formation of CH_4 inside the structure which cannot be seen under the empirical approach. Catastrophic failures have occurred leading to fatalities in the oil and gas industry, even though the failing components were thought to be operating at safe working limits regarding the Nelson curves. The Nelsons curves need to be revised to capture all the effects of hydrogen in the steel and hence reduced the likelihood of premature equipment failure. Current definitions of safe working limits are based on past failures of components under similar conditions rather than a deeper understanding of the materials science involved. A better fundamental understanding of the HTHA process is needed so that better predictive models of HTHA damage can be developed to avoid failures. Additionally, better methods of detecting early-stage HTHA are needed so that damaged components can be

identified reliably and replaced before failure. We believe molecular dynamic research can produce insights that may eventually enable replacing the fully empirical methods used now with physics-based damage model.

CHAPTER III

FAILURE ANALYSIS OF A M7X1 HIGH-SPEED STEEL TAP

This chapter is adapted from our previously published article: Mike Bodden Connor,

Morgan Calhoun, Matthew Cohen, Douglas Lum, Magee KaJuana, Sean Toellner, Doyl Dickel;

Failure Analysis of a M7X1 High-Speed Steel Tap; Journal of Failure Analysis and Prevention

3.1   Introduction

High-speed steels (HSS) are governed by the American Society for Testing and Materials

(ASTM) A600 [128–130]. This standard provides guidance and minimum requirement for the

elements and manufacturing process. The American Iron and Steel Institute (AISI) established two

categorizations for the HSS: Tungsten-type (T) and Molybdenum-type (M) [128,130]. The term

high-speed comes from their ability to machine material at high cutting speeds [129], maintain

hardness at elevated temperatures (~500-600°C) [131], and achieve higher wear resistance. Both

types are iron-based alloys of carbon, chromium, vanadium, molybdenum, or tungsten, and in

some cases substantial amounts of cobalt [129]. This composition of carbon and alloy content

allows the tools to possess properties of high wear resistance, resistance to elevated temperature

softening effects, and good toughness [129,132]. They are available in a large variety such as

annealed, hot-rolled bars, plates, sheets, strips, cold-finished bars, or forgings [128]. The tungsten

HSS has seven metallurgical grade types ranging from T1 -T7 and T15 with minimum tungsten

ranging from 11.75%-21% [128]. The molybdenum HSS has seventeen metallurgical grade types

from M1-M4, M6-M7, M10, M30, M33, M34, M36, M41-44, M46-M48, and M62 with minimum molybdenum ranging from 3.25% - 11% [128,133].

The four most important properties of HSS are hardness, hot hardness, wear resistance, and toughness [129]. Hardness increases the ability of steel to resist penetration by a diamond-hard indenter, improves material life, and is primarily used for cutting very hard material [129]. Most HSS has a hardness ranging from 61-66 HRC but some tools such as the M40 and T15 can reach up to 69 HRC [129]. Hot hardness is the ability to maintain their properties at elevated temperatures [129,131]. Wear resistance is the ability to resist damage caused by abrasion driven primarily by the matrix hardness of the material which is affected by the precipitated M2C and MC carbides [129,130]. Toughness is the ability to resist permanent deformation before breaking [129].

Multiple alloying elements influence the HSS properties but the minimum requirements are carbon (the most essential element and the increase in concentration will increase the working hardness, elevated temperature hardness, and the complexity of the carbide bonding [130,131]), vanadium (increases the cutting efficiency of the tool and the wear resistance [129]), chromium (increases the overall hardness and toughness of the material [129]), tungsten (increases the wear resistance, hot hardness, and produces secondary hardening [129]), molybdenum (has a similar effect to the tungsten [130]). In HSS, when the tungsten is decreased, the molybdenum is increased [129]. Molybdenum has a lower melting point than tungsten which tends to affect the hardening range [129]. The most desirable molybdenum-based HSS is the M2, M3, & M4 [129,130]. They possess a high percentage of tungsten and molybdenum, which allows the hot hardness property to increase which can extend the life of the tool [129]. The HSS is made by an electric melting process [128], which produces a high voltage current that is utilized to melt steel [134]. HSS

(depending on the grade) has a preheat temperature between 732C-871°C, a tempering temperature of 538°C -552°C [128,133].

3.2   Tapping Tool

Machining tools are in high demand, which has led to the rapid and low-cost manufacturing process as well as high-quality products [135]. In 2021, Astute Analytica forecast the machine tools market to reach $95,169.1 million by 2027 (compound annual growth of 4.7%) [136]. Tapping is the action of cutting a thread in a drilled hole. The three known methods of tapping are by hand, using a mill, and using a lathe [137]. They can either be taper chamfer (7 to 10 chamfered threads), requiring less torque and normally used to start the threads, tapping through holes but due to the long taper, they cannot thread as close to the bottom of the hole [137]. Plug chamfer (3 to 5 chamfered threads) requiring moderate torque is often used in start-to-finish of through holes, however, it does not start threads as easily as the taper chamfer when used to tap closed-end holes (blind holes); sufficient space is necessary at the bottom of the hole for chips to collect [137]. Bottoming chamfer (1 to 2 chamfered threads) is used to thread holes closer to the bottom of the hole [137]. In [138], see the figure related to taper chamfer, plug chamfer, and bottoming chamfer tap that shows the difference between the chamfers via thread details.

Tap failures are a common problem with the primary contributing factors being manufacturing defects (design, metallurgy) and operating errors (handling, overusing) [139–142]. A factor that leads to tap wear or reduction of tool life is the friction produced between the tool and the part being worked on which can differ for each material [141,143,144]. The friction can also lead to an increase in the induced residual stress of the component [143]. These stresses are highest in the edge zone of the tool where the greatest contact occurs [145]. In [138] (see the figure

33

related to A new M7x1 HSS plug chamfer tap with the predominant parts labeled), shows the primary parts of a tap.

In the literature, there are few studies on the failure analysis of HSS. According to D.D.D.P Tjahjana [135], the failure of a super hard end mill HSS-Co was due to stress concentration and the micro defect caused by the manufacturing process which made elements distribution inhomogeneous. As reported by O. Vingsbo [145], the three high-speed steel grade (low, medium, high) failures are due to abrasive and adhesive wear in the chisel edge, crater, flank, and margin. V. Gnanasekaran [140] states the failure of the solid carbide cutting tool used in milling operations was due to the crater wear in which contact with the chips eroded the rake surface. Seunghyuk Hwang [139] shows that of 341 drill bits analyzed, the cause of failure was due to overuse with the most frequent failure mode showing chips on the bottom. Miroslav Zetek [146] demonstrated cutting tool life while machining Inconel 718, which was proportional to the radius of the cutting edges of the tool (a higher radius increased tool life).

This case study describes a torsional brittle fracture failure that occurred on an M7x1 HSS plug chamfer tap. The tap had never been used before and failed when too much torque was applied. It bottomed out, causing it to fracture into two pieces. This happened when the tap was being used to create threads in a steel brake caliper on a motorcycle [138] (see the figure related to the brake caliper as well as the location of tap failure). Before the failure, an M6 drill bit [138] (see the figure related to parts used before the failure) was used to create the hole diameter, and Tap Magic lubricant was placed on the M7x1 tap to assist with friction force reduction. A crescent wrench was used by hand to torque the tap throughout the process. The specimen broke into two pieces, separated at a 45° angle from one another (labeled as Shank diameter side and Point diameter side) which is indicative of a type of brittle torsional failure [138] (see figure related

to the fractured M7x1 HSS plug chamfer tap with a 45° fracture surface, distinguishes between the shank and point diameter side). A quarter inch of the broken tap was protruding from the hole post-fracture and pliers were used to extract the lower part of the specimen. The tap is a "Drill America Brand" purchased on Amazon. A failure analysis will be performed on the broken tap to determine the cause of failure and the potential torque value at which it failed. Multiple testing equipment was used, along with finite element analysis (FEA) to corroborate values.

3.3   Methods

3.3.1   Optical Analysis

A visual examination was performed on the failed tap to collect data before microscopic testing. Multiple pictures were taken with a digital camera and dimensions were obtained via a digital caliper. The tap is a plug chamfer tap that has the marking of M7x1 HSS and had 4 flutes measuring 7mm in diameter and 73mm in overall length. The tap did not present any other visual mechanical damage besides the fracture surface. The length of the fractured surface started at the first few threads after the shank and transverse the entire diameter of the tap via a 45° angle [138] (see the figure related to shank diameter side). Damage threads were more noticeable on the point diameter side [138] (see the figure related to point diameter side). The shank diameter was 7.93 mm, the thread diameter was 7.15 mm, from the square to the fracture surface was 41.92 mm, and from the point diameter to the fracture surface was 27.15 mm. Using a Keyence VR-500 3D Optical profiler, the fracture surfaces were examined more closely [138] (see the figure related to downward view of the tap fracture surface).

3.3.2   Hardness Testing

A Leco Rockwell Hardness Tester LR-300 TD was used to determine the Rockwell hardness C value of the failed tap and a new tap to compare their hardness to ASTM standard. To ensure hardness testing accuracy, the same procedure was followed with both the original and new specimens. The machine was first set to 150 lbs and calibrated by using the diamond tip Rockwell C-scale indenter on a material with known hardness. Both cylindrical specimens were held in place by a v-slot cradle to ensure stability. Six separate locations on the shank portion of the tap were tested, taking care not to press the indenter on the stamped M7x1 HSS lettering. Each result was noted before rotating and/or sliding the specimen to test a new location.

3.3.3   Fractography

Fractography examination of the fractured surface was accomplished by using a ZEISS Optic Gemini Scanning Electron Microscope (SEM) from the Center for Advanced Vehicular Systems (CAVS) at Mississippi State University. In preparation for fractography, the shank side of the tap was secured to an inspection plate via carbon tape and placed in the SEM machine with the fractured surface pointing vertically upward. The SEM was used to determine the crack initiation location and failure mode that led to the premature fracture of the HSS tap. All the SEM micrographs were taken at an accelerating voltage of 25 kV. The working distance for the imaging ranged from 13.7 to 16.8 mm. Magnification was done at 79X, 84X, 92X, 100X, 172X, 175X, 197X, 452X, and 1.88KX with a tilting angle of 0.0°.

3.3.4   Optical Emission Spectrometer

An optical emission spectrometer (OES) test was performed to determine the chemical composition of both the original and new tap (table 1 and table 2). This method was used primarily

to determine the weight percentage of the lighter chemical elements. The testing was done at the Anderson and Associates metallurgical lab in Houston Texas (Thermo Fisher/ARL 3640). The sample preparation consisted of removing a small piece of metal (transversal) from each tap and grinding them smoothly and shortly after inputting it into the machine.

3.3.5   X-RAY

To provide insight into whether the microstructure had any large manufacturing defects, a micro-X-ray computed tomography (CT) machine from CAVS was used on the failed piece (Nikon X-Ray CT XT H225). To prepare the test, the tap was secured inside the machine atop a foam base, with the threaded end and fracture surface facing upward to be exposed to the radiation emitted by the machine. The machine's rotating target feature was used to thoroughly examine the tap from every possible angle, capturing approximately 3,100 images in the process. The images were viewed using VGSTUDIO MAX 3.4.5 software, along with the generated model of the X-ray image to look for any defects. The software was then used to retouch the original translucent X-ray image and give it a solid texture to see the features of the failed tap more clearly.

3.3.6   Optical Microscopy

A Leica DM ILM microscope was utilized to better visualize the microscopical effect on both the original and new tap. The test was conducted by Anderson and Associates metallurgical lab in Houston Texas. A small section of each tap was removed (low-speed diamond saw) from the shank side of the taps and prepared following ASTM E3 (Standard guide for the preparation of metallographic specimens). Both surfaces were etched with a 3% Nital.

3.3.7 Torque to Failure

A torque to failure test was performed on a new unbroken tap of the same size from the same vendor to replicate the original failure (M7x1 HSS). Typically, a torsion test is carried out using special equipment per an appropriate ASTM standard. The specimen is placed in the testing machine vertically with clamping jaws located above and below where the specimen is placed. The lower jaw is stationary while the upper jaw rotates in a specified direction and is controlled by a stepper motor via a human-machine interface (HMI). The HMI outputs data including torque vs. angle of twist where torque to failure can be identified. However, due to the shape of the tap specimen, the typical torsion test machine's jaws could not appropriately secure the tap for the test. An alternative method was performed using a shop vice and inch-pound clicker torque wrench. The new tap was secured in the vice simulating the same depth as the original failed tap. The torque wrench was applied to the opposite end of the tap in 5 Lb-in increments until failure occurred to determine an exceptionally good estimate of the torque to failure value.

3.3.8 Finite Element Analysis (FEA)

To further examine the failure mechanisms of the M7x1 HSS tap, an FEA model was developed using the Abaqus FEA software [138] (see the figure related to the three-dimensional view of the model). The following assumptions were taken for this model: the shank side and point side were modeled as a rigid body, with no vibrational effects, homogeneous material, a static model, and an elastic model assuming no plasticity before failure. The mechanical properties were Young's modulus of 29000 kips and Poisson ratio of 0.29 [147]. The approximate global mesh size was 0.03. The dimensions were taken from the failed tap. The intent was to get a complete understanding of how the stress concentration, torsional shear stress, and load was being distributed along with the tap.

3.4   Results and Discussion: Original tap vs New Tap

3.4.1   Original Tap

The tap has over 2000 reviews on Amazon with a 4.5 out of 5-star rating (as of writing this publication). Most customers were satisfied with the product. However, a few of them experienced identical fractures in similar locations as described in this case study. This M7x1 HSS tap failed the first time it was used, which was consistent with what other customers stated occurred to their tap.

The M7x1 HSS tap is a hard and brittle material which is due to the elemental composition and heat treatment. The tap presented a 45° angle fracture surface that was produced as the tap bottomed out inside the steel brake caliper and additional torque was applied which led to the tap experiencing a torsional brittle failure. The crack originated in one of the flutes of the tap [138] (see the figure related to crack origin and crack growth direction). From the SEM data, the fine surface is indicative of brittle fracture and the rough surface as ductile failure [138] (see the figure related to the largest porosity, various porosities, and the ductile region). The M7x1 HSS tap used in this case study was a plug chamfer tap. This type of tap is not adequate for bottoming threads in a closed hole. It is noted that the tap was used incorrectly for the task at hand. The ideal process would have consisted of starting the threaded hole with a taper chamfer tap, proceeding with the plug chamfer tap to get closer to the bottom of the hole, then finalizing with a bottoming chamfer tap to create the last few threads at the bottom. The Nikon X-Ray CT XT H225 machine was utilized to determine if any inclusion, or other manufacturing defects were present throughout the tap [138] (see the figure related to an X-ray machine was used to examine the: threaded end of the tap, the tip with the fracture surface while slowly rotating, and side view of the tap on the end). Per ASTM A600, the HSS should be free of heavy scale, deep pitting, laps, porosity, injurious

segregations, excessive non-metallic inclusions, seams, cracks, checks, slivers, scale marks, dents, soft and hard spots, pipes, or any defects that would detrimentally affect the suitability of the material [128]. During the quality check of the fabrication process, any of the above-stated materials should be rejected [128].

The X-ray machine did not identify any noticeable defects in the rest of the tap. The X-ray showed the remaining parts of the tap to be a solid consistency [138] (see the figure related to images from the VGSTUDIO software show the original X-ray image of the fracture surface, and the retouched image to show increased details on the surface).

Per the chemical composition in Table 3.1, the original tap is approximately to M2 regular Carbon (T11302) Molybdenum type HSS. The hardness was 53 HRC which is below the 64 HRC for M2. From the optical microscopy in [138] (see figure related to original tap. Leica DM ILM microscope at 500x. Small and large cementite particle), the white spots are the cementite particles in the matrix. There are a few large cementite particles on the surface with two of them next to each other. Large cementite particles can affect the strength of steel which can lead to a reduction in hardness. Also, per [26], stress tends to be lower in smaller cementite particles and higher in larger cementite particles. We believe that the reason for the low hardness in this case study is related to the density and size of the cementite particles which more likely occurred during the austenitizing, quenching, or tempering process. Per ASTM A600, for the M2 to obtain adequate hardness, it must be austenitized for the proper amount of time. This time is dependent on if the HSS will be austenitized in a Salt Bath or controlled atmosphere furnace. For the Salt Bath, the sample is immersed for a minimum of 5 minutes and 5 to 15 minutes if it's in a controlled atmosphere furnace. The quenching may be done in oil or molten salt plus air cooling. In the salt

quench, the temperature should be in the range of 566 °C to 635 °C. The M2 HSS should be double tempered at 552 °C for 2 hours each cycle.

3.4.2   New Tap

To determine an approximate torque value at which the original tap failed, a series of calculations and a torque to failure test were performed on a new tap. Even though the new tap was bought at the same location on Amazon, same vendor, and of the same size as the original tap; it had an average of 64 RHC. In [138] (see the figure related to new tap. Leica DM ILM microscope at 500x. Small and large cementite particles), the white spots are the cementite particle. This new tap also presented large cementite particles, but they are more separated and visually appear smaller compared to the original tap. The chemical composition of the new tap in Table 3.2 was approximate to an M2 regular Carbon (T11302) Molybdenum type HSS which has a 64 RHC. No defect was noticed on the fracture surface.

Table 3.1   Original tap vs M2 regular Carbon HSS Chemical Requirements % [128]

Tap	C	Mn	P	S	Si	Cr	V	W	Mo
	%	%	%	%	%	%	%	%	%
Original	0.83	0.36	0.022	0.009	0.46	3.88	1.9	5.65	4.55
M2	0.78-0.88	0.15-0.40	0.03	0.03	0.2-0.45	3.75-4.5	1.75-2.2	5.5-6.75	4.5-5.5

Table 3.2   New tap vs M2 regular Carbon HSS Chemical Requirements % [128]

Tap	C	Mn	P	S	Si	Cr	V	W	Mo
	%	%	%	%	%	%	%	%	%
New	0.82	0.36	0.022	0.009	0.46	3.87	1.88	5.11	4.54
M2	0.78-0.88	0.15-0.40	0.03	0.03	0.2-0.45	3.75-4.5	1.75-2.2	5.5-6.75	4.5-5.5

The visual fracture surface characteristics of the torque to failure test performed on the new tap presented identical results to that of the original failed tap. The new tap was found to fail around 77 lb-in by using a clicker torque wrench [138] (see the figure related to torque to failure test using a clicker torque wrench, new failed tap), and the original failed tap with the crack originating from the valley of the threads. The new failed tap compares to the original failed tap. The two taps failed near the center where the thread cuts begin on the tap with remarkably similar lengths for each broken half. This makes sense as the sharp sudden changes and threads in the surface geometry contribute to stress concentrations in that area. An FEA model was performed to verify the torque to failure result and obtain the approximate stress concentration factor of the tap failure location. A fixed boundary condition was applied to the point diameter side (approximate depth as the new and original failed tap) and a moment force at the reference point (RP-1) on the top side of the tap. The 77 lb-in was used in the FEA model and the result of the failure location was consistent with the torque to failure on the new and original tap location [138] (see the figure related load and boundary condition and highest stress area).

The ultimate tensile strength was calculated using [148] by converting the HRC value to Brinell hardness (BHN) then using [149] to convert to tensile strength (psi). See table 3.3. This was done due to the high HRC value and most published conversion charts had tensile strength up to 59 HRC.

$$\text{BHN} = 43.7 + 10.92\text{HRC} - \frac{(\text{HRC})^2}{5.18} + \frac{(\text{HRC})^3}{340.26} \tag{3.1}$$

$$TS = 500 * BHN \tag{3.2}$$

Table 3.3   Hardness and tensile strength of the original and new tap

Component	Original tap	New tap
HRC	53	64
BHN	517.72	722.27
TS (psi)	2.58×10^5	3.61×10^5

As shown in [138] (see the figure related to region of highest stress); as the torque is applied, the highest Von Mises stress (σ) of 9.67×10^5 psi occurred at the valley of the thread at point A (first few threads), above the tensile strength of the new tap material (3.61×10^5 psi). In the flute area at point B, the stress is 3.225×10^5 psi. These two high-stress areas coincide with the potential crack propagation direction of the original tap. The highest torsional shear stress (S13) of 4.02×10^5 psi occurred in the valley of the thread [138] (see the figure related to highest torsional shear stress). The stress concentration factor (Kt) at location A for the new tap is 2.7 ($Kt = \frac{\sigma}{TS}$). This stress concentration factor was utilized to estimate the approximate Von Mises stress (σ) for the original tap. This came out to be 7.0×10^5 psi ($\sigma = Kt * TS_{or}$). The torque value in the FEA model was lowered until it approximated the estimated Von Mises stress. The potential torque to failure value of the original tap was approximately 56 lb-in, which is 27.3 % lower than the new tap (77 lb-in).

3.5   Conclusion

The tap in question failed in a brittle, torsional fashion. This follows the expected behavior of a cylinder under torsion, with stresses maximized at the surface. Brittle fracture behavior was evident by a 45-degree, smooth fracture surface along with rapid crack propagation, and lack of geometry deformation.

Both the original and new tap approximate to an M2 high-speed steel Molybdenum based per ASTM A600. The original tap failed at approximately 27.3% lower torque than what it should have been. The density and size of the cementite particle are more likely attributed to the reduction in hardness and strength of the original tap. The hardness testing between the original and new taps was~18% in HRC values which led to a converted tensile strength difference of ~27%. This difference in hardness values of the two specimens strengthens the assumption of poor-quality control in manufacturing this brand of taps.

As a result of this case study, the recommendation to the manufacturer is increased quality control to ensure consistent material properties (hardness) across their products. From an end-user standpoint, care should be taken to use the correct type of chamfer for the application to minimize the binding of the tap tip and subsequent torque overloading.

CHAPTER IV

MOLECULAR DYNAMICS OF HTHA

4.1   Introduction

High temperature hydrogen attack (HTHA) has been an issue for many years. Most of the

data regarding HTHA are experimental-driven. Even though this approach has been successful,

there are still much more things that the oil and gas industry does not understand about HTHA.

The regions that were considered safe (below the Nelson curves) have experienced a catastrophic

failure. An atomistic approach to understanding HTHA is important because it allows us to see the

molecular behavior of this damage mechanism and to calculate the required energy barriers for

each stage of reaction between the carbon-hydrogen atom, carbon-hydrogen molecule, and

methane (CH_4). The most asked question for HTHA has been why certain carbon steel material

experience HTHA failure quicker than others even though they are operating at the same

parameters. Our research consisted of performing Molecular Dynamics (MD) of HTHA to

understand this phenomenon and show the behavior of CH_4 in cementite structure from an

atomistic point of view in the MD timescale and using the Nudge Elastic Band (NEB) calculation

method. This approach allowed us to answer the time dependency of HTHA and understand the

different ways in which CH_4 can form. To do this, we separated our research into 4 objectives: 1)

Explore how can hydrogen get into the void of a cementite structure from a surface, 2) Explain

how Hydrogen can take Carbon out of a cementite structure, 3) Determine the effect of the density

level of Hydrogen on CH_4 formation, 4) Evaluate the rate of formation of CH_4 at different temperature and void size.

4.2   First principle of quantum mechanics work

To perform an atomistic simulation for CH_4 using LAMMPS software, a Fe-C-H interatomic potential is needed. Our original plan was to develop our Fe-C-H interatomic potential using machine learning. Machine learning requires a lot of data to be able to accurately predict the parameters for the potential. Unfortunately, we were not able to accurately determine all the behavior of iron (Fe) and therefore did not pursue the creation of the potential using machine learning. Below are some of the outputs that we obtained utilizing the first principle of quantum mechanics. This was obtained by using the Pseudo potential for C and H H.pbe-rrkjus_psl.0.1.UPF and ran in the quantum espresso software. The energy and bond length for the hydrogen molecule (H_2) was 0.74 Å at 4.59 eV (figure 4.1a), and for methane (CH_4) was 1.1 Å at 16.37 eV (figure 4.1b). These values agreed with the literature values (H_2 = 0.74 Å at 4.477 eV [150], CH_4 = 1.1 Å at 17.018 eV [151][152].
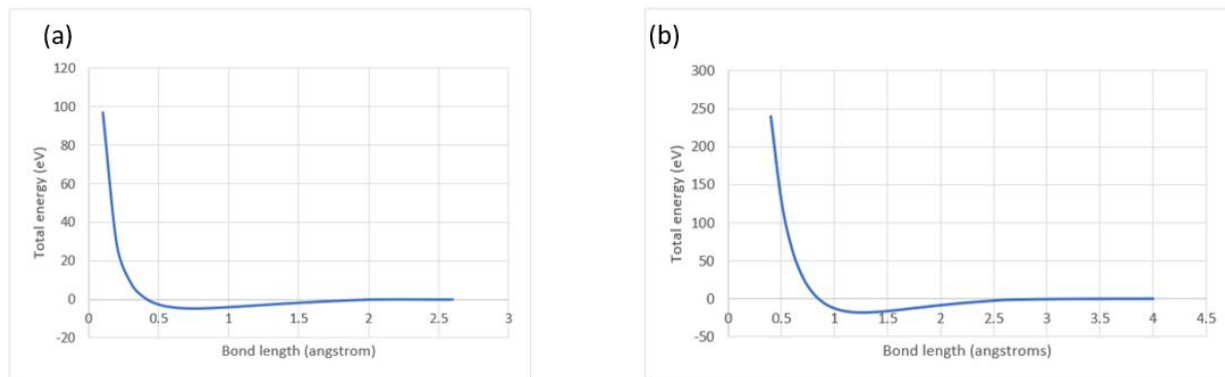

Figure 4.1   (a) H_2 energy vs bond length, (b) CH_4 energy vs bond length

For our research, we utilized a modified embedded atom method (MEAM) interatomic potential for the Fe-C-H. This is currently, the only potential of its kind developed at Mississippi State University. It was created using the Density Function Theory (DFT) to perform molecular dynamics (MD) using the Large-scale Modular Dynamics Simulations (LAMMPS) software. The primary purpose of this potential was to study the effects of hydrogen embrittlement in carbon steel material [151]. Since H embrittlement and HTHA are both H attack mechanisms, for our research, we are utilizing this potential.

To evaluate the accuracy of the MEAM potential (Fe-C-H) for HTHA, several small atomistic simulations were performed, and the potential energy and bond length for the hydrogen molecule (H_2), CH_4, and cementite (Fe_3C) were compared to the literature value. The input script for LAMMPS was separated into four main sections: Initialization, Atom definition, Force Field, and Setting.

```
# ----------------------- INITIALIZATION ---------------------------
units          metal
dimension      3
boundary       p       p       p
atom_style     atomic
neighbor 2.0 bin
neigh_modify delay 0 every 1 check yes page 500000 one 50000
# ----------------------- ATOM DEFINITION ---------------------------
read_data   atoms_coordinate.lmp
# ----------------------- FORCE FIELDS ----------------------------
pair_style      meam/c
```

pair_coeff   * * meamf_FeCH_new_lmp Fe C H meafile_FeCH_new_lmp Fe C H

------------------------ SETTINGS --------------------------------

Display thermo

thermo   1

thermo_style custom step pe

run   0

4.3   Cementite structure (Fe₃C)

CH4 can only form if there are Carbon (C) and Hydrogen atoms (H) available. The weight

% of C in most carbon steel metal for pipes and pressure vessels will form some type of cementite

(Fe3C) structure. This will be the same for grain boundaries. We can get C from solution but CH4

formation normally happens in the cementite structure [58]. Iron (Fe) is a body-centered cube

structure (figure 4.2a) while cementite is an iron carbide structure with layers of Fe and C (figure

4.2b). Fe3C has 16 atoms in the unit cell in which 12 are Fe and 4 are C [153], hence in our

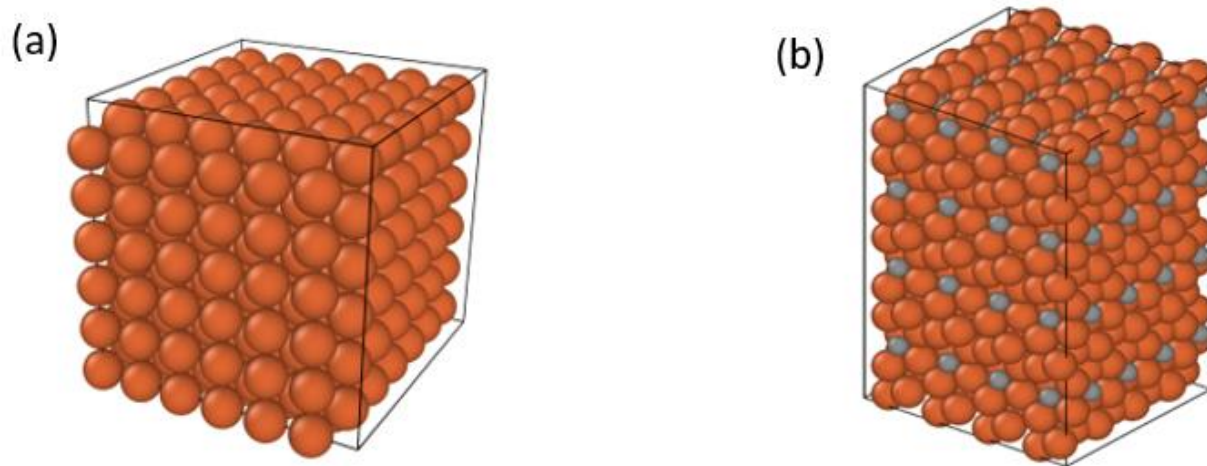research, we will focus only in this structure.

Figure 4.2   (a) BCC structure for Fe, (b) Fe₃C structure

4.4　Energy vs bond length curve for H_2 and CH_4

For this simulation run, a large box of dimensions X = 0, 17.0887 Å, Y = 0, 17.0887 Å, and Z = 17.0887 Å was created. For the H2 (figure 4.3a), two hydrogen atom was placed in the center of the large box with a separation distance of 0.3 Å up to 3 Å between them. For the CH4 (figure 4.3b), the four hydrogens were separated with equal space from the carbon from 1 Å up to 4.6335 Å. A minimization energy simulation was performed to determine the potential energy of the system and plotted verse the bond length (figure 4.4).
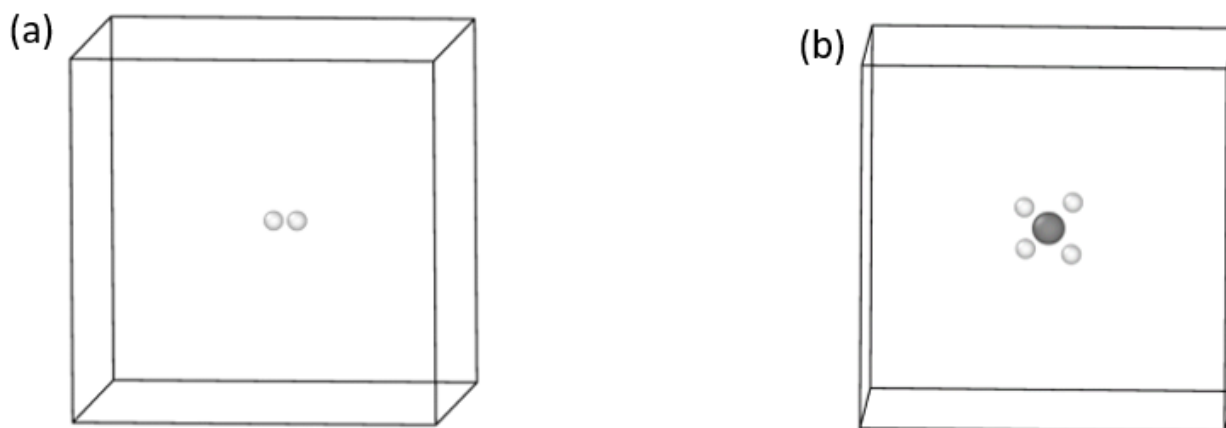

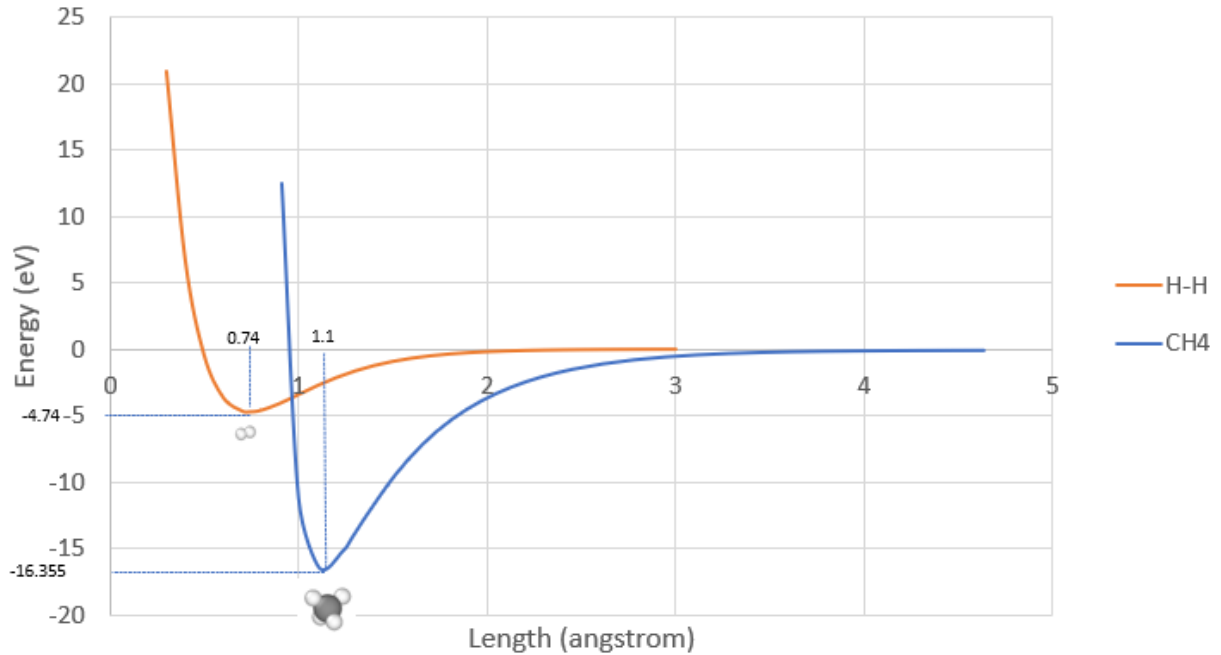Figure 4.3　　(a) H atoms separated, (b) C separated from 4 H

Figure 4.4   Energy vs bond length for H_2 and CH_4 with Fe-C-H MEAM potential

For the H_2, 0.74 Å and -4.74 eV were found. Each value agrees quite well with the literature value [151]. The bond length coincides exactly but the energy had a 0.434 eV difference. For the CH_4, 1.1 Å for the bond length coincides with the literature value [151] but the energy of -16.335 eV varied by 0.662 eV from the literature [151]. This difference in energy was used as guidance regarding our tolerance in energy value.

4.5   Energy vs Bond length for Fe_3C

The cementite (Fe_3C) structure has 16 atoms in the unit cell. 12 of which are Fe and 4 are C. The atoms coordinate (X=0, 4.49085 Å, Y =0, 4.03018 Å, Z = 0, 6.73931 Å) for the unit cell of the Fe_3C was obtained from Material API (figure 4.5). The unit cell was scaled from 0.81 to 3.5. The energy vs bond length was graphed via the X direction of the unit cell (figure 4.6). I obtained a bond length of 5.38 Å and -57.25 eV. The bond length differs from the literature [154] by 0.31 Å.
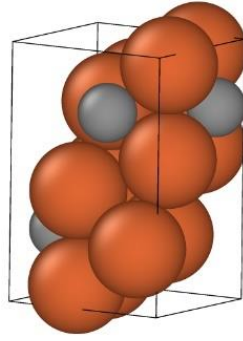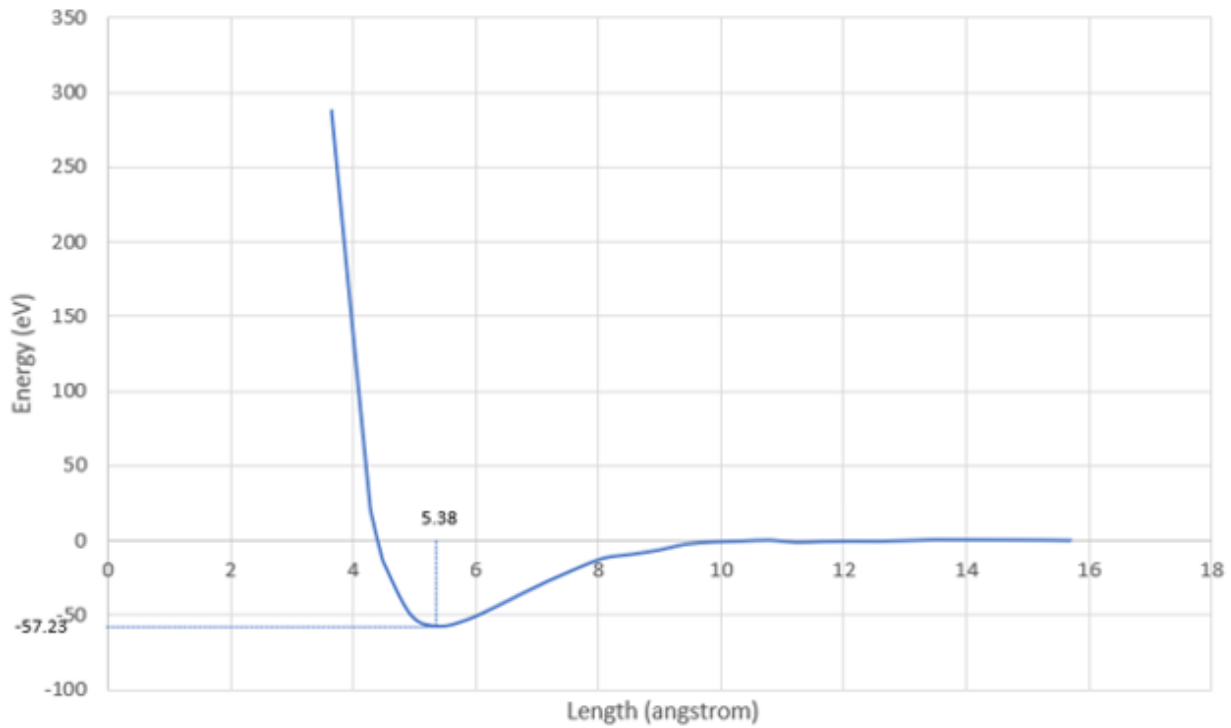
Figure 4.5   Fe₃C unit cell

Figure 4.6   Energy vs bond length of Fe₃C along the X axis

4.6   Nudge Elastic Band (NEB) Calculation

To perform an NEB calculation, you must first establish an initial and final configuration

of the structure. During the simulation run, the NEB determines the minimum energy path (MEP)

between the state of the structure[155]. This requires a finite number of replicas of the system to be constructed. These replicas can be produced by linear interpolation between the two end states [156]. Every two adjacent replicas are connected by a spring, mirroring an elastic band made up of beads and springs [156]. These beads in the band are normally equally spaced in a relaxation process due to the spring forces [156]. At any point along the path, the force acting on the atoms is only pointing along the path [155]. The maxima on the MEP are called saddle points or energy barriers [155]. The nudging operation process is related to the force projection that is needed to resolve the problems of corner cutting and sliding down that often arise with the plain elastic band method [156]. More information regarding NEB can be found in [155][157][158][159]. In the LAMMPS software, the NEB calculation method is activated by using [160]:

$$\text{Neb etof ftol N1 N2 Nevery file} - \text{style arg keyword} \tag{4.1}$$

etol = stopping tolerance for energy

ftol = stopping tolerance for force

N1 = max # of iterations (timestep) to run initial NEB

N2 = max# of iterations (timestep) to run barrier-climbing NEB

Nevery = print replica energies and reaction coordinate every this many timesteps

File-style = final or each or none

$$\text{Fix ID group} - \text{ID neb K} - \text{spring keyword value} \tag{4.2}$$

ID, group-ID are documented in fix command

neb = style name of this fix command

K-spring = spring constant for parallel nudging force

Zero or more keyword/value pairs may be appended

Keyword = parallel or perp or end

4.6.1   NEB Conversion Study: C-H bond

In conjunction with MD, the nudge elastic band (NEB) calculation was utilized to model

the behavior of CH_4 and try to determine the energy barrier that is required to form CH_4, break the

H_2 bond, and H diffusion into the cementite structure. Since this research is unique to its kind, it

was important to understand what would form first, either CH, CH_2, CH_3, or CH_4. To determine

this, a large box of coordinates X=0, 4.49 Å, Y = 0, 4.03018 Å, Z = 0, 6.73931 Å was used to run

a series of NEB calculations. Our first simulation consisted of putting one C and one H inside the

box (blue line) separated by 4.03 Å. The second simulation was one C and H_2 (one molecule,

orange line), our third simulation was one C and H3 (one H_2 and one H atom, gray line), and our

fourth simulation was CH_4 (two H_2, yellow line). See figure 4.7. In table 4.2 below, we see the

initial and final energy of each combination of hydrogen-to-atom reactions. During our simulation

runs, we notice that the CH_2 and CH_3 or CH_4 would form quicker than CH. This agrees with the

data as these values have lower final energy.

Table 4.1   Initial and final energies for 1C-H, 1C-2H, 1C-3H, 1C-4H

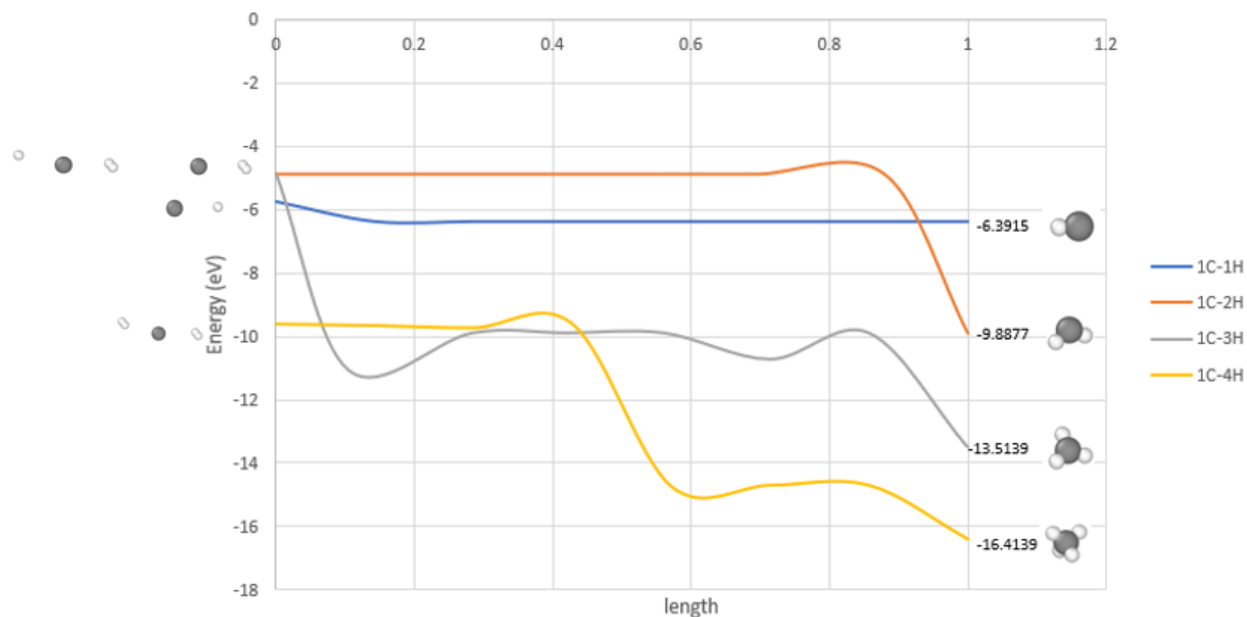| Molecule	Initial Energy (eV)	Final energy (eV)
CH	-5.74	-6.39
CH_2	-4.85	-9.89
CH_3	-4.86	-13.51
CH_4	-9.59	-16.41

Figure 4.7   NEB conversion study of C-H in a large box

Taking a closer look at the CH$_4$ formation in figure 4.8. Point A is where the H$_2$ starts to separate into the H atom. This took 0.47 eV. At point B CH$_2$ forms at an energy value of -5.15 eV. At point C, it took 1.23 eV to form CH$_3$ after CH$_2$ formation. At point D, it took -2.9 eV to form CH$_4$ after CH$_3$ formation. This final energy at point D (-16.41 eV) coincides with the minimum energy obtained in figure 3 with a differential of 0.055 eV.
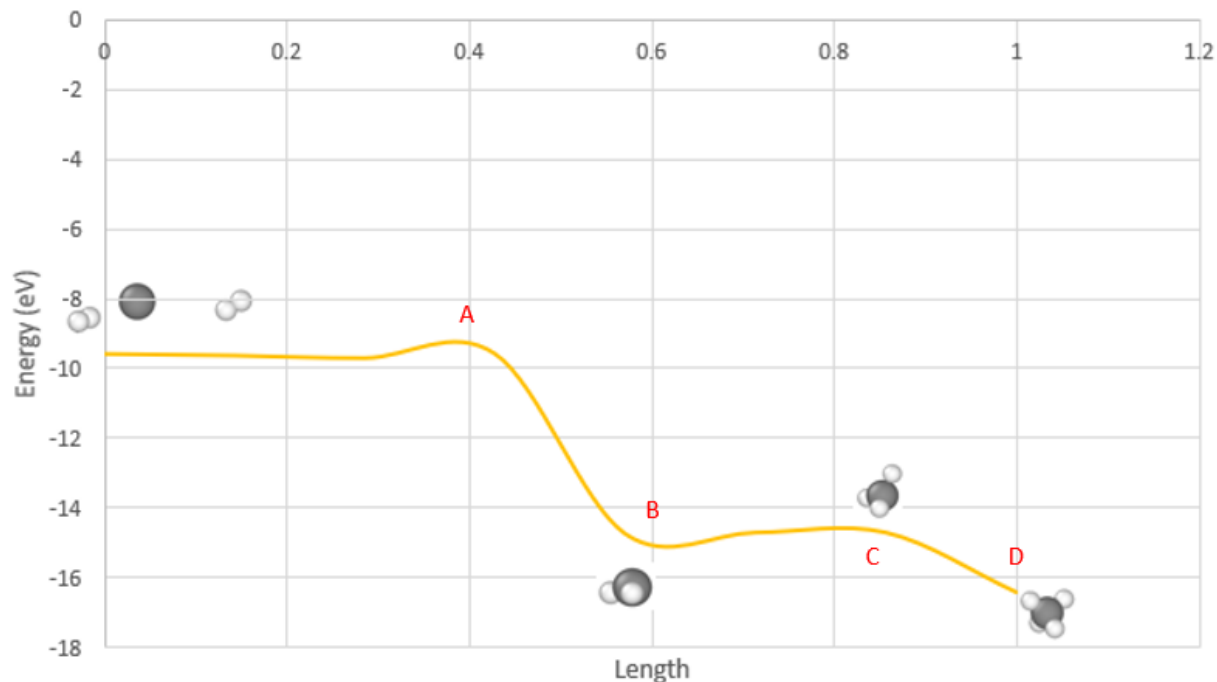
Figure 4.8   NEB of CH₄ formation

4.6.2   NEB Conversion study: CH₄ Replicas

To determine the correct number of replicas to use for our research, a conversion study was done by changing the replica numbers during the simulation run (figure 4.9). The box size was the same as in the previous section. We did 7, 8, 9, 10, and 16 replica simulations. All the replicas started at the same initial energy of -9.59 eV and had final energy of -16.41 eV (point D). Replicas 7, 9, and 16 had the highest energy at point C (CH_3 formation). Replicas 8 and 10 had similar behavior (points A, B, C, D), hence we chose these two replicas for our research study of HTHA.
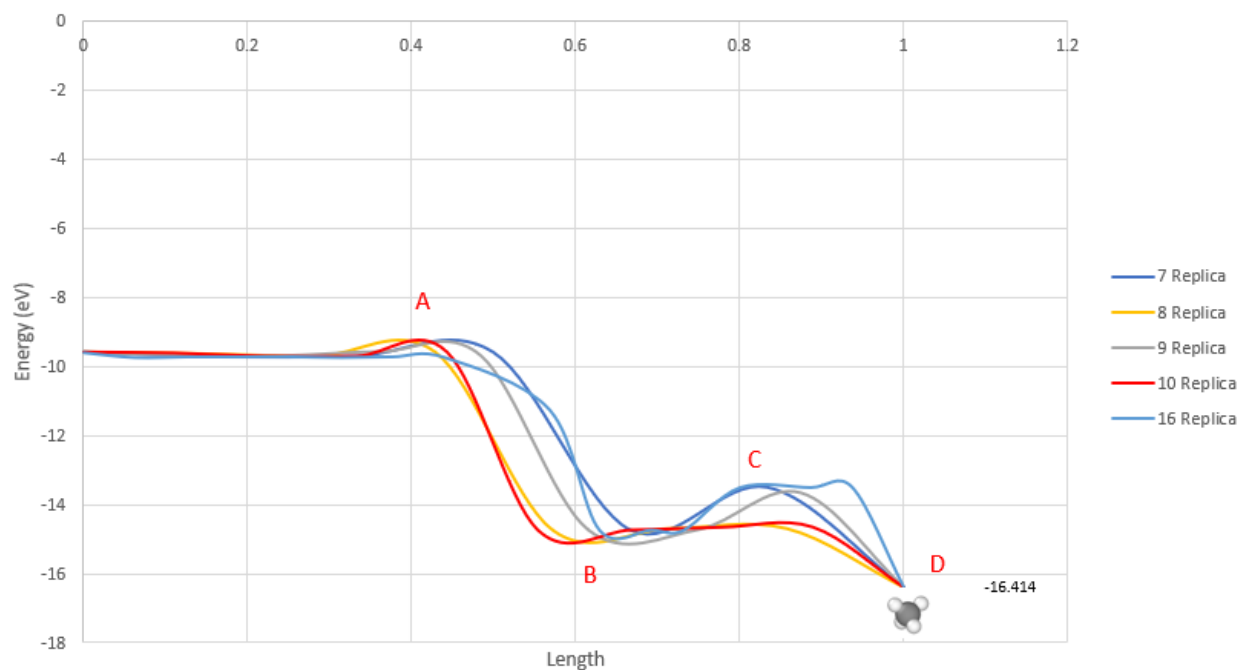
Figure 4.9   NEB replica conversion study

4.6.3   NEB Conversion study: CH₄ K-spring

The k-spring conversion study was done following similar patterns as the previous two conversion studies. See figure 4.10 below. We perform the study on K-spring 0.09, 0.1, 0.2, 0.5, 1, 2, and 5. The initial energy for all the k-spring conversion studies started at -9.59 eV and had final energy of -16.41 eV. All the k-spring that were lower than 2 had identical behaviors. K-spring greater and equal to 2 had a slight change in the graph. We utilized a K-spring value of 0.1 in our research for HTHA as the lower values had a more consistent behavior than the higher values.
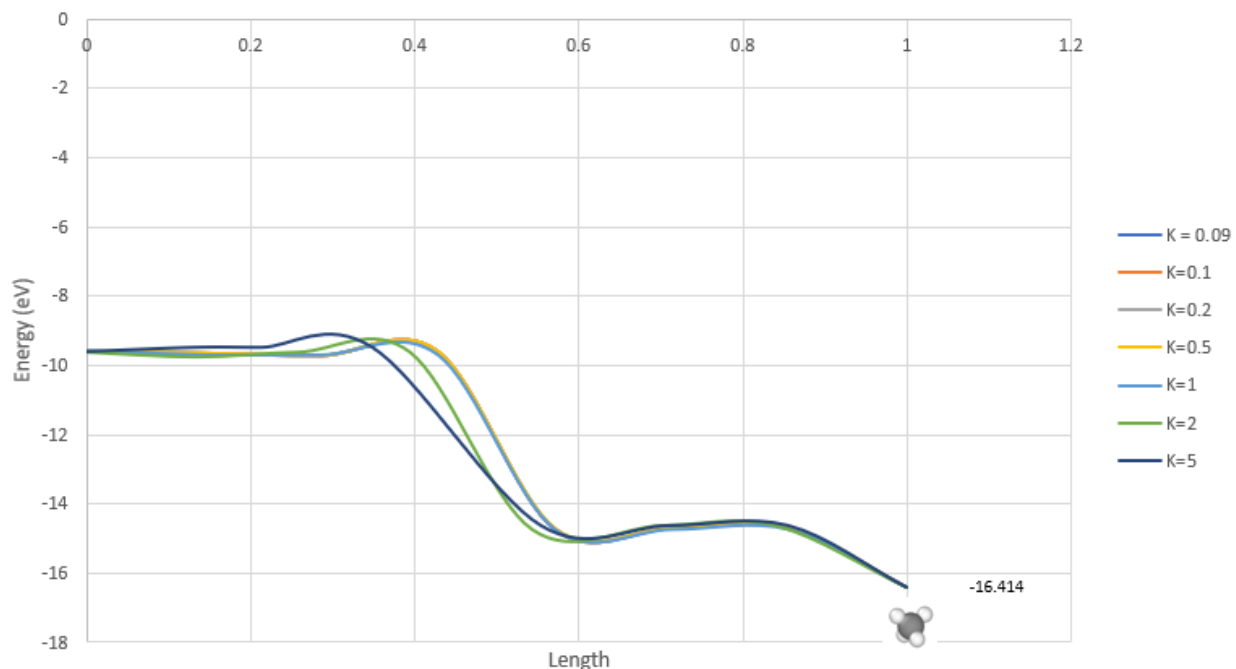
56

Figure 4.10   NEB K-spring conversion study

4.6.4   NEB Conversion study: CH_4 Timestep

A timestep conversion study was done to establish the timestep to be used in our research. Timestep of 0.0005, 0.001, 0.002, 0.005, and 0.05 was evaluated. As can be seen in figure 4.11, a timestep greater and equal to 0.005 change the behavior of the graph significantly. The smaller timestep showed better behavior than the higher time step. Timestep of 0.005, and 0.05 had a higher initial and final energy. At 0.2 length, the timestep of 0.002 had an energy barrier that was different than the 0.001 and 0.0005 timesteps. Timestep of 0.001 and 0.0005 had similar behavior except at point A. At this point, timestep 0.001 had a higher energy barrier (1.23 eV) compared to 0.0005. For our research, we used the smaller timestep of 0.0005.
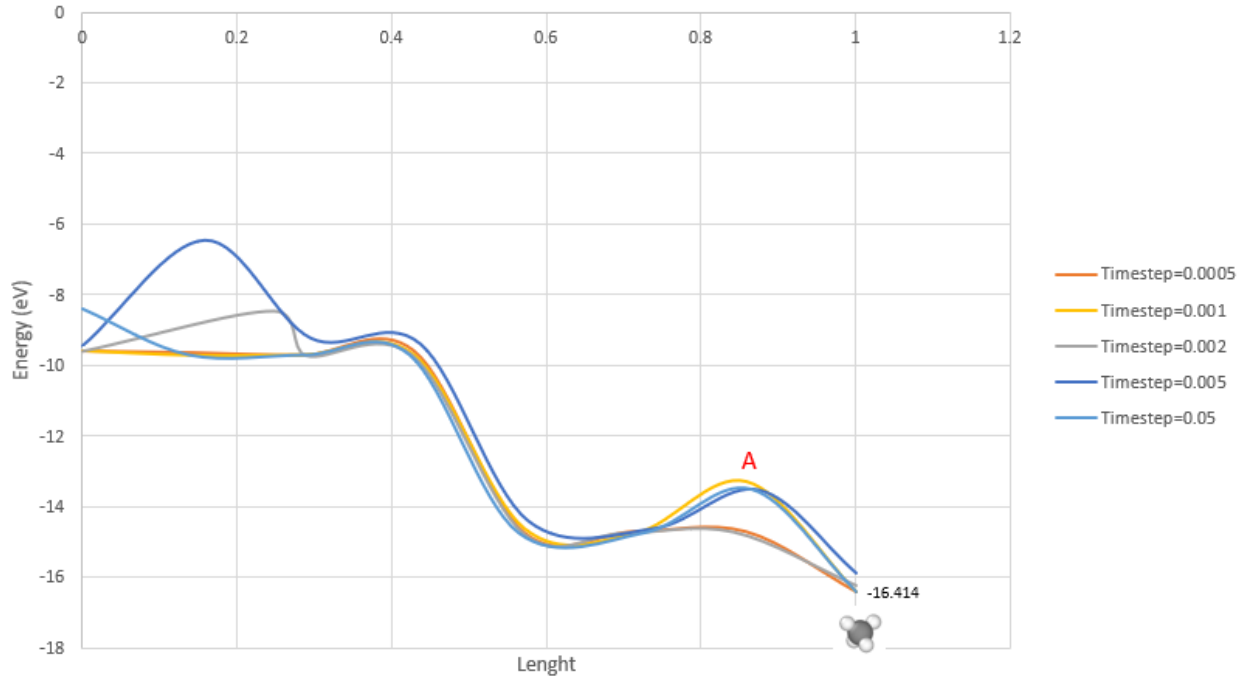
Figure 4.11   NEB timestep conversion study

4.7   Objective A: Explore how can Hydrogen get into the void of a cementite structure from a surface

To complete this objective, we utilized MD and the NEB approach.

4.7.1   MD approach

I created a large box of 1.8 MM atoms (Fe_3C) of dimensions X = 287.41 Å, Y = 257.93 Å, and Z = 215.66 Å. On the top surface of the Fe_3C, multiple H atoms were placed. We assumed that H behaves like an ideal gas, hence the PV=nRT (P = pressure, V = volume, n = amount of substance, R = ideal gas constant, T = temperature) equation was used to determine the number of H atoms that would fit on the surface at a determined H partial pressure and temperature. Per the Nelson curves, most HTHA issues occurred around 100-500 psia of H partial pressure, we chose 300 psia at four different temperatures (700F, 800F, 900F, 1800F) for the Carbon steel material.

58

The 1800F was done as a special case to evaluate the diffusion rate of H atoms into the steel. Note, carbon steel will not operate at these temperatures. All these temperatures are above the Nelson curves (not the safe operating zone of the curve). This was done to accelerate the diffusion process in MD. A large hole of 66 Å in diameter was placed 9 Å below the surface. Our goal in this objective was to get the H atom into the steel and ideally inside the void. We created a Python computer code to generate the random arrangement of the H atoms on the surface.

4.7.1.1   929 H atoms at 700F

The 929 H atoms were randomly distributed on the surface of the Fe_3C. The simulation was run for ~180,000 timestep. 52.6% of H atoms went to the surface of the Fe_3C. 2.2 H atoms became H_2, and 45.2% of H atoms went to the bottom surface (periodic boundary). I observed the H atom that diffused the deepest into the Fe_3C structure and plotted a depth-to-timestep graph of the atom. In figure 4.12, the H atom diffused the deepest into the Fe_3C structure above the void but slightly to the right. It was noticed that this H atom diffused ~ 6 Å in 20 picoseconds (0.3 Å/ps), after 60 picoseconds, it started to move around in different interstitial positions. If the simulation was given a longer run time, the H atom would eventually penetrate deeper into the Fe_3C and make its way into the void. Around the void outer surface, the atoms were deformed. This deformation created more space between the Fe_3C atom which allowed the H atom to penetrate deeper into the steel. Figure 4.13a shows the approximate location of the deepest H atom. This occurred closer to the center of the void. Figure 4.13b (Fe removed) showed the atom deformation around the void.
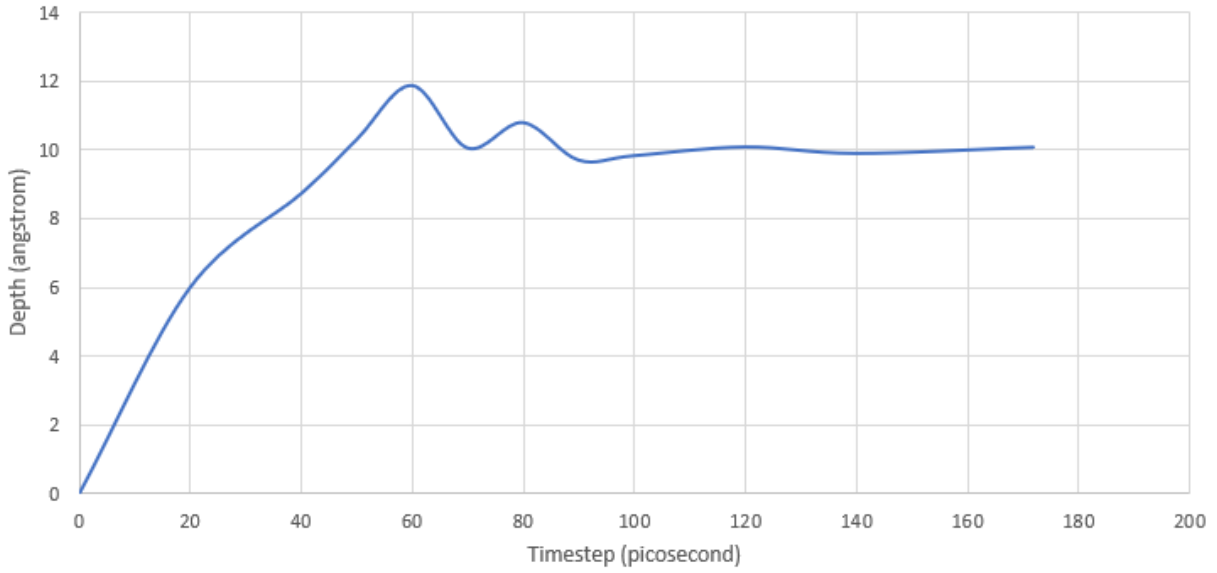
Figure 4.12   Timestep vs depth for H atom that penetrated the deepest into Fe_3C (929 H atom)
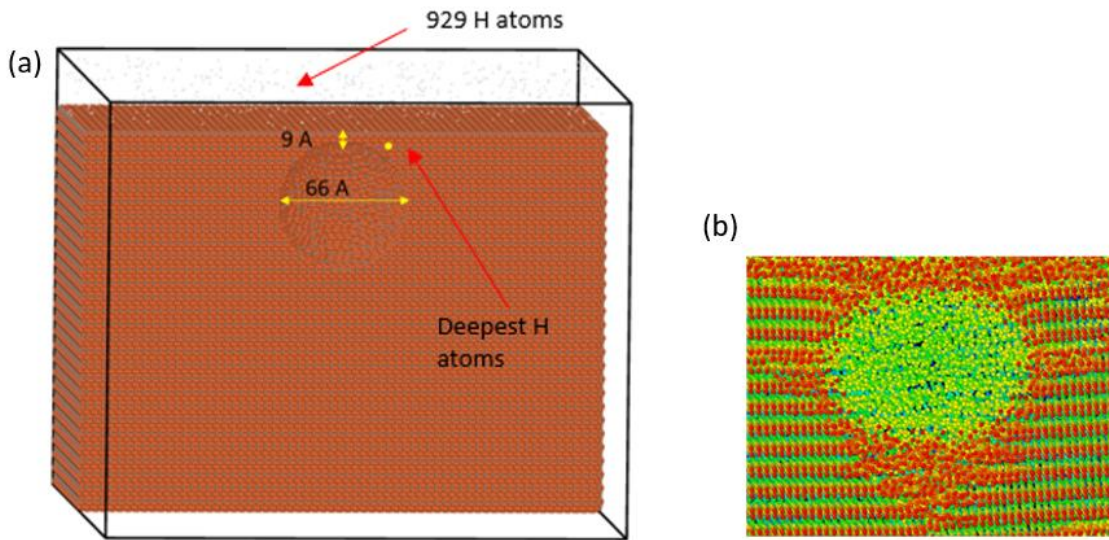

Figure 4.13   (a) Deepest penetration of H atom (929 H atom), (b) Deformation around void
(929 H atom)

4.7.1.2   856 H atoms at 800F

The 856 H atoms were randomly distributed on the surface of the Fe_3C. The simulation was run for ~180,000 timestep. 51.4% of H atoms went to the surface of the Fe_3C. 2.6 H atoms became H_2, and 46% of H atoms went to the bottom surface (periodic boundary). Figure 4.14 shows the path of the H atom that penetrated the deepest into the structure. The H atom travel ~1.7 Å in 10 picoseconds (0.17 Å/ps). This H atom occurred in the back side of the structure (figure 4.15a) but not above the void. In this region, the Fe_3C was not deformed as above the void. This prevented the H atom from penetrating deeply into the Fe_3C structure. As can be seen in figure 4.15b (Fe removed), as the temperature increases the deformation around the void also increased.

Figure 4.14   Timestep vs depth for H atom that penetrated the deepest into Fe_3C (856 H atom)

Figure 4.15   (a) Deepest penetration of H atom (856 H atom), (b) Deformation around void (856 H atom)

4.7.1.3   792 H atoms at 900F

The 792 H atoms were randomly distributed on the surface of the Fe_3C. The simulation was run for ~180,000 timestep. 54.7% of H atoms went to the surface of the Fe_3C. 1.8% of H atoms became H_2, and 43.6% of H atoms went to the bottom surface (periodic boundary). Figure 4.16 shows the path of the H atom that penetrated the deepest into the structure. The H atom travel ~2.2 Å in 14 picoseconds (0.16 Å/ps). This H atom occurred in the back side of the structure (figure 4.17a) but not above the void.

In this region, the Fe_3C was not deformed as above the void. This prevented the H atom from penetrating deeply into the Fe_3C structure. As can be seen in figure 4.17b (Fe removed), as the temperature increases the deformation around the void also increased.
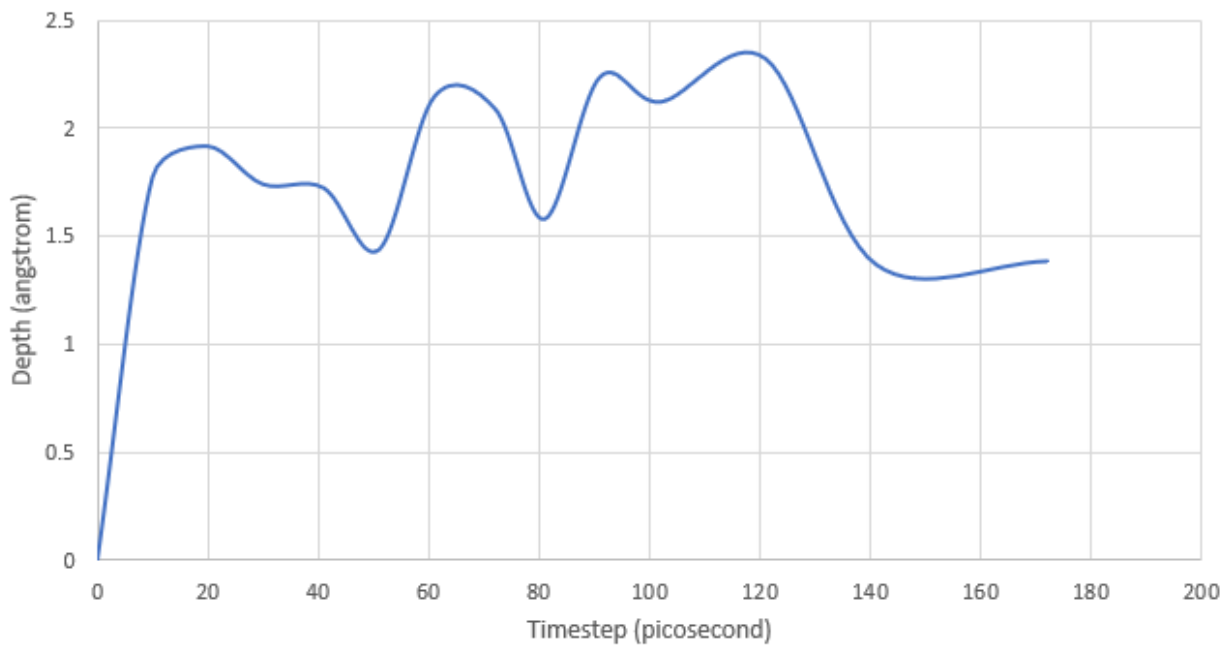
Figure 4.16   Timestep vs depth for H atom that penetrated the deepest into Fe₃C (792 H atom)
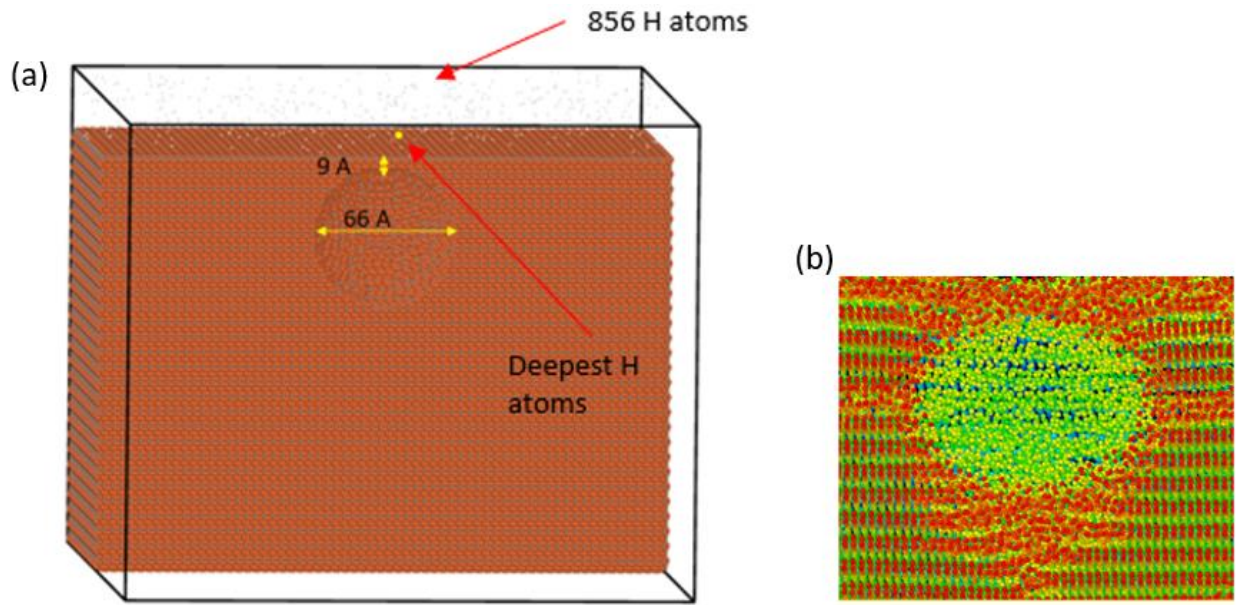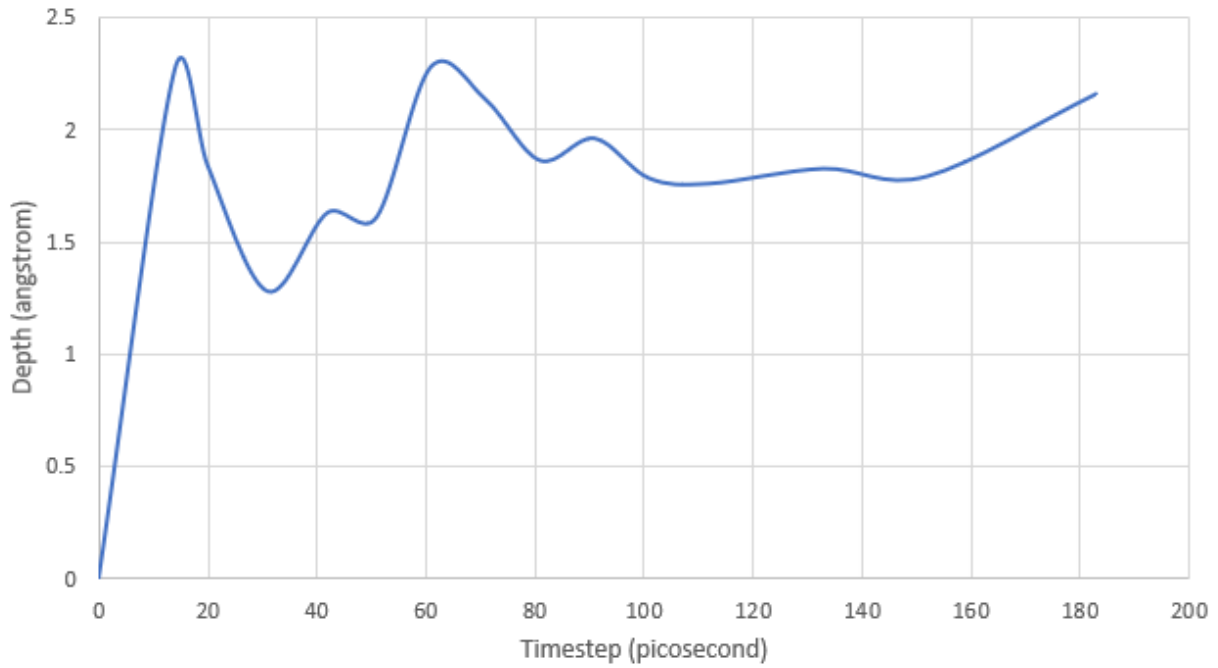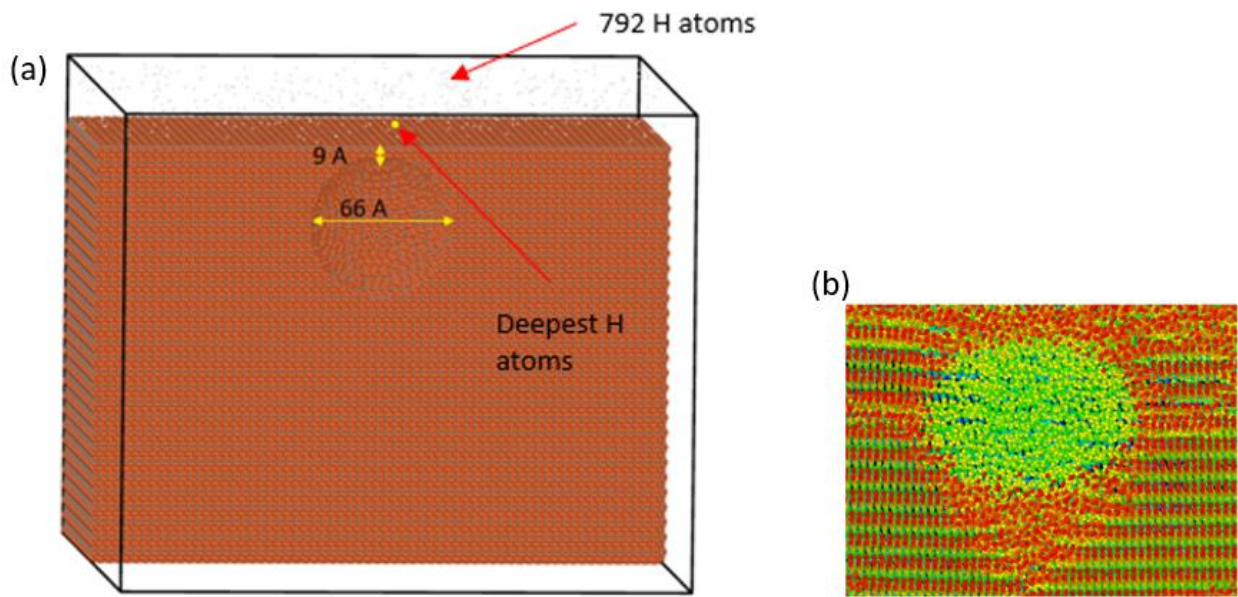

Figure 4.17   (a) Deepest penetration of H atom (792 H atom), (b) Deformation around void (792 H atom)

63

4.7.1.4   792 atoms at 1800F

The 792 H atoms were randomly distributed on the surface of the Fe_3C. The simulation

was run for ~100,000 timesteps. 48.48% of H atoms went to the surface of the Fe_3C. 0.008% of H

atoms became H_2, and 50.8% of H atoms went to the bottom surface (periodic boundary). Figure

4.18 shows the path of the H atom that penetrated the deepest into the structure. The H atom travel

~6 Å in 6 picoseconds (1 Å/ps). This H atom occurred in the back side of the structure (figure

4.19a) but not above the void. In this region, the Fe_3C was not deformed as above the void. This

prevented the H atom from penetrating deeply into the Fe_3C structure. As can be seen in figure

4.19b (Fe removed), as the temperature increases the deformation around the void also increased.
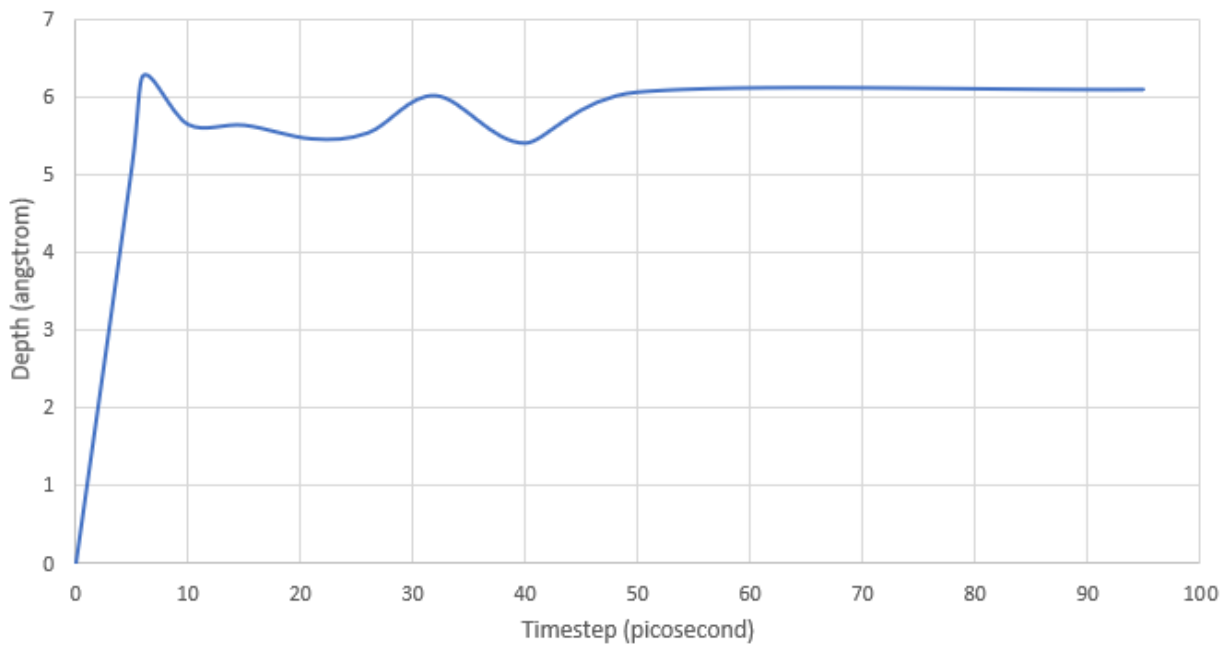
Figure 4.18   Timestep vs depth for H atom that penetrated the deepest into Fe_3C (1800F)
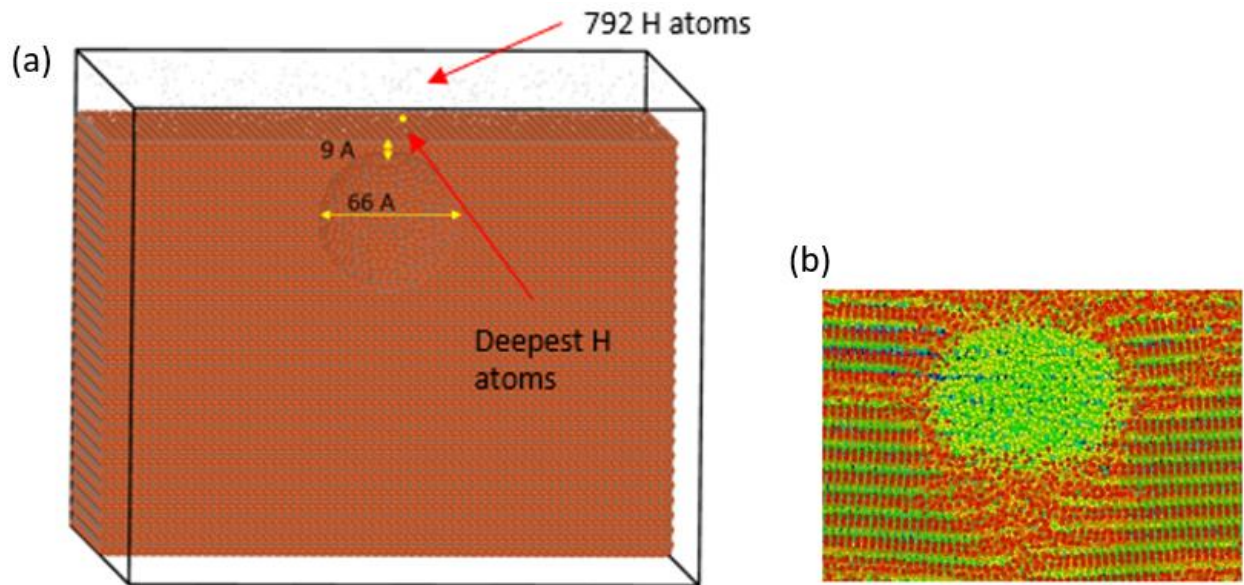
Figure 4.19   (a) Deepest penetration of H atom (1800 F), (b) Deformation around void (1800 F)

4.7.2   NEB approach: H_2 on Surface

To perform the NEB calculation, a structure of 674 atoms (672 Fe_3C and one H_2) was created. The box coordinates were X = -9.40, 9.40, Y = -10.11, 10.11, and Z = -21.25, 21.25. The H_2 was placed ~ 7.8 Å above the surface. The simulation was run and evaluated at the 10 replica case scenario. In figure 4.20 (10 replicas), the first energy barrier occurred at point A. This is when the H_2 separated into H atoms. It took 1.8 eV for this to occur. At point B, both H atoms lay on the surface. This required -2.53 eV. At point C, one of the H atoms diffuses into the steel to ~ 2.4 Å. This generated 1.85 eV. As can be seen, point D is 0.54 eV higher than point B. We believe this margin of error was due to the potential fitting parameter to H embrittlement instead of the HTHA parameter.
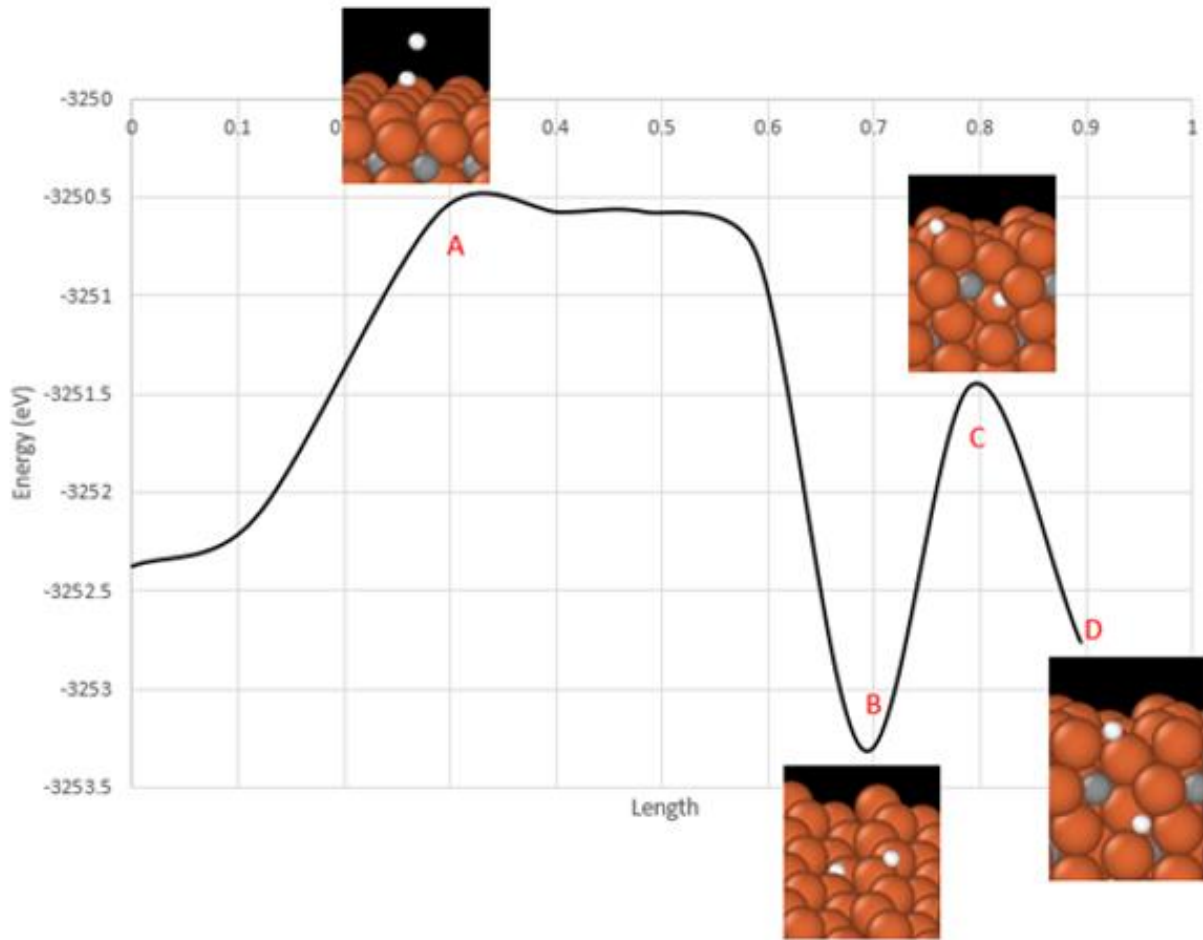
Figure 4.20   NEB of Fe$_3$C with H$_2$ on surface

4.7.3   Summary of objective A

The higher temperature created fewer H atoms in the volume space above the surface, less H$_2$ formation, more H atoms, faster H atom diffusion into the Fe$_3$C structure, and more deformation around the void. At lower temperatures, we had more H$_2$ formation and slower H atom diffusion into the Fe$_3$C structure. Overall, H diffuses into the structure in the MD time scale at all temperatures.

4.8   Objective B: Explain how Hydrogen can take Carbon out of a cementite structure

The goal of this objective was to extract Carbon out of the Fe_3C structure in the MD time scale. We created a large box of ~ 2MM atoms and put a void 56.42 Å in diameter at 78.7 Å from the surface and saturated it with H atoms (figure 4.21). The void was filled with 818, 951, 1307, 1595, 1846, and 2045 H atoms. The coordinates of the large box were X = 0, 287.41 Å, Y = 0, 257.93 Å, Z = 0, 215.66 Å. We did not follow the ideal gas law equation in this objective. A temperature of 700F at 300 psia H partial pressure was used. This temperature was above the Nelson curve. A python computer code was created to generate a random H atom position inside the void.

Figure 4.21   (a) Large box of 56.42 Å diameter fill with H atoms

During the simulation run, we were not able to get H atoms to extract carbon from the Fe_3C in the MD time scale. In the literature (API 941), CH_4 normally forms inside the metal structure
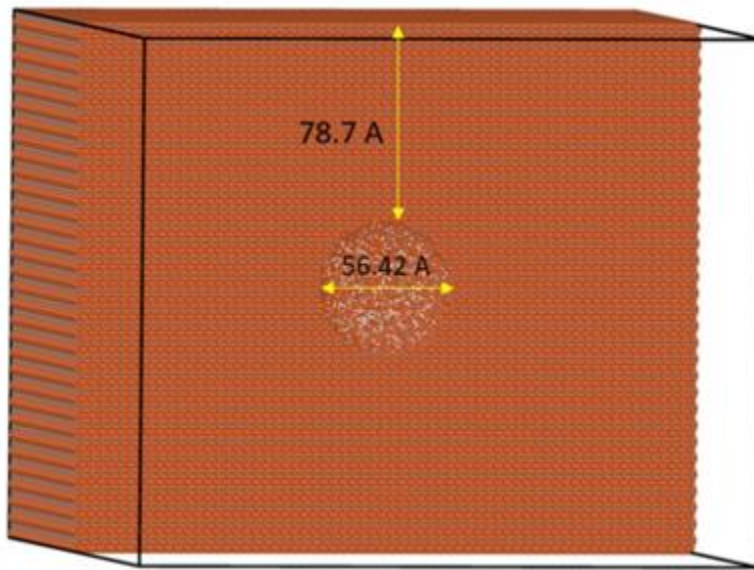
and rarely on the surface of the metal. We decide to use the NEB approach to determine the energy required to form CH_4 inside the void and on the surface.

4.8.1 NEB: CH_4 on the surface

A box of coordinates of X= -9.40, 9.40, Y = -10.11, 10.11, and Z = -21.25, 45 was created and we placed two H_2 at 8.36 Å from the surface. We ran the simulation and allowed the CH_4 to form at 5.5 Å from the surface (figure 4.22). The carbon in which the two H_2 would form was placed at 2 Ås beneath the surface. We performed a replication conversion study at 8, 9, 10, 11, and 13 replicas. In replicas 8, 9, and 11, the carbon jumped far above the surface. In replicas 10 and 13, the carbon diffused to the surface. Replica 13 had a different behavior than what we were expecting for the CH_4 formation. Therefore, we utilized replica 10 (black graph in figure 4.23) for our research. At point A in figure 33, 3.22 eV was required to bring the carbon to the surface. The highest energy barrier was 7.62 eV. At point B, -5.01 eV was required to form CH_2. It required -1.9 eV to form CH_4 from CH_2 at point C. We acknowledge that the final energy should have been lower than the initial energy. Point C has a difference of 0.69 eV from the starting point. As stated previously, this is due to the interatomic MEAM potential not being fitted for the HTHA parameter.
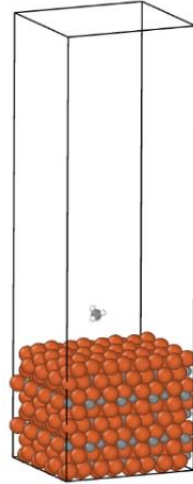
Figure 4.22   Fe$_3$C with two H$_2$ on the surface
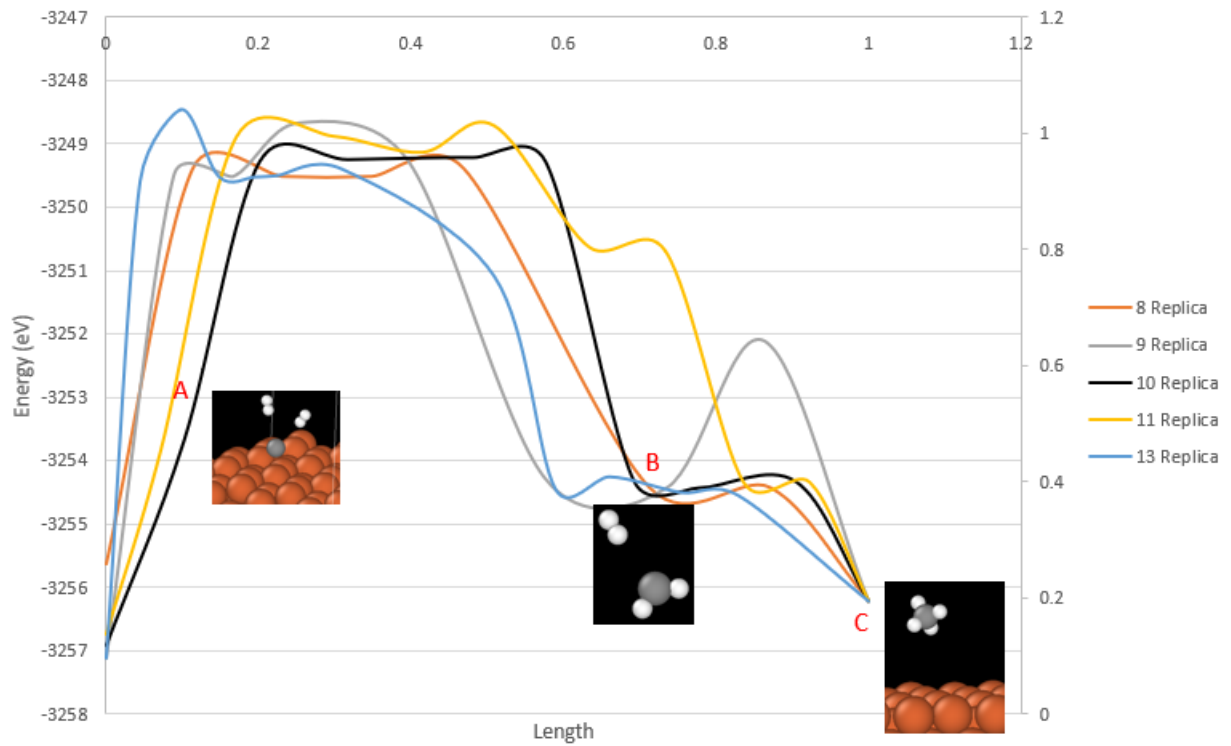
Figure 4.23   NEB replica conversion study of Fe$_3$C with two H$_2$ on the surface

4.8.2   NEB: CH₄ – Void inside the structure

A large box of coordinates X =0, 35.92, Y = 0, 32.24, Z = 0, 53.91 was created with 7641 atoms (Fe_3C). A void of 20 Å diameter was placed at 15.92 Å from the surface and two H_2 were placed in the center of the void (figure 4.24). Two different CH_4 formations were noticed. One at 8 replicas and the other at 10 replicas. In replica 8, we observed that one of the H_2 attached to the carbon while it was still attached to the iron forming CH_2. This happened when the H_2 was at 3.25 Å from the carbon. Shortly after, the CH_2 separated from the Fe_3C and form CH_4 with the other two H_2. As can be seen in figure 25, at point A, 0.267 eV was required for the first energy barrier and at point B, 1.17 eV was required to form CH_2 and 0.526 eV to form CH_4. We believe that is the most likely form of how CH_4 will form in a void. We acknowledge that the reason point C is higher than point B is due to the interatomic potential fitting process. In replica 10 in figure 4.26, we saw that the carbon separated from the iron and form CH_2 with one of the H_2, and shortly after it form CH_4. At point A, 3.02 eV was required for the CH_2 to form and 3.08 eV from CH_4.

Figure 4.24   Two H_2 in the void of replica 8
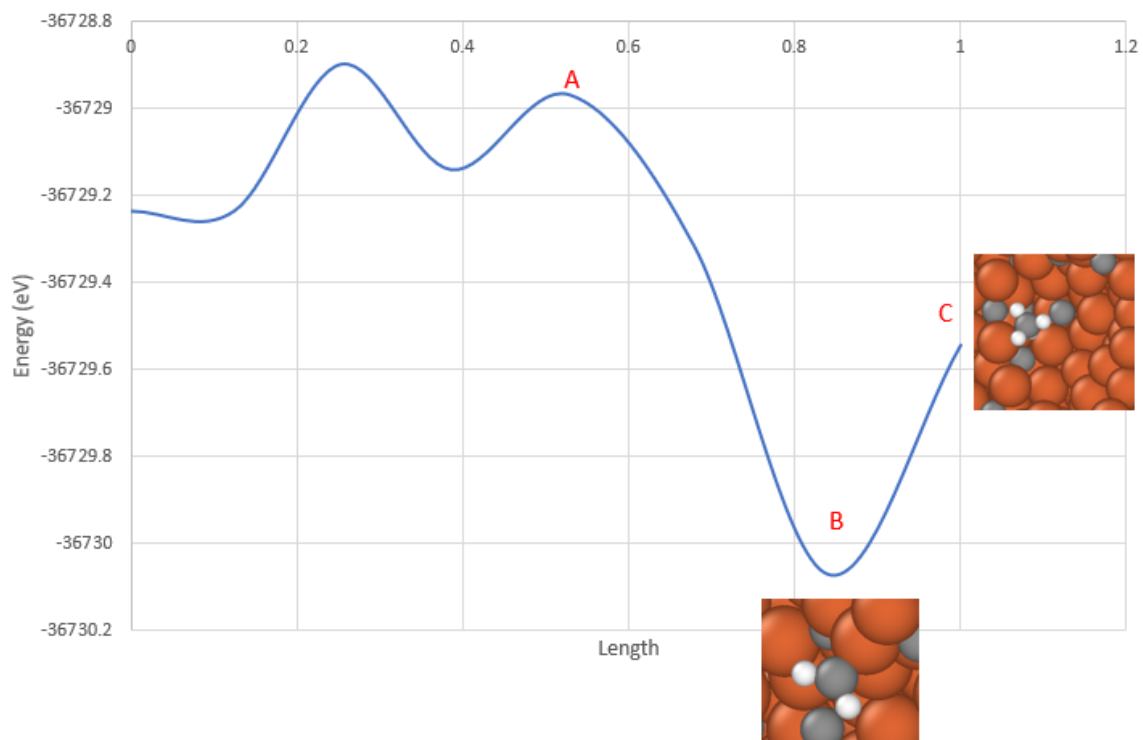
Figure 4.25   NEB of Fe₃C with two H₂ inside the void of replica 8
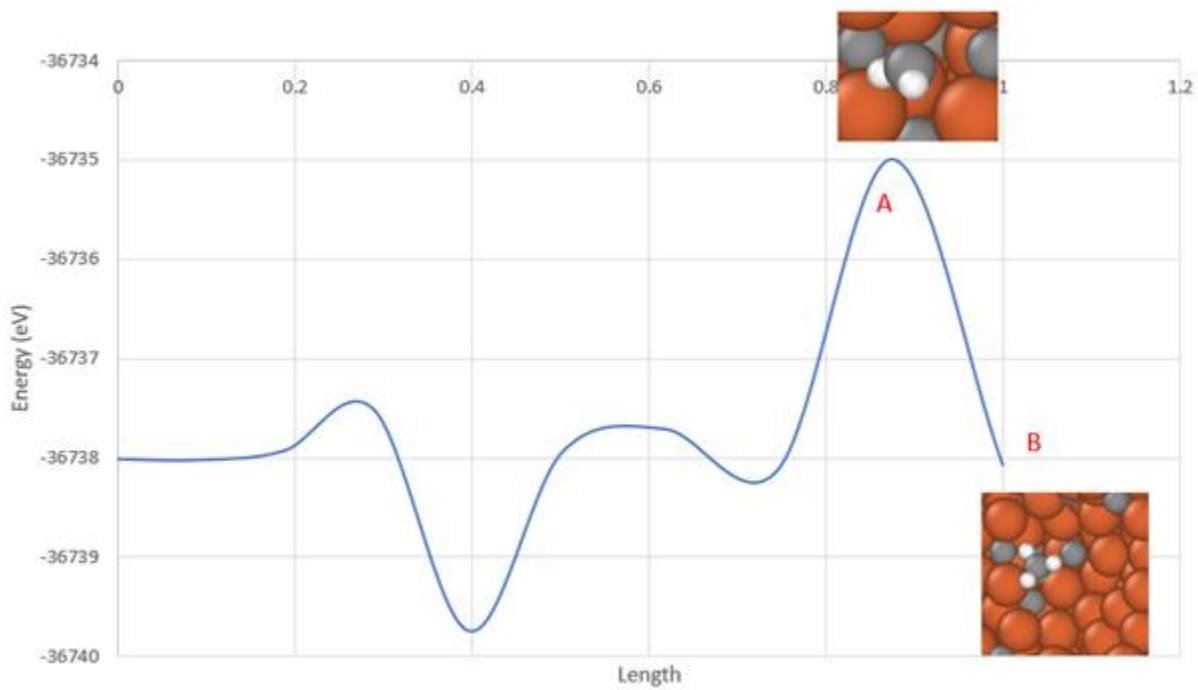
Figure 4.26   NEB of Fe₃C with two H₂ inside the void of replica 10

4.8.3   Summary of objective B

We did not obtain any results of carbon separating from Fe_3C in the MD timescale. CH_4 is more likely to form inside a void instead of a surface. As the surface require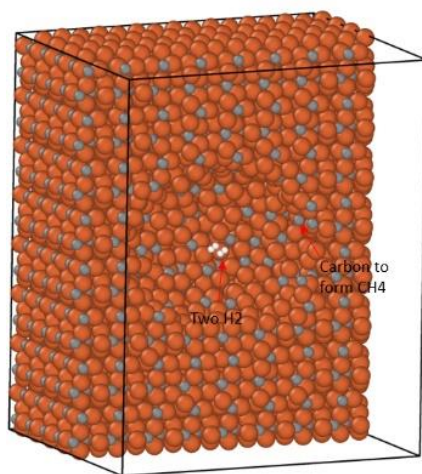d almost twice as much energy to form CH_4 compared to the void forming CH_4. CH_4 is more likely to form with one H_2 attaching to a single carbon atom, over time it will break the bond with Fe_3C and separate to CH_4 with another H_2.

4.9   Eyring Equation

One of the ways to use our data is to use the Eyring Equation. This equation is used to determine the rate constants from their free energy activation [161]. This also provides insight into how a reaction progresses at the molecular level [161]. It shows a relationship between rate and temperature. It's also considered a transition state equation that depends on the reactants' (starting position) and products (final position) state [161]. The equation works by using Gibbs free energy ($\Delta G = \Delta H - T\Delta S$). The lower the ΔG the faster the reaction rate [161]. The enthalpy (ΔH) is the energy barrier that can be taken from our research study and the entropy (ΔS) will have to be estimated from the Nelson curves experimental data. Using both values can determine the calculation of the rate constant for CH_4 formation. The Eyring equation [161]:

$$k = \frac{k_B T}{h} e^{-\left(\frac{\Delta G}{RT}\right)} \tag{4.3}$$

$$k = \frac{k_B T}{h} e^{-\left(\frac{\Delta H}{RT}\right)} e^{\left(\frac{\Delta S}{R}\right)} \tag{4.4}$$

k = rate constant

k_B = Boltzmann constant (1.381×10^{-23} J/K)

h = plank's constant (6.626 x 10^ -34 Js)

ΔH = enthalpy (J)

ΔS = entropy (J)

R = gas constant (8.3145 J*mol^-1*K^-1)

T =absolute temperature (K)

4.10 Objective C: Determine the effect of the density level of hydrogen on methane formation

The goal of this objective was to form CH_4 with carbon that is not bonded to the Fe_3C structure during the MD timescale. These carbons can be found in the void due to the manufacturing process. We created a large box of ~ 2MM atoms. The coordinates of the large box were X = 0, 287.41 Å, Y = 0, 257.93 Å, Z = 0, 215.66 Å. A void of 56.42 Å in diameter was placed at 78.7 Å from the surface (figure 4.27). We utilized a pressure of 300 psia and temperatures of 700F, 800F, and 1800F which are above the Nelson curve. We saturated the void with different quantities of H atoms and carbon atoms. 950H atoms with 1C, 6C, and 12C. 868 H atoms with 6C. 575 H atoms with 6C. The 1800F was done at 950 H atoms at 1C. Overall, we saw better results using 6C at the specified void size compare to the other carbon quantities.
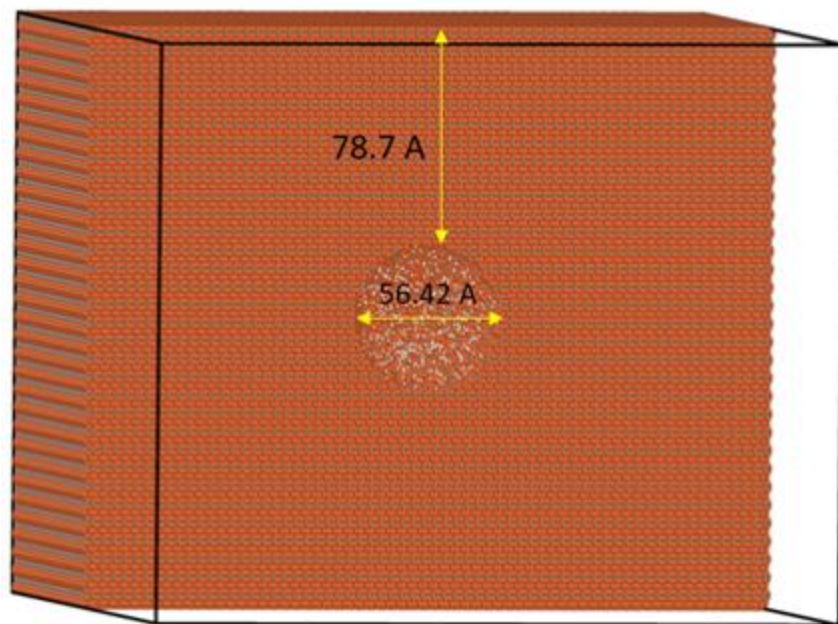
Figure 4.27   Large box of 56.42A diameter filled with H atoms at 700F, 800F, 1800F

Two approaches were taken regarding the H atom's proximity to carbon. The first approach consisted of placing the carbon atoms anywhere from 0.75-2.1 Å at different temperatures. We noticed that CH_4 formed during the minimization process (figure 4.28a). This is indicative that at close enough proximity, CH_4 can form independent of the different temperatures and at the same rate. The second approach consisted of placing the carbon atoms anywhere from 0.75-23 Å at 800F. We were able to form CH_4 at 2 ps. We noticed that CH_3 formed first, then it moved around the void and form CH_4 with the other H atom that did not diffuse into the Fe_3C structure or form H_2 (figure 4.28b).
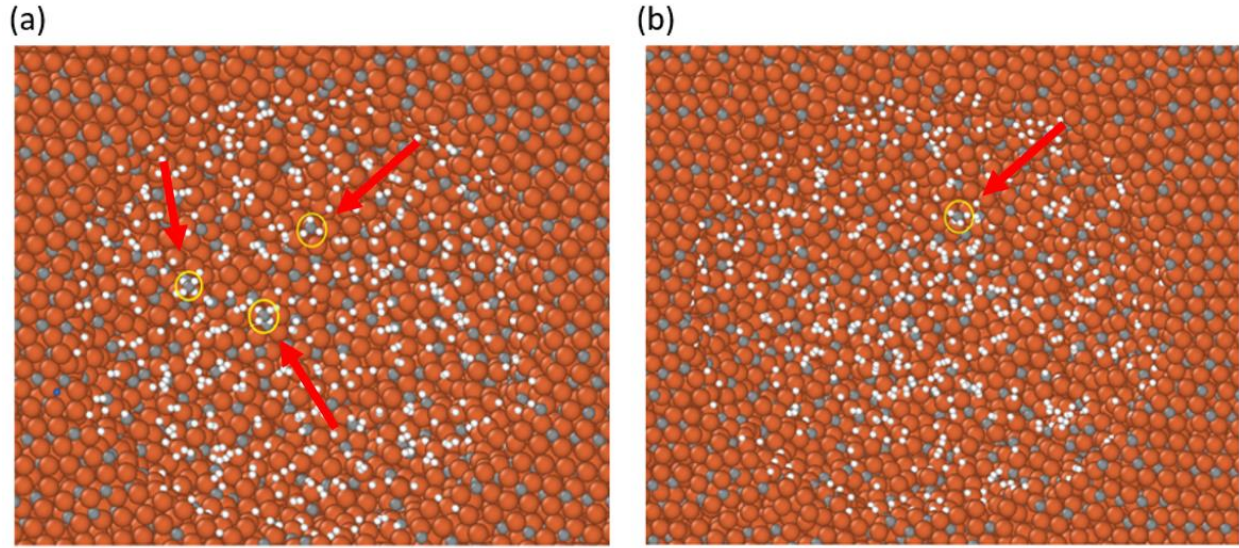
Figure 4.28   (a) CH$_4$ forms at 0.75-2.1 A from H atoms at 700F, (b) CH$_4$ forms at 0.75-23 A from H atoms at 800F

We also notice that over time, H atoms diffuse out of the void (figure 4.29). In figure 4.30 (700F), we graph the depth versus timestep of the H atom that penetrated the deepest into the Fe$_3$C structure. This produced a rate of 0.125 Å/ps. This was also done for the 1800F (figure 4.31, figure 4.32) which produced a rate of 0.35 Å/ps.
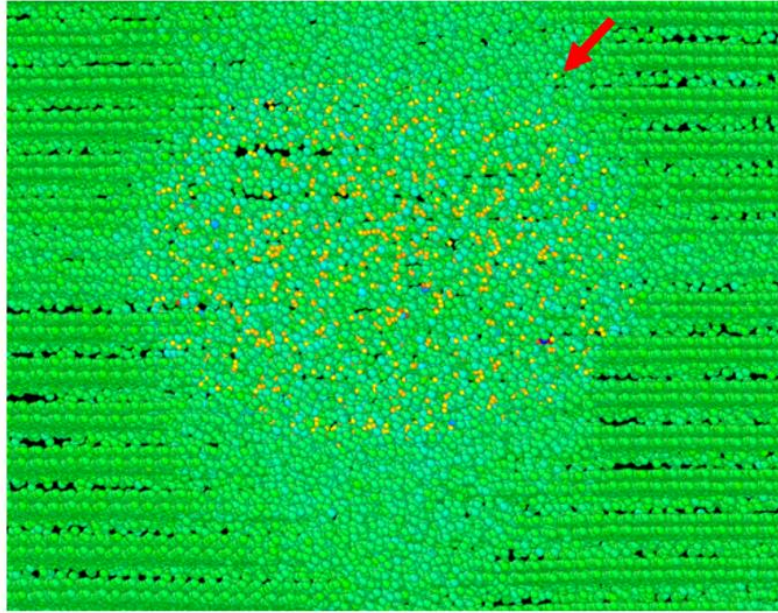
Figure 4.29   H atom defused out of the void at 700F
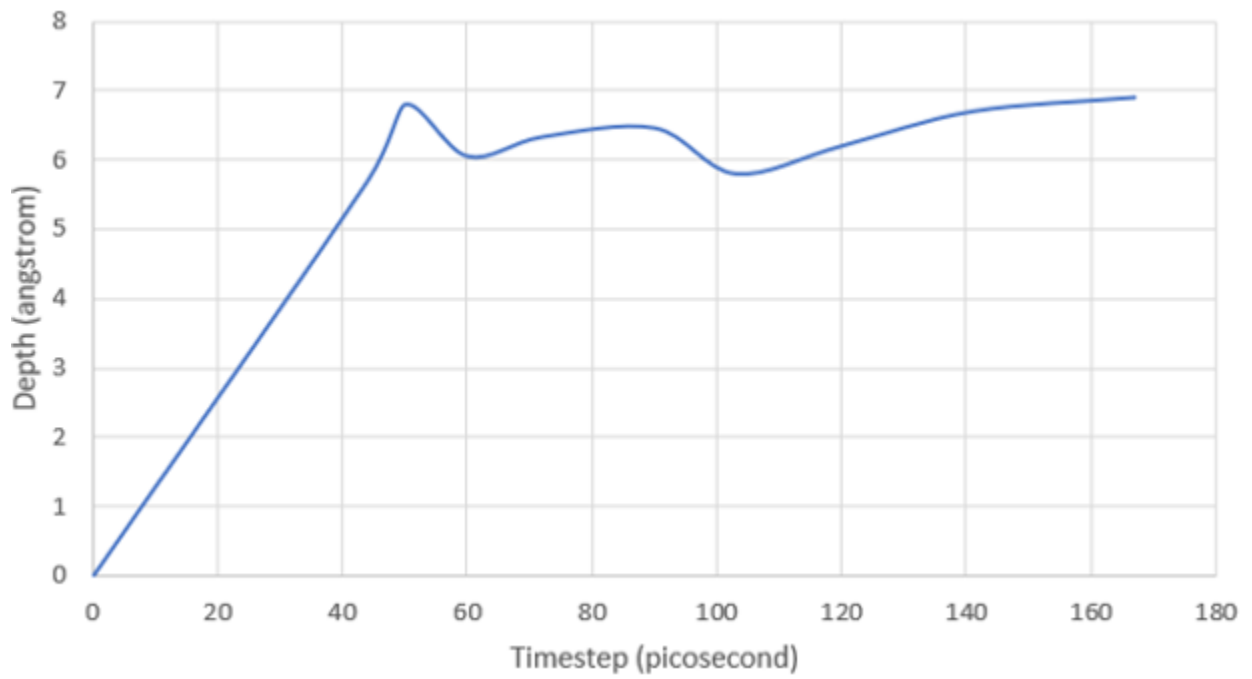
Figure 4.30   Timestep vs depth for H atom that penetrated the deepest into Fe$_3$C (950 H atom)
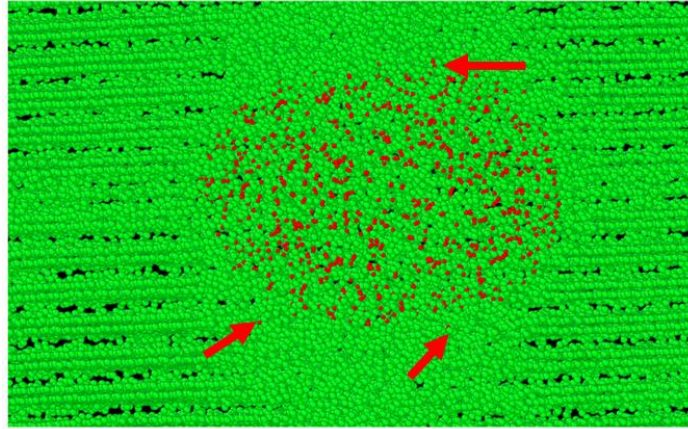
Figure 4.31   H atom defused out of the void at 1800F
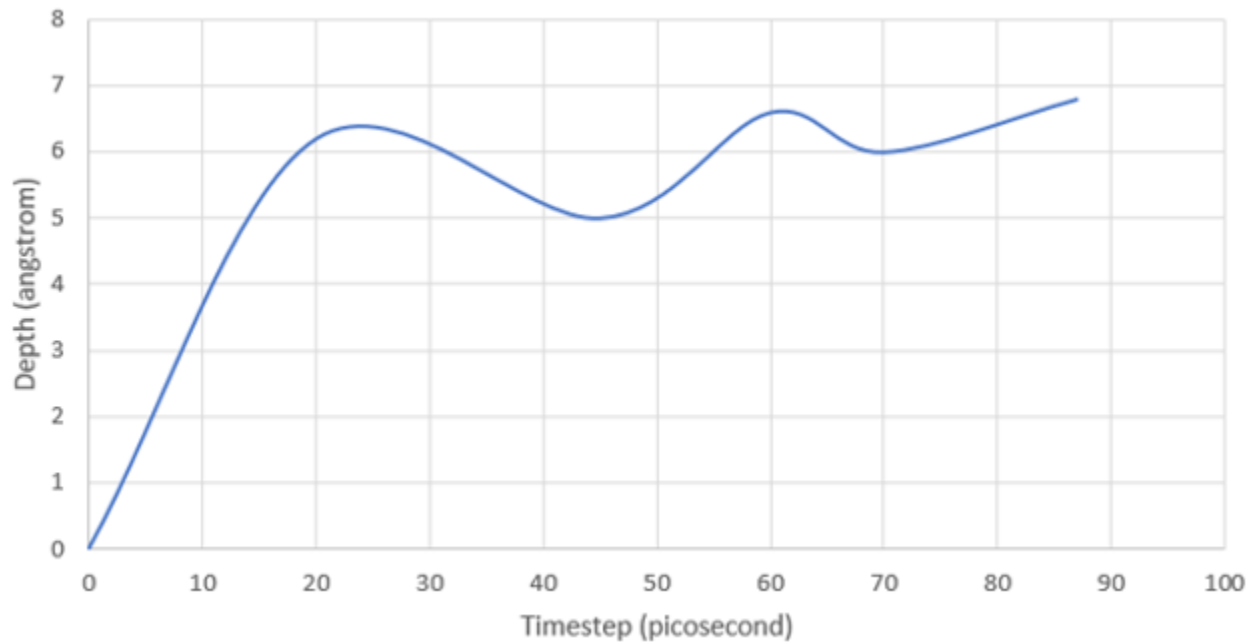
Figure 4.32   Timestep vs depth for H atom that penetrated the deepest into Fe_3C (1800 F)

4.10.1   Summary of Objective C

CH_4 will form very fast if 4 H atoms are within 2.1 Å from a carbon. At these distances, the effect of temperature is minimum. At 800F and 950 H atoms, CH_4 formed at 2 ps at MD

timescale. CH_3 formed during the minimization process then moved around the void and formed CH_4.

4.11 Objective D: Evaluate the rate of formation of methane at different temperatures and void size

Our approach to this objective was similar to Objective C with the differences being using 868 H atoms, 6 carbon, and temperatures on the Nelson curve (512F, 515F, 525F, 530F, 550F, 575F, 650F). Our goal was to form CH_4 at the MD timescale. The same two approaches regarding H atoms' proximity to carbon were used as compared to Objective C. At 0.75-2.1 Å CH_4 formed during the minimization process. At 0.75-23 Å, we did not form CH_4. However, we form CH_2 during the minimization process. CH_2 moved around the void and at 3 ps it formed CH_3 (figure 4.33). We believe that more likely, over time as more H atoms enter the structure, CH_4 will form.
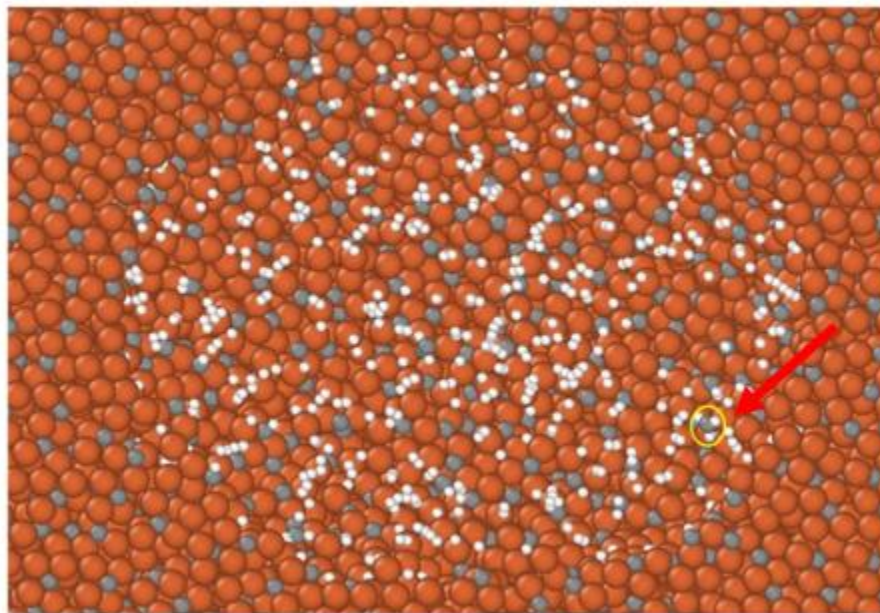
Figure 4.33 CH_3 form at 0.75-23 A. All temperatures

4.11.1   Summary of objective D

At distances between 0.75-2.1 Å CH_4 formed during minimization. The effect of temperature had minimum effects at these distances. CH_2 formed during the minimization then moved around the void and form CH_3. We did not get CH_4 to form at these temperatures. However, we can conclude that if given enough time, CH_4 will form as more H atoms enter the void.

4.12   Future Research Directions

To accurately understand the behavior of HTHA using MD, future research is needed. Below is a list of items that can improve the predictability and behavior of this damage mechanism.

1. An interatomic potential (Fe-C-H) calibrated to fit HTHA properties

2. Use the new interatomic potential to further explore CH_4 formation in the void with NEB.

3. Use the Eyring Equation with experimental data to estimate delta S and get delta H from NEB to better understand the CH_4 formation rate

4. Scale up to macroscale using CH_4 formation rate as a function of void size and other conditions

5. Study the effect of stored deformation in cementite.

4.13   Conclusions

Overall, the MEAM Fe-C-H interatomic potential is very good and even though it was fitted to the H embrittlement parameters, it also was able to capture the behavior of HTHA very nicely. We believe the potential accuracy predicts the pattern of how HTHA forms.

For H to get into the void of a cementite structure from a surface, the higher temperature behaves differently than the lower temperatures. The higher the temperature the faster the diffusion

rate of H atoms into the steel. H atom will penetrate more deeply into the deformed region of cementite. H diffused into cementite rapidly enough to be observed in the MD time scale. The most difficult process and the one that takes the longest to form HTHA is when H tries to take Carbon out of the Fe_3C structure. The CH_4 formation was different when two H_2 were on a surface compared to being inside a void. Regarding the surface, it required ~ twice the amount of energy compared to inside the void. Regarding inside the void, we observed two different scenarios, either the H_2 will attach to a single Carbon then over time will break the bond from Fe_3C, or when H_2 gets at close enough proximity carbon will diffuse from the Fe_3C structure and form CH_2 then overtime will form CH_4. Due to the energy required by either approach (inside the void), the most likely scenario is the former rather than the latter. The effect of the density level of H on CH_4 formation was highly dependent on the amount of H atom to C ratio that is present. We observed that for a void size of 56.42 Å in diameter, we needed 158 H/C to form CH_4 overtime at 800 F. The rate of formation of CH_4 at different temperatures, and void size were highly dependent on the proximity of the H atoms to the C atom. At close proximities, CH_4 will form independent of temperature and during the minimization process. Carbons that are not bonded to the Fe_3C, which can occur during the manufacturing process of the metal, were more likely to move around the void and first form CH_2, then CH_3, and finally CH_4 with H atoms. This process of H atoms being near carbon and the carbon not being bonded to the Fe_3C structure is the reason why HTHA can occur more rapidly in some metals compared to others.

CHAPTER V

CONCLUSION

The use of a MEAM Fe-C-H interatomic potential that was fitted to hydrogen embrittlement parameters resulted in adequate data to model the behavior pattern of HTHA. As long as the oil and gas industry continues to use carbon steel, low alloy steel material, and operate at 400F and above at 50 psia hydrogen partial pressure, the risk of experiencing HTHA is high. The simple matrix of carbon steel material makes it susceptible to HTHA. The manufacturing process which could be within the industry-accepted standard still does not make the carbon steel immune to HTHA. A better manufacturing process that would minimize any free carbon (not bonded adequately) will improve the resistibility of carbon steel. However, there is enough data in the industry to show that going to a higher alloy material can eliminate the risk of HTHA. Our research shows that HTHA can be modeled at an atomistic level in the MD timescale. The effect of temperature is more dominant in H penetration and weakening of the Fe_3C structure by producing the deformation of atoms around the void which allows a higher H diffusion rate into the steel, however, when H atoms are near C the formation of CH_4 can occur rapidly at any temperature. The formation of CH_4 on the surface requires a lot more energy (twice as much) compared to inside a void. This agrees with the Nelson curves and the respective industry literature. The most difficult process and the one that takes the longest to form HTHA is when H tries to take Carbon out of the Fe_3C structure. The most likely scenario to form CH_4 inside a void is that H_2 will attach to a single C atom that is bonded to Fe_3C then over time will form CH_4 with another H_2 that is nearby causing the C to break the bond from Fe_3C. Our findings did show that

to form CH_4 it requires a saturation of H to C ratio; hence this is part of the reason CH_4 formation requires a significant amount of time (years). CH_4 when formed, behaves more stable and hence tends to repel another CH_4 molecule. The molecular dynamic approach to HTHA provides greater insight into the movability and formation of CH_4 inside the structure which cannot be seen under the empirical approach. Catastrophic failures have occurred leading to fatalities in the oil and gas industry, even though the failing components were thought to be operating at safe working limits regarding the Nelson curves. The Nelsons curves need to be revised to capture all the effects of hydrogen in the steel and hence reduced the likelihood of premature equipment failure. A better fundamental understanding of the HTHA process is needed so that better predictive models of HTHA damage can be developed to avoid failures. We believe that if more research is done in MD and bridging the scale to the macro level, we can eventually develop better curves, with higher accuracy of predictability, and could even lead to replacing the Nelson curves.

Our M7x1 high-speed tap failed in a brittle, torsional fashion. This was evident by the 45-degree, smooth fracture surface along with rapid crack propagation, and lack of geometry deformation. Comparing the original tap to a new tap that had the same chemical composition and was bought from the same vendor, allowed us to make an adequate comparison to determine the force that was required to break the tap. The quality of the tap during the manufacturing process and the improper use of the tap led to premature failure. The original tap failed at approximately 27.3% lower torque than it should have been. The hardness testing between the original and new taps was~18% in HRC values which led to a converted tensile strength difference of ~27%.

REFERENCES

[1]   D.J. Benac, Paul McAndrew, Reducing the risk of high temperature hydrogen attack (HTHA) failures, Springer. 12 (2012) 624–627. https://doi.org/10.1007/s11668-012-9605-x.

[2]   API-571, Damage mechanisms affecting fixed equipment in the refining industry, Am. Pet. Inst. (2003) 1–270. http://scholar.google.com/scholar?hl=en&btnG=Search&q=intitle:Damage+Mechanisms+Affecting+Fixed+Equipment+in+the+Refining+Industry#0.

[3]   M. Sabine, V. Der Giessen, Micromechanics of high temperature hydrogen attack, Univ. Groningen. (1999) 1–11.

[4]   P.G. Shewmon, Hydrogen attack of carbon steel, Metall. Trans. A. 7A (1976) 279–280. https://doi.org/10.1007/BF02644468.

[5]   S. Wang, A. Nagao, P. Sofronis, I.M. Robertson, Hydrogen-modified dislocation structures in a cyclically deformed ferritic-pearlitic low carbon steel, Acta Mater. 144 (2018) 164–176. https://doi.org/10.1016/j.actamat.2017.10.034.

[6]   L. S, Hydrogen embrittlement (HE) phenomena and mechanisms, in: Stress Corros. Crack. Theory Pract., Woodhead Publishing Series in Metals and Surface Engineering, 2011: pp. 90–130. https://doi.org/10.1533/9780857093769.1.90.

[7]   Z. Tarzimoghadam, D. Ponge, J. Kloewer, D. Raabe, Hydrogen-assisted failure in nickel base alloy UNS N07718 zahra, NACE - Corros. 2016 Conf. Expo. (2016) 1–10.

[8]   S. Pillot, P. Bourges, C. Chauvy, L. Coudreuse, P. Toussaint, K. Orie, Effect Of Ageing And Hydrogen On Fracture Mechanics And Cvn Properties Of 2,25Cr1Mo Steel Grades – Application To Mpt Issues, NACE - Corros. 2009 Conf. Expo. (2009) 1–19.

[9]   A. Kaufman, B. Feldman, R. Balali, Hydrogen damage and prevention in the oil refinery, NACE - Corros. 2011 Conf. Expo. (2011) 1–15.

[10]   J.C. Staats, G.M. Buchheim, A new practical method for prioritizing equipment in HTHA service for inspection and replacement and the challenges in obtaining process conditions to be used in the HTHA assessment, NACE - Corros. 2016 Conf. Expo. (2016) 1–13.

[11]   C. Krauß, G. Andersohn, M. Oeschsner, Influence of different zinc-containing topcoat systems on the susceptibility against hydrogen re-embrittlement of high strength steel, NACE - Corros. 2014 Conf. Expo. (2014) 1–9.

[12]   P.L. Andresen, T.M. Angeliu, Evaluation of the role of hydrogen in SCC in hot water, NACE Int. Corros. 1997. (1997) 1–12.

[13]   R. Johnsen, O.E. Kongstein, B. Nyhus, Susceptibility of hydrogen induced stress cracking of duplex stainless steel at elevated temperature, NACE - Corros. 2011 Conf. Expo. (2011) 1–15.

[14]   A.S. Melfi, Influence of hydrogen concentration and distribution on fracture in nickel, Mech. Eng. Undergrad. Honor. Theses. 55. (2016) 1–47.

[15]   A.A. Benzerga, J.B. Leblond, Ductile fracture by void growth to coalescence, Elsevier Inc., 2010. https://doi.org/10.1016/S0065-2156(10)44003-X.

[16]   B. Revil-Baudard, O. Cazacu, S. Thuillier, E. Maire, Effect of stress triaxiality on porosity evolution in notched bars: Quantitative agreement between a recent dilatational model and X-ray tomography data, Mech. Res. Commun. 50 (2013) 77–82. https://doi.org/10.1016/j.mechrescom.2013.04.005.

[17]   M.J. Nemcko, H. Qiao, P. Wu, D.S. Wilkinson, Effects of void fraction on void growth and linkage in commercially pure magnesium, Acta Mater. 113 (2016) 68–80. https://doi.org/10.1016/j.actamat.2016.04.008.

[18]   V. Tvergaard, Mechanical models of the effect of grain boundary sliding on creep and creep rupture, Rev. Phys. Appliquée. 23 (1988) 595–604. https://doi.org/10.1051/rphysap:01988002304059500.

[19]   A. Hosokawa, D.S. Wilkinson, J. Kang, E. Maire, Onset of void coalescence in uniaxial tension studied by continuous X-ray tomography, Acta Mater. 61 (2013) 1021–1036. https://doi.org/10.1016/j.actamat.2012.08.002.

[20]   E.V.D.R. Giessen, M.W.D. VAN DER Burg, A. Needleman, V. Tvergaard, Void growth due to creep and grain boundary diffusion at high triaxialities, J Mechn Phys. Solids. 43 (1995) 123–165.

[21]   C. Thomas, Risk analysis for high temperature hydrogen attack, Quest Integr. Gr. Ltd. (n.d.) 1–12. https://doi.org/10.1049/jiee-1.1914.0084.

[22]   U.S.C.S. and H.I. Board, Investigation report - catastrophic rupture of heat exchanger (seven fatalities), U.S. Chem. Saf. Hazard Investig. Board. (2010) 1–160. https://doi.org/10.5271/sjweh.3533.

[23] U.S.C.S. and H.I. Board, CSB Safety Alert : Preventing high temperature hydrogen attack (HTHA) CSB safety guidance to prevent HTHA, U.S. Chem. Saf. Hazard Investig. Board. (2016) 1–2.

[24] MTI, MTI project refining methods for predicting HTHA, Mater. Technol. Inst. Publ. (2016) 1–16.

[25] C.R. Industry, California emphasis program California refining industry Naphtha Hydrotreater Units, State Calif. Dep. Ind. Relations. (2010) 1–15.

[26] M. Umar, F. Qayyum, M.U. Farooq, L.A. Khan, S. Guk, U. Prahl, Investigating the Effect of Cementite Particle Size and Distribution on Local Stress and Strain Evolution in Spheroidized Medium Carbon Steels using Crystal Plasticity-Based Numerical Simulations, Steel Res. Int. 92 (2021) 1–13. https://doi.org/10.1002/srin.202000407.

[27] M.T. Bodden Connor, C.D. Barrett, Introduction of Molecular Dynamics for HTHA and a Review Article of HTHA, J. Fail. Anal. Prev. 22 (2022) 1326–1345. https://doi.org/10.1007/s11668-022-01419-4.

[28] M.B. Djukic, G.M. Bakic, V. Sijacki Zeravcic, A. Sedmak, B. Rajicic, The synergistic action and interplay of hydrogen embrittlement mechanisms in steels and iron: Localized plasticity and decohesion, Eng. Fract. Mech. 216 (2019) 1–33. https://doi.org/10.1016/j.engfracmech.2019.106528.

[29] M.B. Djukic, V. Sijacki Zeravcic, G.M. Bakic, A. Sedmak, B. Rajicic, Hydrogen damage of steels: A case study and hydrogen embrittlement model, Eng. Fail. Anal. 58 (2015) 485–498. https://doi.org/10.1016/j.engfailanal.2015.05.017.

[30] M.B. Djukic, G.M. Bakic, V.S. Zeravcic, B. Rajicic, A. Sedmak, R. Mitrovic, Z. Miskovic, Towards a unified and practical industrial model for prediction of hydrogen embrittlement and damage in steels, Elsevier Ltd. 2 (2016) 604–611. https://doi.org/10.1016/j.prostr.2016.06.078.

[31] R.P. Gangloff, Critical issues in hydrogen assisted cracking of structural alloys, Elsevier Sci. (2006) 1–24. https://doi.org/10.1016/B978-008044635-6.50015-7.

[32] S.M. Schlögl, J. Svoboda, E. Van Der Giessen, Evolution of the methane pressure in a standard 2.25Cr-1Mo steel during hydrogen attack, Acta Mater. 49 (2001) 2227–2238. https://doi.org/10.1016/S1359-6454(01)00132-X.

[33] B.J. Lee, J.W. Jang, A modified embedded-atom method interatomic potential for the Fe-H system, Acta Mater. 55 (2007) 6779–6788. https://doi.org/10.1016/j.actamat.2007.08.041.

[34] B.J. Lee, A modified embedded-atom method interatomic potential for the Fe-C system, Acta Mater. 54 (2006) 701–711. https://doi.org/10.1016/j.actamat.2005.09.034.

[35]   M.B. Djukic, G.M. Bakic, V.S. Zeravcic, A. Sedmak, B. Rajicic, Hydrogen embrittlement of industrial components: Prediction, prevention, and models, Corrosion. 72 (2016) 943–961. https://doi.org/10.5006/1958.

[36]   R.K. Dayal, N. Parvathavarthini, Hydrogen embrittlement in power plant steels, Sadhana - Acad. Proc. Eng. Sci. 28 (2003) 431–451. https://doi.org/10.1007/BF02706442.

[37]   M. Dadfarnia, M.L. Martin, D.E. Moore, S.E. Orwig, P. Sofronis, A model for high temperature hydrogen attack in carbon steels under constrained void growth, Int. J. Fract. 219 (2019) 1–17. https://doi.org/10.1007/s10704-019-00376-8.

[38]   API RP 941 7TH ED (2008), Steels for hydrogen service at elevated temperatures and pressures in petroleum refineries and petrochemical plants, API Publ. (1997) 1–14.

[39]   S. Wang, M.L. Martin, P. Sofronis, S. Ohnuki, N. Hashimoto, I.M. Robertson, Hydrogen-induced intergranular failure of iron, Acta Mater. 69 (2014) 275–282. https://doi.org/10.1016/j.actamat.2014.01.060.

[40]   M.L. Martin, B.P. Somerday, R.O. Ritchie, P. Sofronis, I.M. Robertson, Hydrogen-induced intergranular failure in nickel revisited, Acta Mater. 60 (2012) 2739–2745. https://doi.org/10.1016/j.actamat.2012.01.040.

[41]   S. Wang, M.L. Martin, I.M. Robertson, P. Sofronis, Effect of hydrogen environment on the separation of Fe grain boundaries, Acta Mater. 107 (2016) 279–288. https://doi.org/10.1016/j.actamat.2016.01.067.

[42]   Z.E. des akademischen Grades, Micro scale modeling grain boundary damage under creep conditions, Otto-von-Guericke-UniversityMagdeburg. (2014) 1–113.

[43]   D. Eliezer, High-temperature hydrogen attack of carbon steel, J. Mater. Sci. 16 (1981) 2962–2966. https://doi.org/10.1007/BF00540300.

[44]   S. Pillot, P. Bourges, I. Creusot, G. Masson, L. Coudreuse, I. Loire, P. Toussaint, R. De Chatelet, Effect of hydrogen on mechanical behavior for 2¼ Cr 1Mo steel grades (standard and vanadium added), NACE - Corros. 2008 Conf. Expo. (2008) 1–19.

[45]   P. Pillot, Sylvain; Corre, Stephanie; Coudreuse, Lionel; Chauvy, Cedric; Toussaint, Development and production of creep and hydrogen resistant grade 91 (9 Cr1 Mov) heavy plates for new generating high efficiency refining reactors, NACE - Corros. 2013 Conf. Expo. 91 (2013) 1–15.

[46]   E. van der Giessen, V. Tvergaard, Interaction of cavitating grain boundary facets in creeping polycrystals, Elsevier Sci. B.V. 17 (1994) 47–69. https://doi.org/10.1016/0167-6636(94)90013-2.

[47] T. Laha, R. Balasubramaniam, M.N. Mungole, A. Tewari, R.G. Baligidad, Microstructural evolution in iron aluminide Fe-28Al-2C after high-temperature hydrogen treatment, Metall. Mater. Trans. A. 35A (2004) 1789–1790. https://doi.org/10.1007/s11661-004-0087-7.

[48] M.C. White, Stress-accelerated high temperature hydrogen attack in a catalytic reformer combined feed-effluent exchanger, Mater. Corros. Eng. Pojects Technol. - Proj. Eng. Serv. Shell Glob. Solut. Int. (n.d.) 1–10.

[49] L.C. Chen, P. Shewmon, Stress-assisted hydrogen attack cracking in 2.25Cr-1Mo steels at elevated temperatures, Metall. Mater. Trans. A. 26A (1995) 2317–2318. https://doi.org/10.1007/BF02671246.

[50] E.E. Fletcher, A.R. Elsea, The effects of high pressure, high-temperature hydrogen on steel, DMIC. (1964) 1–70.

[51] S.M. Schlogl, E. Van Der Giessen, Y. Van Leeuwen, On methane generation and decarburization in low-alloy Cr-Mo steels during hydrogen attack, Metall. Mater. Trans. A Phys. Metall. Mater. Sci. 31A (2000) 125–137. https://doi.org/10.1007/s11661-000-0059-5.

[52] S.M. Schlögl, E. Van Der Giessen, Computational model for carbon diffusion and methane formation in a ferritic steel during hydrogen attack, Scr. Mater. 46 (2002) 431–436. https://doi.org/10.1016/S1359-6462(02)00008-8.

[53] M.L. Martin, M. Dadfarnia, S. Orwig, D. Moore, P. Sofronis, A microstructure-based mechanism of cracking in high temperature hydrogen attack, Acta Mater. 140 (2017) 300–304. https://doi.org/10.1016/j.actamat.2017.08.051.

[54] S. Decker, T. Hynes, G. Buchheim, Safe operation of a high temperature hydrogen attack affected DHT reactor, NACE - Corros. 2009 Conf. Expo. (2009) 1–14.

[55] S.N. Karlsdottir, G. Ltd, T. Jonsson, Hydrogen damage of carbon steel fragments from the IDDP-1 geothermal well, NACE - Corros. 2018 Conf. Expo. (2018) 1–11.

[56] M.W.D. Van Der Burg, E. Van Der Giessen, R.C. Brouwer, Investigation of hydrogen attack in 2.25Cr-1Mo steels with a high-triaxiality void growth model, Acta Mater. 44 (1996) 505–518. https://doi.org/10.1016/1359-6454(95)00203-0.

[57] S. Tang, T.F. Guo, L. Cheng, Modeling hydrogen attack effect on creep fracture toughness, Int. J. Solids Struct. 48 (2011) 2909–2919. https://doi.org/10.1016/j.ijsolstr.2011.06.007.

[58] API RP 941 8TH Edition, Steels for hydrogen service at elevated temperatures and pressures in petroleum refineries and petrochemical plants, API Publ. 941. (2016) 1–56.

[59] N.N. Kolgatin, Z.A. Glikman, V.P. Teodorovich, V.I. Deryabina, Failure of steels in hydrogen at high temperature and pressures, All-Unin Res. Inst. Petrochemical Process. (1959) 17–18.

[60] Bakerrisk, Avoiding high temperature hydrogen attack, Bak. Risk. (2015) 1–2.

[61] M. Ransick, P. Shewmon, Effect of cold work on hydrogen attack, Metall. Trans. A. 12A (1981) 17–18. https://doi.org/10.1080/0075417X.2011.614738.

[62] G. Sundararajan, P.G. Shewmon, The kinetics of hydrogen attack of steels, Metall. Mater. Trans. A. 12A (1981) 1761–1762. https://doi.org/10.1179/cmq.1967.6.1.9.

[63] T.A.P. and P.. Shewmon, Effects of tempering on the carbon activity and hydrogen attack kinetics of 2.25Cr-1 Mo steel, Metall. Trans. A. 15A (1984) 2021–2022. https://doi.org/10.1007/bf02670341.

[64] G. Sundararajan, P.G. Shewmon, The hydrogen attack of HSLA steels, Metall. Trans. A. 11 (1980) 509–516. https://doi.org/10.1007/BF02654574.

[65] M.M. Al-aradah, M. Al-Otaibi, M.E. Moh'd, Evaluation of HTHA effect on carbon steel & carbon 0 .5 Mo exchanger using various NDE techniques for reformer waste heat boiler gas exchanger in hydrogen unit, Mina Abdulla Refinery, Kuwait Natl. Pet. Co. (2009) 1–33.

[66] M. Al Arada, M. Al Otaibi, Evaluation of high temperature hydrogen attack effect on carbon steel - 0.5 Mo heat exchanger, NACE - Corros. 2014 Conf. Expo. (2014) 1–11.

[67] I.D. Skrypnyk, Analytic evaluation of hydrogen-assisted void growth at high temperatures, 33 (1997) 478–490.

[68] K.H. Subramanian, J.I. Mickalonis, G.L. Edgemon, Characteristic electrochemical noise during electrochemical determination of hydrogen permeation, NACE - Corros. 2006 Conf. Expo. (2006) 1–10.

[69] N. Trimborn, Detecting and quantifying high temperature hydrogen attack (HTHA), 19th World Conf. Non-Destructive Test. 2016. (2016) 1–4.

[70] B. Chambers, M. Gonzalez, Y. Chen, W. Marc, Sulfide stress cracking of super 13Cr martensitic stainless steel – localized corrosion and hydrogen embrittlement influences, NACE - Corros. 2018 Conf. Expo. (2018) 1–15.

[71] T. Tran, B. Brown, S. Nesic, Corrosion of mild steel in an aqueous CO2 environment – basic electrochemical mechanisms revisited, NACE - Corros. 2015 Conf. Expo. (2015) 1–11.

[72] P. Shewmon, Y.H. Xue, Effect of high-pressure hydrogen on crack growth in carbon steel, Metall. Trans. A. 22A (1991) 2703–2704. https://doi.org/10.1007/BF02851364.

[73] M.W.D. Van Der Burg, E. Van Der Giessen, A Continuum damage relation for hydrogen attack cavitation, Acta Mater. 45 (1997) 3047–3057. https://doi.org/10.1016/S1359-6454(96)00382-5.

[74] H. Saguees, A A, Hall, B O, and Wiedersich, Mechanisms of hydrogen attack, Scr. Met. (United States). 12 (1978) 319–326. https://doi.org/10.1016/0036-9748(78)90121-7.

[75] A. Needleman, J.R. Rice, Plastic Creep Flow Effects in the Diffusive Cavitation of Grain Boundaries., Acta Metall. 28 (1980) 1315–1332. https://doi.org/10.1016/0001-6160(80)90001-2.

[76] H.M. Shih, R.R. Johnson, A model calculation of the Nelson curves for hydrogen attack, Acta Metall. 30 (1982) 537–545. https://doi.org/10.1016/0001-6160(82)90234-6.

[77] P. Shewmon, Synergism between creep ductility and grain boundary bubbles, Acta Mater. 35 (1987) 1317–1324.

[78] A.A. Astaf'ev, Dissolution and redistribution of hydrogen in steel, 1996 Plenum Publ. Corp. 37 (1995) 192–193.

[79] M. Castillo, C.E. Rogers, J.H. Payer, M. Quintana, Hydrogen permeation and hydrogen concentration measurements to model diffusible hydrogen in weld metal, Corros. 2000. (2000) 1–14.

[80] T. Boellinghaus, E. Viyanit, H. Hoffmeister, Numerical modelling of hydrogen assisted cracking th., NACE Int. (2001) 1–17.

[81] D. Ilin, Simulation of hydrogen diffusion in fcc polycrystals . Effect of deformation and grain boundaries, PhD Thesis, Univ. Bordeaux. (2014) 1–203.

[82] S.N. Karlsdottir, I.O. Thorbjornsson, R. University, Hydrogen embrittlement and corrosion in high temperature geothermal well, NACE - Corros. 2012 Conf. Expo. (2012) 1–18.

[83] A. Turnbull, A review of the possible effects of hydrogen on lifetime of carbon steel nuclear waste canisters, Nagra. (2009) 1–68.

[84] T.G. Martin, K. Wilken, Hydrogen induced cracking failure of SA 516 grade 70 steel in near neutral to high PH solution: part 1 field investigation, NACE - Corros. 2003 Conf. Expo. (2003) 1–19.

[85] R.J. Conder, P. Felton, R. Burke, P. Dent, Hydrogen embrittlement testing of high strength low carbon martensitic steels, NACE - Corros. 2010 Conf. Expo. (2010) 1–14.

[86] M. Sagara, Y. Tomio, Y. Otome, N. Sawawatari, T. Omura, H. Amaya, Evaluation of susceptibility to hydrogen embrittlement of high strength corrosion resistant alloys, NACE - Corros. 2016 Conf. Expo. (2016) 1–15.

[87] W. Huang, W. Sun, A. Samson, D. Muise, Investigation of hydrogen embrittlement susceptibility of precipitation hardened nickel alloys under cathodic protection condition, NACE - Corros. 2013 Conf. Expo. (2014) 1–15.

[88] G. Schmitt, T. Gommlich, K. Schoettler, Atomic hydrogen from electroplating of high strength steels – How much is trapped in the coating? Guenter, NACE - Corros. 2016 Conf. Expo. (2016) 1–10.

[89] B. Worthingham, L. Yang, F. King, J. Xie, Hydrogen effects on high strength pipeline steels, NACE - Corros. 2009 Conf. Expo. (2009) 1–15.

[90] K. Takai, Y. Homma, J. Seki, Hydrogen trapping sites in high-strength steels at delayed fracture, NACE - Corros. 1996 Conf. Expo. (1996) 1–13.

[91] S. Ronneteg, A. Juhlin, U. Kivisakk, Hydrogen embrittlement of duplex stainless steels testing of different product forms at low temperature, NACE - Corros. 2007 Conf. Expo. (2007) 1–9.

[92] Y.I. Archakov, I.. Grebeshkova, V.. Dubovskii, Hydrogen resistance of steels 20, 12 MKh, and 30KhMA at elevated temperature, Plenum Publ. Co. (1969) 18–19.

[93] M.R. Louthan, Effect of hydrogen on metals, E. I. Du Pont Nemours Co Savannah River Lab. Aiken, S.C. (1974) 1–25.

[94] Y. Zhao, M.Y. Seok, I.C. Choi, Y.H. Lee, S.J. Park, U. Ramamurty, J.Y. Suh, J. Il Jang, The role of hydrogen in hardening/softening steel: Influence of the charging process, Scr. Mater. 107 (2015) 46–49. https://doi.org/10.1016/j.scriptamat.2015.05.017.

[95] P.. Timmins, Solutions to Hydrogen Attack in Steels, Am. Soc. Met. Intl. (1997).

[96] T.A. Parthasarathy, H.F. Lopez, P.G. Shewmon, Hydrogen Attack kinetics of 2.25 Cr-1 Mo steel weld metals, Metall. Trans. A. 16A (1985) 1143–1144. https://doi.org/10.1007/BF02811683.

[97] D. Moorhead, H. Nelson, Fractography of the high temperature hydrogen attack of a medium carbon steel (NASA), Natl. Aeronaut. Sp. Adm. (1975) 1–17.

[98] P. Elliot, Materials performance in high-temperature environments - making the choice, NACE - Corros. 2000 Conf. Expo. (2000) 1–22.

[99] J.L. Carpenter, W.F. Stuhrke, Hydrogen embrittlment of structural alloys - A technology survey, Natl. Aeronaut. Sp. Adm. 168 (1976) 1–123.

[100] P. Aaltonen, T. Saario, P. Karjalainen-Roikonen, J. Piippo, S. Tahtinen, Vacancy-creep model for EAC of metallic materials in high temperature water, NACE - Corros. 1996 Conf. Expo. (1996) 1–12.

[101] H.R. Copson, The influence of corrosion on the cracking of pressure vessels, Int. Nickel Company, Inc. A-151 (1953) 1–19.

[102] F. El Shawesh, Effect of strain rate and temperature on the susceptibility of 304 austenitic stainless steel to hydrogen embrittlement, NACE - Corros. 1998 Conf. Expo. (1998) 1–12.

[103] F. Silva, J. Santos, R. Gouveia, Dissolution of grain boundary carbides by the effect of solution annealing heat treatment and aging treatment on heat-resistant cast steel HK30, Metals (Basel). 7 (2017) 1–12. https://doi.org/10.3390/met7070251.

[104] A. Roy, High Temperature Hydrgoen Attack (HTHA), Swiss, Re. (2015) 1–32.

[105] RDK Audit, Refineria di Korsou technical audit report, RDK Audit. (2017) 1–82.

[106] E.I.C.E. Eady, Welding and cuttting, Aerlikon Metco. 16 (2017) 275–336.

[107] P.G. Shewmon, Hydrogen Attack of Pressure Vessel Steel, Ohio State Univ. Dep. Metall. Eng. (1980) 1–8.

[108] X. Roumeau, High-temperature cracking of 800 HT pigtails in a hydrogen unit, NACE - Corros. 2010 Conf. Expo. (2010) 1–11.

[109] J. Rothwell, Maintaining the integrity of process plant susceptible to high temperature hydrogen attack . Part 2 : factors affecting carbon steels RR1134, TWl Ltd. (2018) 1–58.

[110] B. Saba, Evaluation of mechanical fitness for service of high temperature hydrogen attacked steels, Louisiana State Univ. Agric. Mech. Coll. (2003) 1–174.

[111] T. Silfies, J.D. Dobis, M. Nugent, Looking behind the curtain of API RP 941 high temperature hydrogen attack (HTHA) data, NACE - Corros. 2016 Conf. Expo. (2016) 1–12.

[112] G.M. McKimpson, Initial hydrogen attack kinetics in a carbon steel, Ohio State Univ. Univ. Microfilm. Int. (1977) 1–162.

[113] J.. Brear, J.. Church, Technical basis for API Publication RP941 (Nelson Curves), Res. Gate. (1996) 1–12.

[114] H. Damage, G.H. Joint, I. Project, P. You, C.A.N. Trust, Preventing HTHA failures with the buckeye model, Equity Eng. (2013) 1–2.

[115] M. Nugent, T. Silfies, J.D. Dobis, A review of high temperature hydrogen attack (HTHA) modeling, prediction, and non-intrusive inspection in refinery applications, NACE - Corros. 2017 Conf. Expo. (2017) 1–13.

[116] A. G142-98, Standard test method for determination of susceptibility of metals to embrittlement in hydrogen containing environments at high pressure , high temperature, or both, ASTM Int. (2016) 1–8. https://doi.org/10.1520/G0142-98R16.2.

[117] API 579-1, Fitness-for-service, API Publ. (2016) 1–1320.

[118] API 580, API RP 580: Risk-based inspection, API. (2009) 1–96.

[119] API-581, API RP 581: Risk-based inspection technology, API Recomm. Pract. 581. (2008) 1–654. http://www.irantpm.ir/wp-content/uploads/2011/08/API-581-2008.pdf.

[120] C. Allevato, Utilizing acoustic emission testing to detect high-temperature hydrogen attack (HTHA) in Cr-Mo reformer reactors and piping during thermal gradients, Elsevier Ltd. 10 (2011) 3552–3560. https://doi.org/10.1016/j.proeng.2011.04.585.

[121] C. Nageswaran, Maintaining the integrity of process plant susceptible to high temperature hydrogen attack. Part 1: analysis of non-destructive testing techniques, Crown. (2018) 1–58.

[122] A. Yamani, A cost effective development of an ultrasonic A-scans database for high-temperature hydrogen attack, Elsevier Ltd. 41 (2008) 163–168. https://doi.org/10.1016/j.ndteint.2007.10.007.

[123] B.A. Kolachev, Hydrogen in Metals and Alloys, Met. Sci. Heat Treat. 41 (1999) 93–100.

[124] B.A. Kolachev, Hydrogen embrittlement of metals, Itogi Nauk. Tekh.. Met. Term. Obrab. 23 (1989) 3–46.

[125] Chitu Georghe, Metallurgia, 8 (1964) 34–39.

[126] C. Borchers, T. Michler, A. Pundt, Effect of hydrogen on the mechanical properties of stainless steels, Adv. Eng. Mater. 10 (2008) 11–23. https://doi.org/10.1002/adem.200700252.

[127] M. Nugent, T. Silfies, P. Kowalski, N. Sutton, Recent applications of evaluations of equipment in HTHA service, NACE - Corros. 2018 Conf. Expo. (2018) 1–23.

[128] ASTM Internation, ASTM A600- standard specification for tool steel high speed, (2014) 1–5. https://doi.org/10.1520/A0600-92AR16.2.

[129] G.A. T.E. Aaron, ASM Handbook, ASM Int. 16 (1995) 1089.

[130] A.M. Bayer, B.A. Becherer, T. Vasco, High speed tool steels, ASM Int. 16 (1989) 10–11.

[131] E. Saikoff, E. Andersson, M. Galstyan, C. Olausen, F. Bengtsson, D. Vikström, J.B. Lazraq, Cobalt in high speed steels, UPPSALA Univ. (2018) 42.

[132] W.J. Salesky, Medium carbon steel alloy design for wear application, Wear. 75 (1982) 21–40.

[133] T.G. Digges, S.J. Rosenberg, G.W. Geil, Heat treatment and properties of iron and steel, Washington, DC US Dept. Commer. (1966) 1–46.

[134] J.A. T, N. Corporation, Electric arc furnace steelmaking, Am. Iron Steel Institue. (2008) 1–9.

[135] D.D.D.P. Tjahjana, Y. Waloyo, Triyono, Failure analysis of super hard end mill HSS-Co, Open Eng. 9 (2019) 202–210. https://doi.org/10.1515/eng-2019-0025.

[136] A. Analytica, Gloabl machine tools market, Astuta Anal. (2021) 1–130.

[137] McMaster-Carr, General purpose taps, Https://Www.Mcmaster.Com/Tapping-Bits/General-Purpose-Taps-9/. (n.d.).

[138] M.B. Connor, M. Calhoun, M. Cohen, D. Lum, M. KaJuana, S. Toellner, D. Dickel, Failure Analysis of a M7X1 High-Speed Steel Tap, J. Fail. Anal. Prev. 22 (2022) 1431–1441. https://doi.org/10.1007/s11668-022-01423-8.

[139] H. Jang, Effects of Overused Top-hammer Drilling Bits, Insights Min. Sci. Technol. 01 (2019) 37–43. https://doi.org/10.19080/imst.2019.01.555558.

[140] V. Gnanasekaran, J. Ekanthamoorthy, K. Senthilkumar, Failure analysis of solid carbide cutting tool used in milling operation, Int. J. Chem. Sci. 14 (2016) 1197–1210.

[141] J.S. Wolf, G.D. Neale, Design of a high speed friction and wear machine with test results for steels, Wear. 75 (1982) 145–157. https://doi.org/10.1016/0043-1648(82)90144-2.

[142] I. Jung, V. Lubich, H.-J. Wieland, Tool failures - Causes and prevention, Proc. 6th Int. Tool. Conf. (2002) 1343–1362. https://www5.kau.se/sites/default/files/Dokument/subpage/2010/02/93_1343_1362_pdf_76008.pdf.

[143] X. Yang, C.R. Liu, A new stress-based model of friction behavior in machining and its significant impact on residual stresses computed by finite element method, Int. J. Mech. Sci. 44 (2002) 703–723. https://doi.org/10.1016/S0020-7403(02)00008-5.

[144] D.Y. Pimenov, A. Hassui, S. Wojciechowski, M. Mia, A. Magri, D.I. Suyama, A. Bustillo, G. Krolczyk, M.K. Gupta, Effect of the relative position of the face milling tool towards the workpiece on machined surface roughness and milling dynamics, Appl. Sci. 9 (2019) 1–17. https://doi.org/10.3390/app9050842.

[145] S. Sbderberg, M. Nissle, Performance and failure of high speed steel drills related to wear, Wear. 75 (1982) 123–143.

[146] M. Zetek, I. Česáková, V. Švarc, Increasing cutting tool life when machining inconel 718, Procedia Eng. 69 (2014) 1115–1124. https://doi.org/10.1016/j.proeng.2014.03.099.

[147] Makeitfrom, SAE-AISI M2 (T11302) Molybdenum high-speed steel, Https://Www.Makeitfrom.Com/Material-Properties/SAE-AISI-M2-T11302-Molybdenum-High-Speed-Steel. (n.d.).

[148] M.M. Yovanovich, Micro and macro hardness measurements, correlations, and contact models, Am. Institue Aeronaut. Astronaut. (2006) 1–28. https://doi.org/10.2514/6.2006-979.

[149] M.P. Groover, Introduction to manufacturing processes, 2012.

[150] B.D. Darwent, Bond dissociation energies in simple molecules. National Standard Reference Data Series, National Bureau of Standards, 31, J. Chem. Educ., Washingt. DC. (1970) 52.

[151] K.L. Sungkwan Mun; Doyl Dickel, Sara Adibi, Bradley Huddleston, Raj Prabhu, A Modified Embedded Atom Method (MEAM) Interatomic Potential for the Fe-C-H System Authors: Sungkwang Mun, (2021) 1–26. https://doi.org/https://doi.org/10.48550/arXiv.2109.01712.

[152] H. Feilchenfeld, Bond length and bond energy in hydrocarbons, J. Phys. Chem. 61 (1957) 689–700. http://www.jstor.org/stable/3276141.

[153] H.K.D.H. Bhadeshia, Cementite, Int. Mater. Rev. 65 (2020) 1–27. https://www.tandfonline.com/action/journalInformation?journalCode=yimr20.

[154] K.O.E. Henriksson, K. Nordlund, Simulations of cementite: An analytical potential for the Fe-C system, Phys. Rev. B - Condens. Matter Mater. Phys. 79 (2009) 1–6. https://doi.org/10.1103/PhysRevB.79.144107.

[155] G. Henkelman, B.P. Uberuaga, H. Jónsson, Climbing image nudged elastic band method for finding saddle points and minimum energy paths, J. Chem. Phys. 113 (2000) 9901–9904. https://doi.org/10.1063/1.1329672.

[156] T.Z.J.L.S. Yip, Atomistic reaction pathway sampling: The nudge elastic band method and nanomechanics applications, John Wiley Son. 1 (2013) 313–338.

[157] G. Henkelman, H. Jónsson, Improved tangent estimate in the nudged elastic band method for finding minimum energy paths and saddle points, J. Chem. Phys. 113 (2000) 9978–9985. https://doi.org/10.1063/1.1323224.

[158] A. Nakano, A space-time-ensemble parallel nudged elastic band algorithm for molecular kinetics simulation, Comput. Phys. Commun. 178 (2008) 280–289. https://doi.org/10.1016/j.cpc.2007.09.011.

[159] E. Maras, O. Trushin, A. Stukowski, T. Ala-Nissila, H. Jónsson, Global transition path search for dislocation formation in Ge on Si(001), Comput. Phys. Commun. 205 (2016) 13–21. https://doi.org/10.1016/j.cpc.2016.04.001.

[160] S.N.L.T. University, LAMMPS documentation, Https://Docs.Lammps.Org/Neb.Html. (2007).

[161] J.M. Goodman, P.D. Kirby, L.O. Haustedt, Some calculations for organic chemists: Boiling point variation, Boltzmann factors and the Eyring equation, Tetrahedron Lett. 41 (2000) 9879–9882. https://doi.org/10.1016/S0040-4039(00)01754-8.

APPENDIX A

LAMMPS INPUT SCRIPT

A.1 Input script for MD: Objective A, C, D

```
# ------------------------- INITIALIZATION --------------------------

units           metal

dimension       3

boundary        p       p       p

atom_style      atomic

neighbor 2.0 bin

neigh_modify delay 0 every 1 check yes page 500000 one 50000

# ----------------------- ATOM DEFINITION ---------------------------

read_data   coordinate_data.lmp

# ------------------------ FORCE FIELDS -----------------------------

pair_style      meam/c

pair_coeff      * * meamf_FeCH_new_lmp.txt Fe C H meafile_FeCH_new_lmp.txt Fe C H

# ------------------------- SETTINGS --------------------------------

compute csym all centro/atom bcc

compute peratom all pe/atom

thermo          1

######################################

# MINIMIZATION

minimize 1e-10 1e-10 600 10000

fix 1 all box/relax aniso 0.0 vmax 0.001

minimize 1000 1e-10 600 10000

unfix 1
```

```
###########################################
# EQUILIBRATION

shell mkdir dumps

change_box all x scale 1.06 y scale 1.09 z scale 1.04 remap

restart 10000 poly.restart

reset_timestep 0

reset_ids

velocity all create 549.82 12345 mom yes rot no

fix 1 all npt temp 549.82 549.82 1 aniso 27.58 27.58 1

#thermo_style custom step temp ke pe press

thermo_style custom step temp etotal pe pxx pyy pzz pxy pxz pyz lx ly lz

# Use cfg for AtomEye

dump   1 all cfg 1000 dumps/dump.D1000.H25.6C.530F.H.Void.htha1_*.cfg mass type xs ys zs

c_csym c_peratom fx fy fz

dump_modify 1 element Fe C H

timestep 0.0001

run              350000

###########################################
# SIMULATION DONE

print "All done"
```

A.2   Input script for the NEB conversion study: replica, K-spring, timestep

```
# ----------------------- INITIALIZATION ---------------------------

units           metal
```

dimension   3

boundary   p   p   p

atom_style   atomic

neighbor 2.0 bin

neigh_modify delay 0 every 1 check yes page 500000 one 50000

atom_modify map array sort 0 0.0

variable u uloop 20

---------------------- ATOM DEFINITION --------------------------

read_data   coordinate_data.lmp

---------------------- FORCE FIELDS ----------------------------

pair_style   meam/c

pair_coeff   * * meamf_FeCH_new_lmp.txt Fe C H meafile_FeCH_new_lmp.txt Fe C H

pair_modify shift yes

compute peratom all pe/atom

MINIMIZATION

minimize 1.0e-10 1.0e-10 1000 10000

reset_timestep 0

shell mkdir dumps

timestep 0.0005

fix 1 all neb 0.1 parallel ideal

thermo   100

######################################

dump   1 all cfg 1000 dump.C1000.Void.htha1_*.$u.cfg mass type xs ys zs c_peratom fx fy fz id

dump_modify 1 element Fe C H

min_style quickmin

neb 0.0 0.000001 100000 0 50 final Void.neb.lmp

#######################################

SIMULATION DONE

print "All done"

A.3   Input script for NEB: Objective A, B

----------------------- INITIALIZATION ---------------------------

units   metal

dimension   3

boundary   p   p   p

atom_style   atomic

neighbor 2.0 bin

neigh_modify delay 0 every 1 check yes page 500000 one 50000

atom_modify map array sort 0 0.0

variable u uloop 20

----------------------- ATOM DEFINITION --------------------------

read_data   coordinate_data.lmp

----------------------- FORCE FIELDS ----------------------------

pair_style   meam/c

pair_coeff   * * meamf_FeCH_new_lmp.txt Fe C H meafile_FeCH_new_lmp.txt Fe C H

pair_modify shift yes

compute peratom all pe/atom

MINIMIZATION

minimize 1e-10 1e-10 10000 10000

reset_timestep 0

region   1 block INF INF INF INF INF 1

group   lower region 1

group   mobile subtract all lower

timestep 0.0005

region   surround block 0 8 0 8 0 10 units box

group   nebatoms region surround

group   nonneb subtract all nebatoms

fix 1 lower setforce 0.0 0.0 0.0

fix 2 all neb 0.1 parallel ideal

thermo   100

Dump files

dump   1 all cfg 1000 dump.C1000.Void.htha1_*.$u.cfg mass type xs ys zs c_peratom fx fy fz id

dump_modify 1 element Fe C H

min_style quickmin

neb 0.0 0.000001 100000 0 50 final Void.neb.lmp

#######################################

SIMULATION DONE

print "All done"

APPENDIX B

PYTHON CODE

B.1 Python: Objective A

```
import numpy as np

for i in range (1):

    N = np.array([287.414,257.932,215.625])

    n = np.random.rand(172,3)

    n[:,0]*=N[0]

    n[:,1]*=N[1]

    n[:,2]=n[:,2]*30+(N[2]-30)

    print 'H'  ,i+1  ,n,'\n\n'
```

B.2 Python: Objective B

```
import numpy as np

for i in range (1):

    N = np.array([63.24,63.24,63.24])

    n = np.random.rand(41,3)

    n[:,0]=n[:,0]*N[0]+112.7072

    n[:,1]=n[:,1]*N[1]+97.96576

    n[:,2]=n[:,2]*N[2]+121.658

    print (n,'\n\n')
```

B.3 Python: Objective C, D

```
import numpy as np
```

```python
for i in range (6):

    N = np.array([63.25,63.25,63.25])

    n = np.random.rand(275,3)

    n[:,0]=n[:,0]*N[0]+112.08

    n[:,1]=n[:,1]*N[1]+97.34

    n[:,2]=n[:,2]*N[2]+76.21

    print (n,'\n\n')
```